

# Carbon Nanotubes and Graphene in Aqueous Surfactant Solutions: Molecular Simulations and Theoretical Modeling

by

Shangchao Lin

B. S., Mechanical Engineering, University of Michigan, 2006

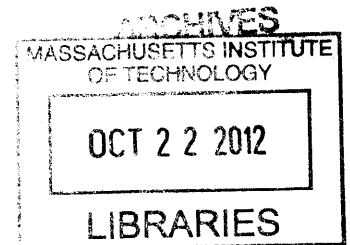
S. M., Mechanical Engineering, Massachusetts Institute of Technology, 2008

Submitted to the Department of Mechanical Engineering  
in Partial Fulfillment of the Requirements for the Degree of  
Doctor of Philosophy in Mechanical Engineering  
at the

MASSACHUSETTS INSTITUTE OF TECHNOLOGY

September 2012

© 2012 Massachusetts Institute of Technology. All rights reserved.



Author \_\_\_\_\_

Department of Mechanical Engineering  
June 28, 2012

Certified by \_\_\_\_\_

Daniel Blankschtein  
Professor of Chemical Engineering  
Thesis Supervisor

Certified by \_\_\_\_\_

Nicolas G. Hadjiconstantinou  
Professor of Mechanical Engineering  
Chairman, Doctoral Thesis Committee

Accepted by \_\_\_\_\_

David E. Hardt  
Professor of Mechanical Engineering  
Chairman, Committee for Graduate Studies

# **Carbon Nanotubes and Graphene in Aqueous Surfactant Solutions: Molecular Simulations and Theoretical Modeling**

by  
Shangchao Lin

Submitted to the Department of Mechanical Engineering on June 28, 2012  
in Partial Fulfillment of the Requirements for the Degree of  
Doctor of Philosophy in Mechanical Engineering

## **Abstract**

This thesis describes combined molecular simulations and theoretical modeling studies, supported by experimental observations, on properties and applications of carbon nanotubes (CNTs) and graphene sheets dispersed in aqueous surfactant solutions. In particular, the role of the bile salt anionic surfactant, sodium cholate (SC), in dispersing single-walled carbon nanotubes (SWCNTs) and graphene sheets in aqueous solutions was investigated. In addition, the roles of various surfactants (SC, sodium dodecyl sulfate (SDS, anionic), and cetyl trimethylammonium bromide (CTAB, cationic)) in controlling the extent of functionalization of SWCNTs were investigated.

First, the surface structure of adsorbed surfactant (SC) molecules on the SWCNT surface was studied using molecular dynamics (MD) simulations, and the interactions between two SWCNT-SC complexes were determined using potential of mean force (PMF) calculations. I found that the cholate ions wrap around the SWCNT like a ring, and exhibit a small tendency to orient perpendicular to the cylindrical axis of the SWCNT, a unique feature that has not been observed for conventional linear surfactants such as SDS. By comparing my simulated PMF profile of SC with the PMF profile of SDS reported in the literature, I found that, at the saturated surface coverages, SC is a better stabilizer than SDS, a finding that is consistent with the widespread use of SC to disperse SWNTs in aqueous media.

Second, I probed the surface structure and electrostatic potential of monolayer graphene dispersed in a SC aqueous solution. Subsequently, I quantified the interactions between two

graphene-SC complexes using PMF calculations, which confirmed the existence of a metastable bilayer graphene structure due to the steric hindrance of the confined SC molecules. Interestingly, one faces a dilemma when using surfactants to disperse and stabilize graphene in aqueous solution: on the one hand, surfactants can stabilize graphene aqueous dispersions, but on the other hand, they prevent the formation of new AB-stacked bilayer and trilayer graphene resulting from the reaggregation process. Finally, the lifetime and time-dependent distribution of various graphene layer types were predicted using a kinetic model of colloid aggregation, and each graphene layer type was further decomposed into subtypes, including the AB-stacked species and various turbostratic species.

Third, I showed that the free energy of diazonium adsorption onto the SWCNT-surfactant complex, determined using PMF calculations, can be used to rank surfactants (SC, SDS, and CTAB) in terms of the extent of functionalization attained following their adsorption on the nanotube surface. The difference in binding affinities between linear and rigid surfactants was attributed to the synergistic binding of the diazonium ion to the local “hot/cold spots” formed by the charged surfactant heads. A combined simulation–modeling framework was developed to provide guidance for controlling the various sensitive experimental conditions needed to achieve the desired extent of SWCNT functionalization.

In conclusion, molecular simulations of the type discussed in this thesis, which can be used to complement traditional continuum-based theories, provide a powerful tool to investigate nano-structured aqueous dispersions. The combined simulation–modeling methodology presented in this thesis can be extremely useful in predicting material properties and optimizing experimental procedures in order to minimize tedious and time-consuming trial-and-error experimentation when studying other nanoscale systems of interest.

Thesis Supervisor:

Professor Daniel Blankschtein, Department of Chemical Engineering

Thesis Committee Members:

Professor Nicolas G. Hadjiconstantinou (Chairman), Department of Mechanical Engineering

Professor Gregory C. Rutledge, Department of Chemical Engineering

Professor Michael S. Strano, Department of Chemical Engineering

Professor Kripa K. Varanasi, Department of Mechanical Engineering

## Acknowledgements

There are many individuals that I would like to thank for contributing to the completion of this thesis. First, I would like to express my sincere appreciation to my advisor, Professor Daniel Blankschtein, for his dedicated help and guidance in both my work and personal life throughout my years at MIT. He taught me to be critical, delicate, independent, hard-working, creative, and open-minded. I thank him for giving me freedom and support to explore the carbon nanotube and graphene areas, including establishing fruitful collaborations with experimentalists to study nanomaterial/surfactant systems. Without him, this thesis would not have been possible. I also would like to thank him for his support of my family when I had to work remotely in Princeton to take care of my pregnant wife, my new-born daughter, and to write my doctoral thesis.

Second, I would like to thank my doctoral thesis committee members, Professor Nicholas Hadjiconstantinou, Professor Gregory Rutledge, Professor Michael Strano, and Professor Kripa Varanasi, for the time that they have invested, the support that they have provided, and the guidance that they have given, throughout my thesis work at MIT. Special thanks to Professor Strano for his encouragement to establish an intellectually stimulating theoretical-experimental collaboration that has led to various publications summarized in this thesis.

Third, I would like to thank all my colleagues and collaborators at MIT, including those in the Blankschtein group: Chih-Jen Shih, Jonathan Mendenhall, Baris Polat, Professor Pak Yuet, and Professor Lingling Zhao, as well as those in the Strano group: Andrew Hilmer and Jingqing Zhang. Without their wisdom and support, this thesis will not be possible either. I learned a lot from them, and wish them great success in their professional careers. I wish the rest of the current Blankschtein group members, including Jaisree Iyer, Vishnu Sresht, Diviya Sinha, and Carl Schoellhammer, success in their present and future research endeavors.

Most importantly, I would like to express my greatest gratitude to my parents, Xidan Lin and Zhongming Liu, who have supported me throughout my stay in the United States and away from home with their unfailing love and confidence in my efforts. My parents, in particular, have



always shown interest in my daily life, and have been supportive throughout my upbringing in our hometown of Suzhou, a beautiful Chinese city where I lived for 20 years, my undergraduate education at Shanghai Jiao Tong University in Shanghai and at the University of Michigan, my current doctoral education at MIT. I also would like to thank my great in-laws, Shouping Wang and Binlong Jiang, for their strong supports for me and my wife's career choices and hearty cares for their granddaughter.

Words cannot describe my deepest appreciation for my wife Ying Jiang, whose love, understanding, encouragement, and persistent confidence in me has lifted burdens from my shoulders and supported me throughout, even as we are separated by the six-hour commuting between Princeton and Cambridge. I wish that we could have been together during the past seven years. It is her unselfishness, her intelligence, her beauty, and her passion for our future that stirs and inspires me. Finally, to my lovely, beautiful, and chubby three-months old "cutie pie" Amy: you have been and will always be my joy in life. Fatherhood while pursuing a career in academia is not easy, but your smiling face will always encourage me and make me proud. This thesis is dedicated to you.

## Table of Contents

<b>Abstract.....</b>	<b>2</b>
<b>Acknowledgements .....</b>	<b>4</b>
<b>Table of Contents .....</b>	<b>6</b>
<b>List of Figures.....</b>	<b>9</b>
<b>List of Tables.....</b>	<b>17</b>
<b>1. Introductions .....</b>	<b>18</b>
1.1 Overview of Carbon Nanotubes (CNTs) and Graphene .....	18
1.2 The Role of Surfactants in CNT and Graphene Solutions .....	21
1.3 Overview of Molecular Dynamics (MD) Simulations .....	25
1.4 Thesis Overview .....	28
<b>2. Role of the Bile Salt Surfactant Sodium Cholate (SC) in Enhancing the Aqueous Dispersion Stability of Single-Walled Carbon Nanotubes: A Molecular Dynamics Simulation Study.....</b>	<b>30</b>
2.1 Introduction .....	30
2.2 Methods .....	34
2.2.1 Simulation Methods .....	34
2.2.2 Simulated Systems .....	35
2.3 Results and Discussion .....	38
2.3.1 Sodium Cholate Adsorption and Surface Self Assembly on a SWCNT .....	38
2.3.2 Interactions between Two Parallel SWCNTs with Adsorbed Cholate Ions .....	45

2.4	Conclusions .....	53
2.5	Appendix: Supporting Tables and Figures .....	54
<b>3.</b>	<b>Molecular Insights into the Surface Morphology, Layering Structure, and Aggregation Kinetics of Surfactant-Stabilized Graphene Dispersions .....</b>	<b>57</b>
3.1	Introduction .....	57
3.2	Methods .....	61
3.2.1	Simulation Methods .....	61
3.2.2	Experimental Methods .....	64
3.3	Results and Discussion .....	64
3.3.1	Surface Morphology of the Monolayer Graphene-SC Assembly .....	64
3.3.2	Electrostatic Potential around the Monolayer Graphene-SC Assembly .....	69
3.3.3	Interactions between Two Graphene-SC Assemblies .....	72
3.3.4	Metastable Bilayer Graphene and the Turbostratic Layering Structure .....	76
3.3.5	Experimental and Predicted Total Graphene Dispersion Stability .....	79
3.3.6	AB-Stacked and Turbostratic Graphene Dispersion Stability .....	83
3.4	Conclusions .....	86
3.5	Appendix A: Supporting Tables and Figures .....	88
3.6	Appendix B: Summary of Experimental Procedures .....	90
3.7	Appendix C: Kinetic Theory of Graphene Aggregation .....	91
<b>4.</b>	<b>Molecular Perspective on Diazonium Adsorption for Controllable Functionalization of Single-Walled Carbon Nanotubes in Aqueous Surfactant Solutions .....</b>	<b>95</b>
4.1	Introduction .....	95

4.2	Methods .....	97
4.2.1	Simulation Methods .....	97
4.2.2	Experimental Methods .....	100
4.3	Results and Discussions .....	100
4.3.1	Free-Energy Calculations of Diazonium Ion Adsorption .....	100
4.3.2	Understanding the Synergetic Binding Affinity .....	106
4.3.3	Model for the Extent of SWCNT Functionalization .....	111
4.3.4	Modeling Results and Discussions .....	115
4.4	Conclusions .....	118
4.5	Appendix A: Supporting Tables and Figures .....	120
4.6	Appendix B: Deconvolution of SWCNT Fluorescence Spectra .....	122
<b>5.</b>	<b>Thesis Summary, Major Conclusions, and Future Work.....</b>	<b>124</b>
5.1	Thesis Summary and Major Conclusions.....	124
5.2	Future Work .....	127
	<b>Bibliography .....</b>	<b>130</b>

## List of Figures

**Figure 1-1:** Chemical structure and electronic property of CNTs. (a) A single-walled carbon nanotube (SWCNT). Carbon atoms and the covalent bonds between them are shown in red and yellow, respectively.[11] (b) A multi-walled carbon nanotube (MWCNT).[11] Each SWCNT is shown in a different color. (c) Conceptually rolling up a graphene sheet (a single layer of graphite, see below) along a vector ( $C_h$ ) on the sheet into a SWCNT.[11] The graphene sheet is shown in grey. The SWCNT and the portion of graphene which is rolled to form the SWCNT are shown in red. (d) The  $(n,m)$  SWCNT naming scheme, or chirality, can be thought of as the vector ( $C_h$ ) that describes how to "roll up" the graphene sheet to make the SWCNT.[12]  $\theta$  is the chiral angle, and  $a_1$  and  $a_2$  are the unit vectors of the honeycomb crystal lattice of graphene. The integers  $n$  and  $m$  are chiral indices which denote the number of unit vectors along  $a_1$  and  $a_2$ , respectively. SWCNTs with  $n = m$  (known as armchair nanotubes) and those with  $n - m = 3j$ , where  $j = 0, 1, 2, 3, \dots$ , are metallic at room temperature (labeled green). SWCNTs with  $n - m = 3j + 1$  (labeled pink) and  $n - m = 3j + 2$  (labeled purple) are semiconductors with a bandgap that varies inversely with diameter. SWCNTs with  $m = 0$  are known as zigzag nanotubes and can be either metallic or semiconducting ..... 19

**Figure 1-2:** (a) Chemical structure of monolayer graphene.[21] (b) AB-stacked (Bernal stacking),[22] and (c) turbostratic bilayer graphene sheets.[22]..... 20

**Figure 1-3:** Various behaviors of surfactant molecules in bulk aqueous solutions (light blue square), and at liquid/vapor and liquid/solid interfaces. The air represents a hydrophobic vapor phase while the CNT represents a hydrophobic solid phase..... 22

**Figure 1-4:** (a) TEM (Transmission Electron Microscope) image of the cross-section of a SWCNT bundle.[44] (b) Schematic sketch of the exfoliation process of SWCNT bundles (cross-sectional view) into individually dispersed SWCNTs in a common bile salt surfactant (sodium cholate (SC)) solution.[39] (c) Schematic sketch of the exfoliation process of graphite flakes into graphene sheets of various thicknesses in a SC solution.[40]..... 23

**Figure 1-5:** Covalent functionalization of SWCNTs with a common diazonium salt reagent, tetrafluoroborate ( $BF_4^-$ ) *p*-Hydroxybenzene diazonium.[49] Diazonium ions react with (extract electrons from) the SWCNT sidewall, thereby evolving  $N_2$  gas and leaving a stable C-C covalent bond with the SWCNT surface. .... 24

**Figure 1-6:** Sequence of steps involved in a typical molecular dynamics (MD) simulation. .... 27

**Figure 2-1:** Schematic (top) and spatial (bottom) chemical structures of sodium cholate, a common bile salt surfactant, showing the rigid steroid-ring backbone, the hydrophobic and hydrophilic faces of the molecule, the hydroxyl groups ( $-\text{OH}$ ), and the charged carboxylate group ( $-\text{COO}^-$ ). Color code: red – oxygen, light green – carbon, and white – hydrogen. .... 32

**Figure 2-2:** Representative post-equilibrium simulation snapshots of a (6,6) SWCNT in aqueous SC solutions at two different total SC concentrations: (a) 75 mM and (b) 125 mM. The two plots on the left are side views and the two plots on the right are corresponding front views. Water molecules are not shown for clarity. Color code: red – oxygen, blue – sodium counterion, light green – carbon, white – hydrogen, and purple – carbon atoms in the SWCNT..... 39

**Figure 2-3:** Simulated radial distribution functions (RDFs) relative to the cylindrical axis of a SWCNT (“ $r$ ” is measured radially from this axis): (a) RDF of the cholate ions, (b) RDF of the carbon atoms of the charged carboxylate groups, and (c) RDF of the sodium counterions. The RDFs are plotted for low (corresponding to a total SC concentration of 75 mM) and high (corresponding to a total SC concentration of 125 mM) SC surface coverages. Note that the radius of the (6,6) SWCNT considered here is around 0.55 nm when excluded-volume effects are accounted for, and explains why the three RDF profiles shown remain zero for  $r \leq 0.55$  nm. 39

**Figure 2-4:** Simulated distribution profiles of the angle,  $\theta$ , between the principal axis of the cholate ions and the cylindrical axis of the SWCNT. Note that bias resulting from variations in solid angle has been removed by a weighting factor of  $(1/\sin \theta)$ . In the SC molecular structure shown, the dotted line connecting the carbon atom in the carboxylate group with the carbon atom at the end of the steroid ring defines the principal axis of the cholate ion (refer also to Figure 2-1). .... 45

**Figure 2-5:** (a) Simulated potential of mean force (PMF) corresponding to: (i) two parallel SWCNTs coated with cholate ions (solid line), and (ii) two parallel bare SWCNTs in vacuum (dashed line), as a function of the intertube separation,  $d$ . Note that the two PMF profiles overlap for  $d \leq 1.2$  nm, (b) Net contribution of SC to the PMF profile,  $\Delta\text{PMF}$ , corresponding to two parallel SWCNTs coated with cholate ions. The error bars (in blue) were computed using the block averaging method discussed in the text. Note that the y-axis in (b) has been rescaled relative to that in (a) for clarity. In addition, the designations (i) to (iv) in (b) correspond to plots (a) to (d) in Figure 2-7, where 2D atom number density plots of the cholate ions and the sodium counterions are shown at selected intertube separations in order to help explain the features exhibited by the  $\Delta\text{PMF}$  profile discussed in the text. .... 46

**Figure 2-6:** Simulated contour plot of the density profile of the sodium counterions (in units of  $\text{kg}/\text{m}^3$ ) along the x-axis of the simulation box (which is parallel to  $d$ ), as a function of the

intertube separation,  $d$ . The density scale is shown in the side color bar. As shown, the ion wall extends from an intertube separation of  $d = 1.7$  to  $d = 2.8$  nm. The locations of the two SWCNT cylindrical axes along the x-axis are shown by the two white dashed lines. .... 50

**Figure 2-7:** 2D atom number density plots of the cholate ions (left panel) and the sodium counterions (right panel) at selected intertube separations of: (a) 2.48 nm, (b) 2.00 nm, (c) 1.68 nm, and (d) 1.32 nm. These four intertube separations were selected in order to help explain the features exhibited by the PMF profile discussed in the text. The atom number density scale is shown in the bottom color bars. The density plots in (a) – (d) represent front views of the simulation box. The black rings denote the locations of the two parallel SWCNTs. .... 51

**Figure 2-A1:** Solvent accessible surface areas (SASAs) of: (a) a SWCNT and (b) the cholate ions under low and high SC surface coverages, monitored as a function of simulation time. As shown, the fluctuations in the SASA curves are significant at the beginning, and are dampened after about 200 ns, indicating that the system has reached equilibrium. Therefore, data analysis was performed during the last 20 ns of the entire simulation run, as indicated by the time period beyond the vertical dashed lines. .... 55

**Figure 2-A2:** Cumulative average forces as a function of simulation time at several selected intertube separations,  $d$ . As shown, the fluctuations in the force curves are significant at the beginning, and are dampened after about 10 ns, indicating that the system has reached equilibrium. Therefore, data analysis was performed during the last 5 ns of each simulation run, as indicated by the time period beyond the vertical dashed line. .... 55

**Figure 2-A3:** Zoomed-in plots of representative post-equilibrium simulation snapshots of a (6,6) SWCNT in aqueous SC solutions, showing that: (a) the cholate ions prefer to self-assemble side-by-side (perpendicular to the nanotube axis) in order to minimize contact of their hydrophobic faces with water, (b) the side-by-side self assembly is facilitated by the condensation of positively-charged sodium counterions onto the negatively-charged carboxylate group of a single cholate ion, and (c) the side-by-side self assembly is also facilitated by the condensation of a positively-charged sodium counterion onto the negatively-charged carboxylate groups of two cholate ions. Water molecules are not shown in all the plots for clarity. Note that in (a), the sodium counterions are also not shown for clarity, and all the irrelevant cholate ions are shown in a transparent fashion in order to highlight the relevant ones. In addition, in (b), all the irrelevant cholate ions and sodium counterions are shown in a transparent fashion in order to highlight the relevant ones. The color code is the same as that in Figure 2-2. .... 56

**Figure 2-A4:** Post-equilibrium MD simulation snapshots at intertube separations of: (a) 1.96 nm and (b) 1.68 nm, illustrating the orientation of the steroid-ring plane of one cholate ion when

only a single layer of cholate ions resides within the intertube gap. At  $d = 1.96$  nm, the plane in white orients perpendicular to the SWCNT surface in order to accommodate the fixed, sparsely-packed intertube gap, while at  $d = 1.68$  nm, the plane in white orients parallel to the SWCNT surface. .... 56

**Figure 3-1:** Representative post-equilibrium simulation snapshots of SC-stabilized monolayer graphene: (a) top view, (b) side view, and (c) chemical structure of the cholate ion. Water molecules are not shown for clarity. Note that in (a) and (b), SC is shown in the volume-filled form, while the graphene sheet is shown in the stick form. The cholate ions at the back of the graphene sheet can also be visualized in a darker fashion. Note that the orange dashed ellipse highlights two side-by-side self-assembled SC molecules. Color code: red – oxygen, blue – sodium, light green – carbon, white – hydrogen, and silver – graphene carbon. .... 65

**Figure 3-2:** (a) Simulated density profiles of water molecules, cholate ions, and sodium counterions along the z-axis normal to the monolayer graphene. Note that the z-axis was shifted so that the graphene sheet is located at  $z = 0$ . The water density profile for the simulation of graphene in water, without SC, is shown as the blue dashed line for comparison. Note also that the density of the sodium counterions was amplified 10 times for clarity. (b) Simulated distribution profile of the angles (with a  $1^\circ$  interval) between the principal axis of the cholate ions and the zigzag axis ( $0^\circ$ ) of graphene. In the SC molecular structure shown, the solid black line connecting the carbon atom in the carboxylate group with the carbon atom at the end of the steroid ring defines the principal axis of the cholate ion. Furthermore, the three red hexagonal rings represent the “armchair-like” cyclohexane rings in the cholate ion, while the orange pentagonal ring represents the cyclopentane ring in the cholate ion. .... 67

**Figure 3-3:** Simulated electrostatic potential around the graphene-SC assembly as a function of  $z$ , compared to that predicted based on the traditional Poisson-Boltzmann (PB) equation. The water density profile is shown for comparison purposes..... 70

**Figure 3-4:** (a) Simulated potential of mean force (PMF) between two parallel graphene-SC assemblies as a function of the intersheet separation,  $d$ . The fitting results to the simulated PMF data (shown in red circles) using Eq. (3-A1) in Appendix C corresponds to the red solid line. The predicted electrostatic repulsive potential using the DLVO theory corresponds to the blue dashed line, and is shown for comparison. Note that the arrow shows the position of the local minimum at  $d = 1.05$  nm in the PMF profile. (b) & (c) The contour plots of the density (in units of  $\text{kg}/\text{m}^3$ ) profiles of: (b) the sodium counterions, and (c) the cholate ions, both along the z-axis, as a function of  $d$ . The red-color regions illustrate the existence of: a sodium ion wall in (b), and a single layer of cholate ions in (c), both being confined by the two graphene sheets. Note that the



density increases as the color changes gradually from blue to red. Note also that the white dashed lines denote the z-axis positions of the graphene sheets, as a function of  $d$ . ..... 73

**Figure 3-5:** (a) Post-equilibrium simulation snapshot of the metastable bilayer graphene-SC assembly at an intersheet separation of  $d = 1.05$  nm, showing a single layer of cholate ions and a sodium counterion wall confined between the two graphene sheets. Water molecules are not shown for clarity. The color code is the same as in Figure 3-1. (b) The simulated density profiles of the cholate ions and the sodium counterions along the z-axis, showing a single layer of cholate ions and a sodium counterion wall (both peaked at  $z = 0$  nm) being confined between the two graphene sheets located at  $d = 1.05$  nm (or at  $z = \pm 0.525$  nm, as pointed out by the two arrows). Note that the other four peaks (two peaked at  $z = \pm 0.9$  nm and two peaked at  $z = \pm 1.15$  nm) show the adsorbed cholate ions and sodium counterions at the outer surfaces of the two graphene sheets. .... 78

**Figure 3-6:** (a) Measured optical absorbance (at 660 nm wavelength) per unit path length ( $A/l$ ) as a function of the total graphene mass concentration,  $C$ . Note that three different samples (corresponding to the red, blue, and green symbols) were prepared using the same procedure. (b) Time-dependent graphene total mass concentration,  $C(t)$ , as a function of time. The red line denotes the numerical fitting results from Eqs. (3-A1)–(3-A6) in Appendix C. The errors in the experimental results (the black markers) were obtained from the standard deviations in the optical absorbance of the three cuvette samples. (c) Predicted time-dependent number concentrations of graphene with various layer numbers,  $N_i(t)$ , as a function of time. Note that 6-layer graphene is used to represent thicker multilayer graphene. (d) Predicted distributions of graphene layer numbers as a function of time. Note that the circles are the actual values, and each line that smoothly connects the circles is just a guide to the eye. .... 81

**Figure 3-7:** (a) Re-aggregation mechanisms of turbostratic bilayer and trilayer graphene. The turbostratic bilayer graphene results from the re-aggregation of two monolayer graphene sheets. The turbostratic trilayer graphene results from the re-aggregation of one AB-stacked bilayer graphene and one monolayer graphene (type I), or from the re-aggregation of one turbostratic bilayer graphene and one monolayer graphene (type II). (b) Predicted time-dependent concentrations of AB-stacked bilayer graphene (red line) and turbostratic bilayer graphene (blue line). (c) Predicted time-dependent concentrations of AB-stacked trilayer graphene (red line) and turbostratic trilayer graphene (type I — blue line, and type II — green line). .... 84

**Figure 3-A1:** Solvent accessible surface areas (SASAs) of a graphene monolayer and the cholate ions, monitored as a function of simulation time. As shown, the fluctuations in the SASA curves are significant at the beginning, and are dampened after about 200 ns, indicating that the system

has reached equilibrium. Therefore, data analysis was performed during the last 50 ns of the entire simulation run, as indicated by the time period beyond the vertical dashed line. .... 89

**Figure 3-A2:** Cumulative average forces as a function of simulation time at several selected inter-sheet separations,  $d$ . As shown, the fluctuations in the force curves are significant at the beginning, and are dampened after about 10 ns, indicating that the system has reached equilibrium. Therefore, data analysis was performed during the last 5 ns of each simulation run, as indicated by the time period beyond the vertical dashed line..... 89

**Figure 4-1:** Chemical structures of the surfactants and the diazonium salt considered in this study: (a) sodium cholate (SC), (b) sodium dodecyl sulfate (SDS), (c) cetyl trimethylammonium bromide (CTAB), and (d) tetrafluoroborate ( $\text{BF}_4^-$ ) aryl diazonium. The bile salt SC has rigid steroidal backbones, which results in hydrophobic and hydrophilic “faces”. Therefore, SC can also be referred to as a “facial” surfactant. The rigidity of the SC molecules leads them to form a monolayer structure on the nanotube surface.[158] The flexible linear surfactants, SDS and CTAB, possess less rigid, hydrophobic chains, which tend to coat the nanotube in a more disordered manner at high surface coverages.[91] (e) Schematic of the equilibrium model proposed here, showing the three possible states of the diazonium ion during the functionalization process: (i) free in the surfactant aqueous solution, (ii) adsorbed on the SWCNT-surfactant complex (with an adsorption constant  $K_A$ ), and (iii) covalently bound to the SWCNT surface (with a reaction constant  $K_R$ ). Adsorbed surfactant molecules are shown as blue beads (the hydrophilic surfactant heads) connected with red lines (the hydrophobic surfactant tails)..... 97

**Figure 4-2:** Post-equilibrium simulation snapshots of SWCNTs covered with surfactants, showing the surface structures of the various surfactants considered here. (a) and (b) for the SC case, (c) and (d) for the SDS case, and (e) and (f) for the CTAB case. Within each row, the side view is on the left and the front view is on the right. (a), (c), and (e) correspond to low surfactant surface coverages, while (b), (d), and (f) correspond to high surfactant surface coverages. Water molecules and counterions are not shown for clarity. Color code: red – oxygen, light blue – carbon, white – hydrogen, dark blue – nitrogen, and purple – carbon in the SWCNT..... 101

**Figure 4-3:** Simulated PMF profiles between the diazonium ion and the SWCNT-surfactant complexes corresponding to SC, SDS, and CTAB for both low and high surface coverages. The no surfactant case (that is, the bare SWCNT in water) is also shown for comparison. The error bars in green, corresponding to the simulated no surfactant case, represent the typical errors in the PMF calculations for the surfactant cases simulated here ( $< 2 k_B T$ ). The inset shows a schematic drawing of the cylindrical axis ( $z$ -axis) of the SWCNT (the black arrow), the

constraint distance,  $r$ , between this axis and the diazonium ion (the red arrow), and the cylindrical surface on which the diazonium ion can move freely (the black dashed lines). The simulation snapshot of the high-surface coverage SWCNT-SC complex is used here. Water molecules and counterions are not shown for clarity. The color code is the same as the one used in Figure 4-2..... 103

**Figure 4-4:** (a) Interaction potential energy between the diazonium ion and SC, SDS, and CTAB molecules adsorbed on the SWCNT surface at high surfactant surface coverages, as a function of  $r$ . (b) The Lennard-Jones (LJ) contribution to the potential energy in (a), which reflects both the vdW and the steric interactions between the diazonium ion and the surfactant molecules. (c) The Coulombic (Coul) contribution to the potential energy in (a), which reflects the electrostatic interactions between the diazonium ion and the surfactant molecules. .... 107

**Figure 4-5:** Projected density maps of charged surfactant head groups on the unrolled SWCNT surface (tube length  $\times$  tube circumference) for: SDS (top row), SC (middle row), and CTAB (bottom row). Within each plot, the diazonium ion approaches the SWCNT-surfactant complex gradually from the left to the right, where the left subplot:  $r = 3.3$  nm, middle subplot:  $r = 1.7$  nm, and right subplot:  $r = 1.1$  nm. The y-axis measures the circumference of the SWCNT, and the z-axis measures the length of the SWCNT. Density maps are shown as contour plots with arbitrary units. Color bar code: lighter color corresponds to high surfactant head densities and darker color corresponds to low surfactant head densities. The origin of each plot at  $y = z = 0$  denotes the projected position of the charged diazo group ( $-N^+ \equiv N$ ) of the diazonium ion. Each density map was averaged over the last 20 ns of each simulation. Representative simulation snapshots showing the binding of the diazonium ion (the blue arrows) to the charged surfactant layer on the SWCNT surface are shown at the bottom of the density maps corresponding to  $r = 1.1$  nm. The color code is the same as the one used in Figure 4-2. Note that the diazonium ion and the various SWCNT-surfactant complexes are drawn in the “Licorice” and the “Surf” representation in VMD,[188] respectively, to facilitate distinction between the two..... 109

**Figure 4-6:** (a) Experimental data (circles) and theoretical fitting results (solid lines) for the extents of functionalization ( $f_{(7,5)}^{SC}$ ,  $f_{(7,5)}^{SDS}$ , and  $f_{(7,5)}^{CTAB}$ ) as a function of the diazonium/carbon molar ratio. The solid lines were predicted using Eq. (4-9), and the corresponding fitting parameters are listed in Table 4-1. (b) Predicted diazonium ion surface coverage (adsorption isotherm),  $\theta_A$  (in units of number of diazonium ions per nm of a SWCNT), as a function of the diazonium/carbon molar ratio, using Eq. (4-6) and the fitting parameters listed in Table 4-1. .... 115

**Figure 4-A1:** Representative coordinates ( $x$ ,  $y$ , and  $z$ ) of the charged diazo group ( $-N^+ \equiv N$ ) in the diazonium ion as a function of the simulation time for a: (a) SWCNT-SDS complex, (b)

SWCNT-SC complex, and (c) SWCNT-CTAB complex. Left:  $r = 3.3$  nm, middle:  $r = 1.7$  nm, right:  $r = 1.1$  nm, corresponding to the density maps in Figure 4-4 in the main text. Note that  $z_{\max} \approx 6$  nm,  $x_{\max} = y_{\max} \approx 7$  nm, and the nanotube axis along the z-axis is located at  $x = y = 3.5$  nm. .... 121

**Figure 4-A2:** Representative SWCNT fluorescence spectra and spectra deconvolution. The blue curve represents the original spectra data, the 9 black curves represent the deconvoluted spectra corresponding to  $N = 9$  Lorentzian lineshapes (8 nanotube peaks and 1 G-prime peak), and the red curve represents the fitted result (i.e., the summation of the 9 black curves) to the blue curve. .... 123

## List of Tables

<b>Table 2-1:</b> Population Analysis Results and Relevant Experimental Data .....	42
<b>Table 2-A1:</b> Summary of Simulated Systems .....	54
<b>Table 3-A1:</b> Summary of Simulated Systems .....	88
<b>Table 3-A2:</b> Summary of Fitted Parameters in Eq. (3-A1). Note that $\varepsilon$ , $\beta_1$ , $\beta_2$ , and $\alpha$ are in units of kJ/mol·nm <sup>2</sup> , $r_0$ , $r_1$ , $\sigma_1$ , $r_2$ , $\sigma_2$ , and $r_3$ are in units of nm, and $\kappa$ is in units of nm <sup>-1</sup> . .....	92
<b>Table 4-1:</b> Summary of parameter values for $A = P\theta_{TR}$ , $\theta_{TA}$ , and $K_R$ in Eq. (4-9) by fitting to the experimental values of $C_0$ and $f_{(m,n)}^i$ (see Figure 4-6-a) with constants $l$ and $K_A$ using the simulated $\Delta G_A$ values in Eq. (4-4) .....	116
<b>Table 4-A1:</b> Partial atomic charges of the diazonium ion used in the molecular dynamics (MD) simulations. The color code for the diazonium ion chemical structure is the same as in Figure 4-2 in the main text. Note that charge symmetry was enforced to determine partial charges based on results from quantum mechanics (QM) calculations. ....	120

# Chapter 1

## Introductions

### 1.1 Overview of Carbon Nanotubes (CNTs) and Graphene

Nanoscience and nanotechnology strive to understand and employ the unique properties of nanoscale materials for the development of revolutionary technologies. Some of the nanoscale materials with the highest potential to fulfill this goal are the two recently discovered allotropes of carbon: carbon nanotubes (CNTs) and graphene, due to their extraordinary electrical, thermal, mechanical, and optical properties.[1, 2]

CNTs are cylindrical tubes of  $sp^2$ -hybridized carbon atoms with diameters of  $\sim 1$  nm (Figure 1-1). Since their discovery in transmission electron microscope (TEM) images in 1991,[3] the physical properties of CNTs have been extensively studied. CNTs can exist in single- (Figure 1-1-a) or multi-walled forms (Figures 1-1-b). Despite their small diameters, CNTs vary in length from  $\sim 10$  nm all the way up to  $\sim 1$  cm.[4] CNTs are exceptionally strong and stiff; they have the largest tensile strength and elastic modulus of any known material.[5] CNTs are extremely lightweight as a result of the hollow tubes of low mass carbon atoms, which makes them ideal for use in lightweight, high-strength composite materials.[6] Depending on the direction in which a graphene sheet (a single layer of graphite, see below) is rolled up (see Figure 1-1-c), SWCNTs can behave either as semiconductors, or as metals (see Figure 1-1-d).[7] The quasi-one-dimensional structure of SWCNTs gives them a characteristic, spike-like electronic density of states, resulting in sharply peaked absorption and emission spectra.[8] The orbital misalignment induced by the curvature of the SWCNTs makes them more amenable to functionalization than graphene, and their large specific surface area facilitates the physical adsorption of molecules through non-covalent attractions.[9] Due to these unique chemical and electronic properties, practical applications of SWCNTs include logic gates, field emission sources, scanning probes, conductive films, electromechanical actuators, super-capacitors, and sensors.[10]

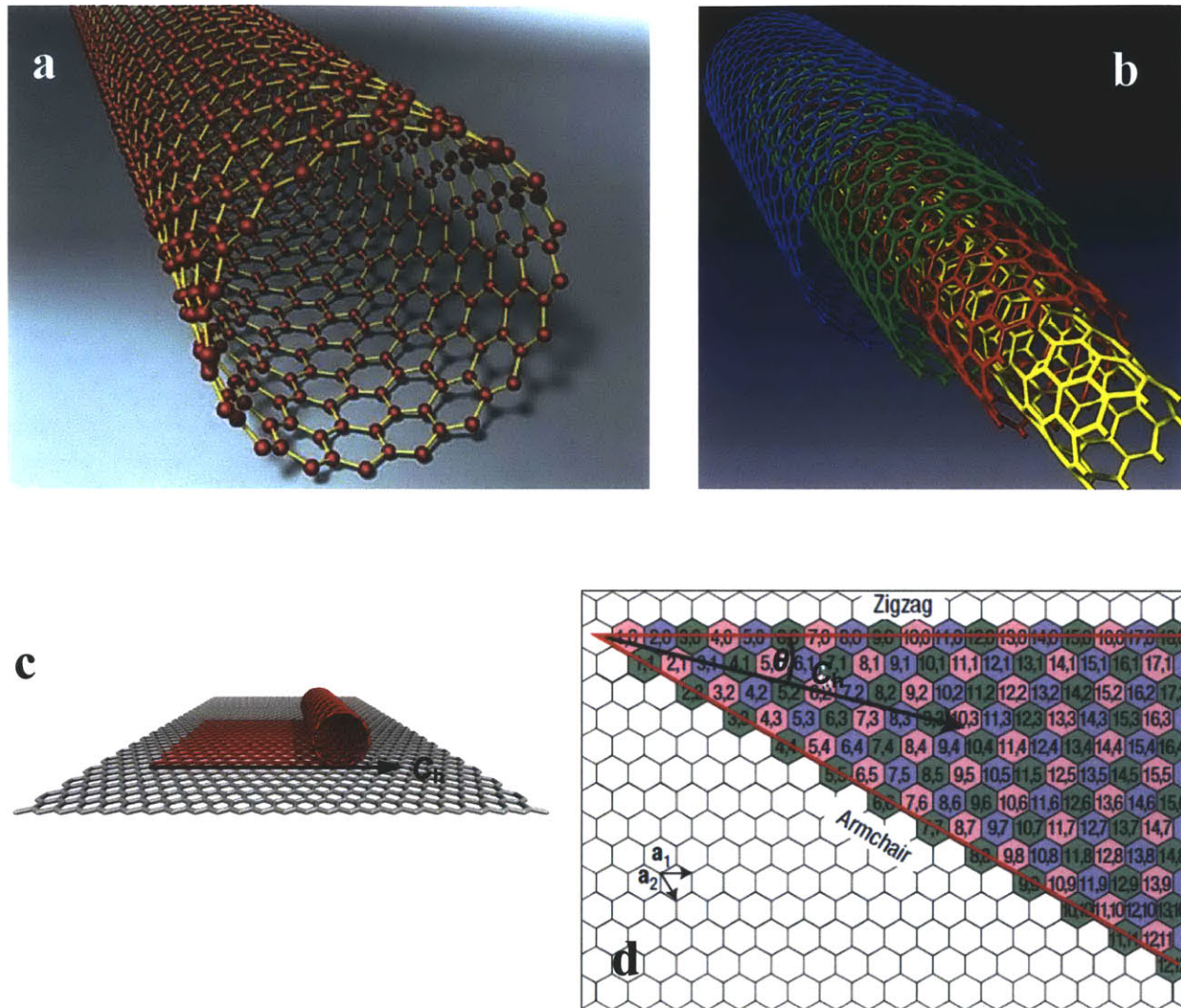


**Figure 1-1:** Chemical structure and electronic property of CNTs. (a) A single-walled carbon nanotube (SWCNT). Carbon atoms and the covalent bonds between them are shown in red and yellow, respectively.[11] (b) A multi-walled carbon nanotube (MWCNT).[11] Each SWCNT is shown in a different color. (c) Conceptually rolling up a graphene sheet (a single layer of graphite, see below) along a vector ( $C_h$ ) on the sheet into a SWCNT.[11] The graphene sheet is shown in grey. The SWCNT and the portion of graphene which is rolled to form the SWCNT are shown in red. (d) The  $(n,m)$  SWCNT naming scheme, or chirality, can be thought of as the vector ( $C_h$ ) that describes how to "roll up" the graphene sheet to make the SWCNT.[12]  $\theta$  is the chiral angle, and  $a_1$  and  $a_2$  are the unit vectors of the honeycomb crystal lattice of graphene. The integers  $n$  and  $m$  are chiral indices which denote the number of unit vectors along  $a_1$  and  $a_2$ , respectively. SWCNTs with  $n = m$  (known as armchair nanotubes) and those with  $n - m = 3j$ , where  $j = 0, 1, 2, 3, \dots$ , are metallic at room temperature (labeled green). SWCNTs with  $n - m = 3j + 1$  (labeled pink) and  $n - m = 3j + 2$  (labeled purple) are semiconductors with a bandgap that varies inversely with diameter. SWCNTs with  $m = 0$  are known as zigzag nanotubes and can be either metallic or semiconducting.



On the other hand, the discovery of two-dimensional, one-atom-thick graphene (see Figure 1-2-a) in 2004 using the simple “Scotch-tape method” has led to a revolution in condensed matter physics.[13, 14] Due to the different electronic band structures of graphene relative to that of bulk, three-dimensional graphite, graphene is generally defined as sheets consisting of fewer than 10 stacked layers of  $sp^2$ -hybridized carbon lattices.[15] Monolayer graphene is a semiconductor having zero bandgap. The electronic dispersion is conical near the crossing of the valence and conduction bands with vertices that meet at the  $K$  point (Dirac point) of the Brillouin zone.[16] On the other hand, just with one additional graphene layer, bilayer graphene has an entirely different band structure. In fact, the inversion symmetric AB-stacked bilayer graphene is also a zero-bandgap semiconductor in its pristine form. However, a non-zero bandgap can be induced by breaking the inversion symmetry of the two layers.[17, 18] Interestingly, the bandgap may be tuned by applying an electric field perpendicular to the sample.[19] In contrast, trilayer graphene is a semimetal with a band overlap which can also be controlled by applying an external electric field.[20] As a result of these unique properties, bilayer and trilayer graphene have extraordinary potential for next-generation optoelectronic and microprocessor applications.

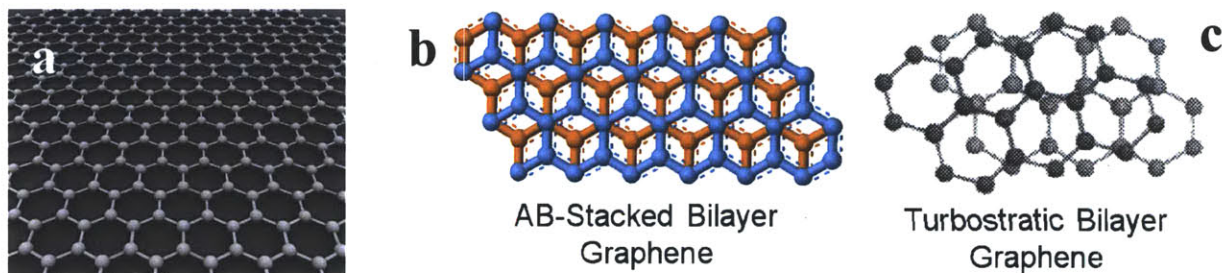


**Figure 1-2:** (a) Chemical structure of monolayer graphene.[21] (b) AB-stacked (Bernal stacking),[22] and (c) turbostratic bilayer graphene sheets.[22]

Micromechanically-cleaved graphene [13, 14] (obtained using the “Scotch-tape method”) provides the first platform for the investigation of the fundamental physics associated with graphene. Mono- and few-layer graphene flakes are exfoliated by direct stamping or via an



intermediary adhesive tape from the surface of Highly-Ordered Pyrolytic Graphite (HOPG). Although this method provides the highest quality of graphene due to the excellent crystallinity of HOPG, the mono- and bi-layer graphene yield is very low and the process is extremely time-consuming. It is unlikely that this method will be amenable to large-scale production of graphene.[23] Alternatively, large-scale graphene films have been produced based on the kinetics of epitaxial growth on top of other crystals.[15] Annealing of single-crystalline Silicon Carbide (SiC) substrates[24] in ultra-high vacuum was considered the most promising route to produce graphene wafers due to the insulating substrate. However, the requirements of high-quality substrate and processing conditions limit the use of this method. Furthermore, the graphene films are bound to the substrate sufficiently strongly such that the subsequent transfer of the graphene films onto other surfaces is not possible. Tremendous progress has been made using chemical vapor deposition (CVD) for graphene growth on poly-crystalline Ni and Cu films.[25-27] This method allows the flexibility of transferring the produced film to arbitrary substrates by wet-etching the underlying metal film. The technique has been scaled up to roll-to-roll production, and the production of a 30-inch graphene film on a flexible substrate for replacing traditional indium tin oxide (ITO) conducting films has been demonstrated.[28] However, for all epitaxial growth methods, the epitaxial multilayers tend to be “turbostratic”, which means that the Bernal stacking between graphitic layers has random disorders (see Figures 1-2-b and 1-2-c). Slight deviations from the natural AB stacking arrangement affect interlayer interactions, and can even induce electronic properties which are similar to those of monolayer graphene.[29] As a result, the distinct properties of micromechanically-exfoliated bilayer and trilayer graphene cannot be reproduced.

## **1.2 The Role of Surfactants in CNT and Graphene Solutions**

Surfactants, or surface active agents, are chemicals exhibiting amphiphilic behavior towards a solvent (e.g., water).[30-32] Each surfactant molecule possesses a hydrophobic (water fearing) “tail” and a hydrophilic (water loving) “head” (see Figure 1-3). This amphiphilic character leads

to increased activity at various types of interfaces (e.g., liquid/vapor and liquid/solid, see Figure 1-3), as well as to self-assembly into micellar aggregates (see Figure 1-3) beyond a threshold surfactant concentration (referred to as the CMC, the Critical Micelle Concentration) in bulk aqueous solutions.[30-32] As a result of these unique attributes, surfactants are used in many pharmaceutical, industrial, and environmental applications, including biological separations,[33, 34] fat metabolism during digestion,[33] drug delivery,[35] enhanced-oil recovery (EOR),[36, 37] nanomaterial dispersion and sorting,[38-40] and water purification.[41, 42] Selection of the appropriate surfactant for a given application is often motivated by the need to: (i) control bulk solution micellization properties (e.g., the CMC and the micelle shape and size), (ii) reduce interfacial tensions between two phases, and (iii) stabilize aqueous dispersed systems, such as carbon nanotubes and graphene sheets. Clearly, the ability to make a priori molecular-level predictions of surfactant properties for applications (i) – (iii) would allow formulators in industry to speed up the design and optimization of new surfactant formulations, and would also allow academic and industrial researchers to obtain a better understanding of the fundamental mechanisms behind surfactant organization phenomena in various environments (in the bulk and at interfaces).

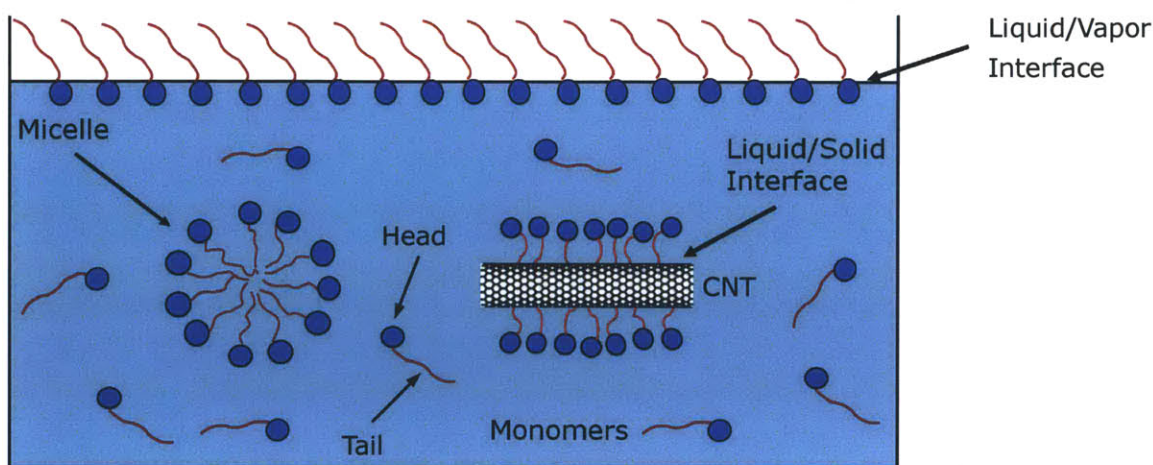


**Figure 1-3:** Various behaviors of surfactant molecules in bulk aqueous solutions (light blue square), and at liquid/vapor and liquid/solid interfaces. The air represents a hydrophobic vapor phase while the CNT represents a hydrophobic solid phase.

The discovery of CNTs and graphene sheets offers exciting opportunities for the development of novel materials. Uniform aqueous dispersion and solution-phase sorting of CNTs and graphene sheets are critical challenges that must be met to successfully produce such materials,[43] since they tend to self-associate into micro-scale aggregates (bundles in the case of CNTs,[44] see Figure 1-4-a, and thick flakes in the case of graphene,[45] see Figure 1-4-c). In addition, they are quite polydisperse when made using current technologies (e.g., the diameter of SWCNTs usually varies from 0.8 to 2 nm,[1] and the thickness of graphene sheets usually varies from a single layer up to hundreds of layers[23]). This results in products with inferior mechanical and electric performance. Recognizing this problem, extensive and successful research has been reported in the literature on the development of dispersion and sorting technologies based on both mechanical (e.g., ultrasonication and ultracentrifugation in surfactant solutions, see Figures 1-4-b and 1-4-c), and chemical (e.g., covalent chemical functionalization, see Figure 1-5) approaches.[39, 40, 46-49]

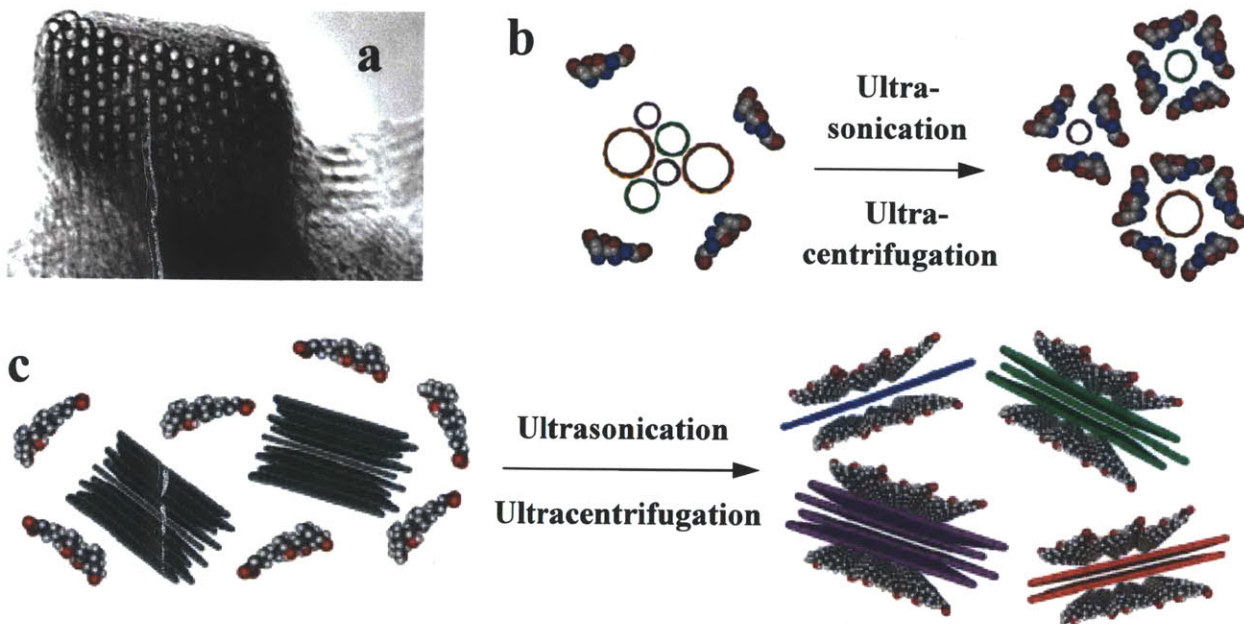


**Figure 1-4:** (a) TEM (Transmission Electron Microscope) image of the cross-section of a SWCNT bundle.[44] (b) Schematic sketch of the exfoliation process of SWCNT bundles (cross-sectional view) into individually dispersed SWCNTs in a common bile salt surfactant (sodium cholate (SC)) solution.[39] (c) Schematic sketch of the exfoliation process of graphite flakes into graphene sheets of various thicknesses in a SC solution.[40]



Furthermore, as an alternative to the ‘Scotch-tape method’ and the epitaxial growth method to produce graphene (discussed in Section 1.1), exfoliation of pristine graphite in a liquid phase, as shown in Figure 1-4-c, is easily scalable similar to many ‘conducting inks’, is amenable to printing technologies, and also allows for more precise chemical modification in solution.[43, 50] The liquid-phase production of chemically-converted graphene from graphene oxide (GO) is a popular and high-yield method for graphene-based solutions.[51-54] In spite of producing high-concentration dispersions containing large flake areas, a substantial number of defects are introduced during the reduction process,[55, 56] which only lead to partial restoration of the intrinsic properties of graphene.[57] Liquid-phase exfoliation of graphite in organic solvents[58-60] and surfactant aqueous solutions[40, 45] are promising routes to produce pristine, unfunctionalized graphene dispersions.

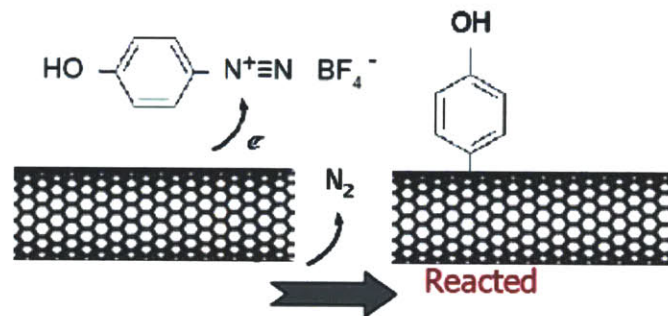


**Figure 1-5:** Covalent functionalization of SWCNTs with a common diazonium salt reagent, tetrafluoroborate ( $\text{BF}_4^-$ ) *p*-Hydroxybenzene diazonium.[49] Diazonium ions react with (extract electrons from) the SWCNT sidewall, thereby evolving  $\text{N}_2$  gas and leaving a stable C–C covalent bond with the SWCNT surface.

Covalently functionalized CNTs (see Figure 1-5) have been utilized for a variety of applications,[61] ranging from drug-delivery vehicles[62] to molecular sensors,[63, 64] and are promising materials for the development of both optical[65] and mechanical[66] switches. However, for such applications as electronic sensors and actuators, the introduction of covalent defect sites to the highly conjugated nanotube sidewall significantly alters the electronic properties of the nanotube, which in the case of single-walled carbon nanotubes (SWCNTs) can

substantially hinder tube conductance.[67, 68] Additionally, in the case of semiconducting SWCNTs, such defect sites can quench nanotube fluorescence along a length of approximately 140–240 nm,[69, 70] thereby inhibiting the use of covalently modified nanotubes for fluorescence sensing applications. Accordingly, there is interest in developing a means of controlling the degree of covalent functionalization, such that the majority of the properties of pristine nanotubes are preserved. Because surfactants stabilize nanoparticles by a variety of mechanisms, from Coulombic forces to steric exclusion and thermal fluctuations,[32] it should be expected that these adsorbed layers will also influence the ability of a reagent molecule to access the nanoparticle surface.

In summary, surfactants play a very important role in functional CNTs and graphene via: (i) stabilizing CNTs and graphene in aqueous solutions for further chemical processing, species sorting, and solution-phase applications, and (ii) controlling the functionalization (both non-covalent and covalent) process of CNTs and graphene (note that the graphene functionalization case is not studied here, but interesting readers are referred to Refs. [71-73]). It is useful to explore the role of surfactants using molecular dynamics (MD) simulations (see Section 1.3) and theoretical modeling for three reasons: (i) the structure of the adsorbed surfactant molecules on CNTs and graphene can be studied at the molecular-level to help understand their role in the various solution-phase applications of these two important nanomaterials, (ii) the surfactant-induced dispersion stability can be quantified and understood to help design dispersants that can stabilize CNTs and graphene in aqueous solutions more efficiently, and (iii) the interactions of CNT/graphene–surfactant complexes with the diazonium salts can be quantified and understood to help direct and control the chemical functionalization of CNTs and graphene.

### **1.3 Overview of Molecular Dynamics (MD) Simulations**

Computer simulations of molecular systems are used to estimate equilibrium or dynamic properties of these systems. Computer simulations allow investigations of complex, many-body

systems for which analytical, closed-form solutions do not exist. Two of the most popular computer simulation methods used today are molecular dynamics (MD) and Monte Carlo (MC) simulations. Both methods can be used to determine equilibrium properties, while the MD method can also be used to determine dynamic properties. Frequently, properties of interest depend on the positions and momenta of all the particles present in a system. Given this dependence, the instantaneous value of the property of interest,  $A$ , can be expressed as  $A(p^N(t), r^N(t))$ , where  $p^N(t)$  represents the momenta of the  $N$  particles at time  $t$ , and  $r^N(t)$  represents the positions of the  $N$  particles at time  $t$ . The instantaneous value of the property  $A$  may fluctuate with time, and it is frequently useful to determine the time average value of the property,  $A_{ave}$ , through integration [74]:

$$A_{ave} = \lim_{\tau \rightarrow \infty} \frac{1}{\tau} \int_{t=0}^{\tau} A(p^N(t), r^N(t)) dt \quad (1-1)$$

In MD simulation, the time evolution of a system is determined by solving Newton's equations of motion. To this end, a potential energy model (referred to as a "force field") must be used to describe the intermolecular and intramolecular interactions of each of the system components. The forces acting on each particle in the system are determined through differentiation of the potential energy model. Once the force acting on each particle is known, trajectories which describe how the positions, velocities, and accelerations of the particles respond to these forces are computed numerically by incrementing forward in time with small time steps, and using an integration technique such as the velocity Verlet or the leap-frog algorithm [74]. A flowchart illustrating the computational steps involved in a typical MD simulation is shown in Figure 1-6. The force field and simulation parameters implemented in this thesis are discussed in detail in the Methods of Chapters 2 to 4 (Sections 2.2.1, 3.2.1, and 4.2.1). Interested readers are referred to Refs. [74, 75]

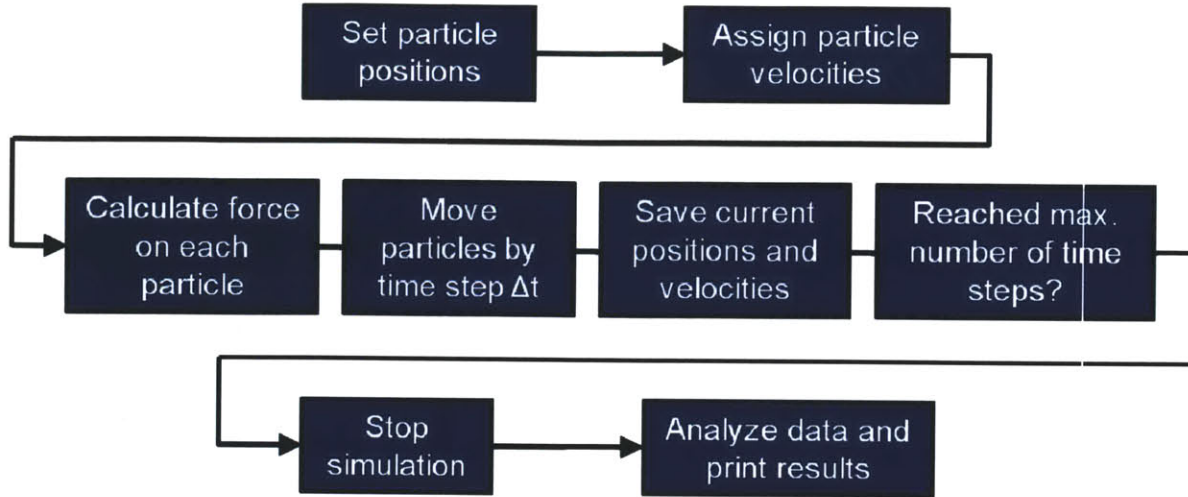


**Figure 1-6:** Sequence of steps involved in a typical molecular dynamics (MD) simulation.

At the end of an MD simulation with  $S$  time steps, averaged properties are determined as follows [74]:

$$A_{ave} = \frac{1}{S} \sum_i^S A(p^N(i), r^N(i)) \quad (1-2)$$

An alternative to determining a time average value of the property  $A$  of interest is to calculate the ensemble average, or the expectation value. In this approach, a large number of replicas of the system of interest are considered simultaneously. The ensemble average, usually determined in an MC simulation, can be expressed mathematically as follows [74]:

$$\langle A \rangle = \iint A(p^N, r^N) \rho(p^N, r^N) dp^N dr^N \quad (1-3)$$

where  $\rho(p^N, r^N)$ , the probability density of the ensemble, is the probability of finding a configuration with momenta  $p^N$  and positions  $r^N$ . Although only a double integral sign is shown, in practice, the integration is carried out over all  $6N$  momenta and positions of the particles present in the system. Therefore, in this approach, the average value of the property  $A$  is determined by averaging over all possible configurations of the system rather than by taking a time average. In accordance with the ergodic hypothesis, which is one of the fundamental axioms of statistical mechanics, the ensemble average  $\langle A \rangle$  can be considered equal to the time average

$A_{ave}$  under certain conditions. In particular, in MD simulations, the ergodic hypothesis holds by assuming no correlation among each system trajectory frame that one outputs for studying. Therefore, the average, or expectation value, of the property  $A$  is obtained from MD simulations as follows [74]:

$$\langle A \rangle = A_{ave} = \frac{1}{M} \sum_i^M A(p^N(i), r^N(i)) \quad (1-4)$$

where  $M$  is the number of trajectory frames outputted for studying. Note that  $M$  may be equal to the number of simulation time steps  $S$ , or it may be the number of trajectory frames outputted at regular time steps.

## 1.4 Thesis Overview

The remainder of this thesis is devoted to the use of molecular dynamics (MD) simulations and theoretical modeling to understand the role of surfactants in dispersing and sorting SWCNTs and graphene sheets, as well as in controlling the functionalization process of SWCNTs with diazonium salts. Each Chapter was written based on my published work in a peer-reviewed journal. It is noteworthy that extensive computational resources were used to complete the MD simulations presented in this thesis, in particular, for the time-consuming potential of mean force (PMF) calculations. Every nanosecond of the simulation takes between 2 to 5 hours on a 2.4 GHz 8-core CPU processor, which varies depending on the size of the actual simulated system. As a result, each Chapter (2, 3, and 4) presented below represents a net computer wall-clock time of 2 to 5 months. Running each simulation in parallel on multiple 8-core processors (e.g., 2 to 4) can significantly speed up the simulation, but the enhancement will reach a plateau due to slower communications among the different processors which are wired through the switch.

In Chapter 2 of this thesis, I report the first detailed large-scale all-atomistic MD simulation study of the adsorption and surface self-assembly structure of sodium cholate (SC) on a SWCNT in aqueous solution. In addition, I carry out a series of simulations to compute the potential of



mean force (PMF) between two parallel SC-covered SWCNTs as a function of the intertube separation. This study can enhance our quantitative and qualitative understanding of the role of bile salts such as SC in enhancing the dispersion stability of individual SWNTs in aqueous solution. Moreover, this study may shed light on the future design of novel surfactants capable of more efficiently stabilizing aqueous dispersions of nanoscaled materials.

In Chapter 3 of this thesis, I successfully combined MD simulations, theoretical modeling, and experimental measurements to address challenges in solution-phase graphene production. First, I probe the surface structure and electrostatic potential of monolayer graphene dispersed in a SC surfactant aqueous solution. Subsequently, I quantify the interactions between two graphene-SC assemblies by calculating the PMF between two SC-covered graphene sheets. Finally, the lifetime and time-dependent distribution of various graphene layer types are predicted using a kinetic model of colloid aggregation, and each graphene layer type is further decomposed into subtypes, including the AB-stacked species and various turbostratic species. The kinetic model of colloid aggregation developed here can serve as a useful tool to evaluate the quality of graphene dispersions for subsequent substrate-transferring or functionalization processes.

In Chapter 4 of this thesis, I successfully combine MD simulations and equilibrium reaction modeling to understand and model the extent of diazonium functionalization of SWCNTs coated with various surfactants (SC, sodium dodecyl sulfate (SDS), and cetyl trimethylammonium bromide (CTAB)). I show that the free energy of diazonium adsorption, determined using the PMF calculations, can be used to rank surfactants in terms of the extent of functionalization attained following their adsorption on the nanotube surface. The difference in binding affinities between linear and rigid surfactants is attributed to the synergistic binding of the diazonium ion to the local “hot/cold spots” formed by the charged surfactant heads. A combined simulation-modeling framework is developed to provide guidance for controlling the various sensitive experimental conditions needed to achieve the desired extent of SWCNT functionalization.

In Chapter 5 of this thesis, I conclude by: (i) providing a summary of the important findings and conclusions of the research presented, and (ii) proposing future research directions in this area.

## **Chapter 2**

### **Role of the Bile Salt Surfactant Sodium Cholate (SC) in Enhancing the Aqueous Dispersion Stability of Single-Walled Carbon Nanotubes: A Molecular Dynamics Simulation Study**

#### **2.1 Introduction**

As discussed in Section 1.2, since the first successful use of surfactants to disperse carbon nanotubes, a highly water insoluble material, in aqueous solution,[76] surfactants have played a very important role in the standard procedure used to prepare aqueous dispersions of single-walled carbon nanotubes (SWCNTs).[38, 44, 77, 78] Specifically, this widely-recognized, surfactant-aided dispersion process involves the application of an external energy input (ultrasound) to separate nanotubes at the bundled end by overcoming the strong van der Waals (vdW) attractions between them.[78, 79] Subsequently, the separated bundled ends provide new adsorption sites for the surfactant molecules. As a result, the repulsive potential energy resulting from the adsorbed surfactant molecules (electrostatic for ionic surfactants and steric for nonionic surfactants) further enhances this separation process.[76, 77, 79] In the case of ionic surfactants, the electrostatic repulsion between the surfactant-covered SWCNTs has been quantified experimentally by measuring the zeta potential of the surfactant-SWCNT assembly using electrophoresis.[43] Eventually, in a so-called “unzipping” fashion, individually isolated surfactant-coated carbon nanotubes are released to the aqueous solution.[79] This process involving the non-covalent dispersion of SWCNTs in aqueous solution is essential for many applications of carbon nanotubes, including their use as chemical and biological sensors in aqueous environments such as living cells.[80-82]

In recent years, significant effort has been devoted to: (i) better understand the unzipping mechanism, and (ii) screen through many types of surfactants for the preparation of high-weight fraction, aqueous solutions of SWCNTs, including ranking of surfactants in terms of their ability to solubilize unbundled SWCNTs.[38, 77-79, 83-85] In order to obtain a high-quality SWCNT aqueous solution for practical applications, surfactants are not only required to increase the weight fraction (or the solubility) of unbundled SWCNTs, but also to stabilize the individual nanotubes against rebundling, thus increasing the shelf life of these colloidal dispersions. In particular, the anionic surfactant SDS has been used extensively to separate SWCNT bundles, as well as to stabilize individual nanotubes with the aid of ultrasonication.[76, 78]

Very recently, more attention has been devoted to bile salts, the biological detergents, which have been shown to solubilize individual SWCNTs in aqueous solution with high weight fractions.[85] In particular, the most common bile salt, sodium cholate (SC), has been utilized to both separate and sort SWCNTs according to their different diameters and electronic properties with the aid of both ultrasonication and ultracentrifugation.[12, 39] Bile salts, unlike conventional linear surfactants like SDS, are rigid facial amphiphiles (referred to as “two-faced detergents”; see Figure 2-1 for the chemical structure of SC). These surfactants possess a quasi-planar, slightly bent but rigid steroid ring with a hydrophilic face (the hydroxyl groups and the charged carboxylate group) and a hydrophobic face (the methyl groups and the tetracyclic carbon backbone) residing back-to-back.[86] As a result of their unique chemical structure, bile salts act as very effective dispersants of biological molecules in living cells, including fat-soluble vitamins, bilirubin, and cholesterol.[87] Very recently, new dispersants have been synthesized based on the “two-faced” bile salt motif in order to stabilize cylindrically-shaped integral membrane proteins.[88] Furthermore, it is believed that, due to the slightly bent but rigid steroid ring found in bile salts, these surfactants can very effectively accommodate the curvature of the SWCNT surface, and as a result, can better enhance the dispersion stability of SWCNTs in aqueous solutions.[39, 85, 89, 90]

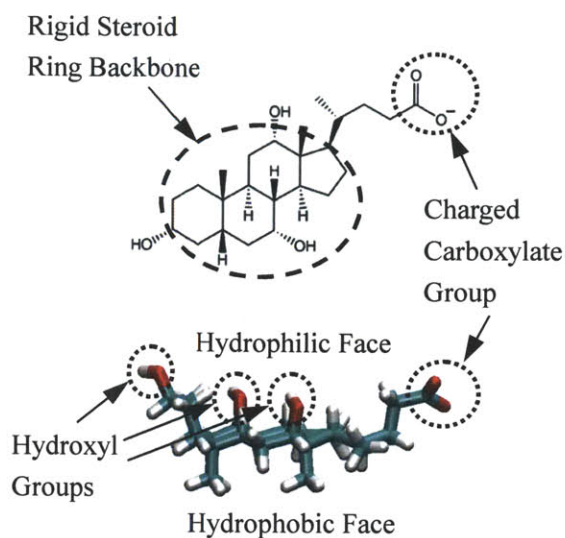


**Figure 2-1:** Schematic (top) and spatial (bottom) chemical structures of sodium cholate, a common bile salt surfactant, showing the rigid steroid-ring backbone, the hydrophobic and hydrophilic faces of the molecule, the hydroxyl groups ( $-OH$ ), and the charged carboxylate group ( $-COO^-$ ). Color code: red – oxygen, light green – carbon, and white – hydrogen.

To date, molecular dynamics (MD) simulations of surfactant adsorption and surface self assembly on SWCNTs have focused primarily on conventional linear surfactants like SDS,[91-93] as well as on single-tailed and double-tailed phosphatidylcholine,[94-96] using all-atomistic or course-grained force fields to model the surfactants and carbon nanotubes. Very recently, interactions between two SDS-coated SWCNTs were studied using MD simulations, including elucidating the contributions from electrostatic and vdW interactions to the simulated potential of mean force (PMF) between the two SWCNTs.[93] In addition, very recently, density differences of SC-SWCNT assemblies when cholate ions adsorb onto SWCNTs having different diameters have been studied using MD simulations.[97, 98] However, the surface morphology of adsorbed SC as a function of its surface coverage have not been investigated computationally. Note that, experimentally, increasing the surfactant concentration beyond the surfactant critical micelle concentration (CMC) results in negligible increases in both surfactant surface coverage at interfaces and in surfactant monomer concentration. This follows because, in general, above the CMC, the added surfactant molecules increase primarily the micelle population.[31, 99] In

addition, in recent MD simulations of surfactant adsorption onto solid surfaces, no desorption of surfactant monomers from the solid surface was observed, which does not ensure thermodynamic equilibrium of the simulated system. Recall that in a thermodynamically-equilibrated aqueous system, where water, surfactants, and SWCNTs are present, surfactant molecules adsorbed onto the SWCNTs should have the same chemical potential as the surfactant monomers desorbed from the SWCNTs. Accordingly, the surfactant monomer concentration should be nonzero to avoid unphysical chemical potential values.[100] Moreover, the mechanism underlying the surfactant-induced stabilization of aqueous dispersions of SWCNTs is not sufficiently well understood to permit a rational design of suitable surfactants.

With all of the above in mind, in the present study, I carried out a large-scale (up to 43,000 atoms), extended-time (up to 240 ns), and all-atomistic MD simulation to investigate the adsorption and surface self assembly of SC, at low and high total SC concentrations, around a SWCNT as a function of the resulting SC surface coverage. A limitation typical to all-atomistic MD simulations is that due to the currently available computational resources, it is impossible to simulate large enough systems to determine the adsorption isotherm of SC on SWCNTs, including the resulting saturated SC surface coverage on the SWCNTs. Note that under saturated SC surface coverage, SC surfactant micelles begin to form. Unfortunately, at dilute aqueous solution conditions where there are so many water molecules in the simulation box to accommodate surfactant monomers and micelles, the simulations become very costly computationally. Therefore, I carried out simulations at a sufficiently high total SC concentration to be able to reproduce the experimentally-estimated saturated SC surface coverage on the SWCNT.[89, 101] Although based on the discussion above I expect that not all the SC monomers will adsorb onto the SWCNT surface, the simulated surface coverage should nevertheless be similar to the experimental value due to the small concentration of desorbed SC monomers (typically, less than the CMC of SC at around 16.3 mM[102]). In the simulations, SC monomers will coexist with adsorbed cholate ions present in the SC-SWCNT assembly, which is required for the system to attain thermodynamic equilibrium. After comparing the simulated

average SC surface coverage and average bulk SC concentration with the experimental values, I confirmed that the simulations at high total SC concentration reproduce reasonably well the experimental saturated SC surface coverage on the SWCNTs.[89] Details about the experimental and simulated values are presented later. More importantly, in order to quantify the interactions between SWCNTs coated with cholate ions, I carried out a potential of mean force (PMF) calculation for two parallel SWCNTs, as a function of intertube separation (defined as the distance between the cylindrical axes of the two SWCNTs),  $d$ , with each SWCNT covered with cholate ions at a surface coverage comparable to the saturated surface coverage deduced from the previous simulation at high total SC concentration. Subsequently, I decomposed the computed PMF profile into contributions resulting from the two parallel bare SWCNTs and from sodium cholate. Moreover, I rationalized the mechanism responsible for the repulsive potential energy barrier and the attractive potential energy well in the PMF profile, resulting from sodium cholate, in terms of the long-range electrostatic repulsion, the short-range vdW attraction, and the short-range steric repulsion.

## 2.2 Methods

### 2.2.1 Simulation Methods

Simulations of sodium cholate adsorption and the associated surface self assembly on the SWCNT surface in aqueous solution were carried out using the GROMACS 4.0 software package.[103] A (6,6) single-walled carbon nanotube (with a diameter of 0.81 nm and a length of 6.16 nm, as determined based on the centers of mass of the carbon atoms) was selected as a representative SWCNT. The simulated SWCNT is sufficiently long compared to the size of a cholate ion (approximately 1.5 nm  $\times$  0.8 nm  $\times$  0.6 nm), which allows observation of the adsorption pattern of the cholate ions on the SWCNT surface. The SWCNT was kept rigid throughout the simulations, with all the carbon atoms in the nanotube treated as uncharged Lennard-Jones (LJ) spheres using the LJ parameters reported by Tummala et al.[91, 92, 104] Water molecules were modeled using the standard SPC/E model,[105] with bond lengths

constrained using the SETTLE algorithm.[106] SC molecules, which were assumed to completely dissociate into cholate ions and sodium counterions in water, were modeled using the OPLS-AA force field.[107] Bond lengths in the cholate ion were constrained using the parallel version of the LINCS algorithm.[108, 109] van der Waals (vdW) attractions and hard-core steric repulsions were treated with a cutoff distance of 0.9 nm, which falls within the typical range of cutoff values used in other publications.[91, 93] The vdW attractions and the hard-core steric repulsions between different atoms were calculated from the LJ potential using the standard geometric averaging rule which is implemented in the OPLS-AA force field.[107] Long-range electrostatic interactions were treated using the particle mesh Ewald (PME) summation method.[110, 111]

The equations of motion were integrated with a time step of 2 fs using the Verlet (Leap-Frog) algorithm.[112, 113] All the simulations were conducted under the NPT ensemble (constant number of atoms, constant pressure of 1.0 bar, and constant temperature of 298.15 K) in order to best mimic the experimental conditions. The velocity-rescaled Berendsen thermostat was implemented to maintain a constant temperature in the simulated system.[114] The pressure was coupled to an isotropic Berendsen barostat.[115] Periodic boundary conditions were applied in all three directions. In practice, most of the synthesized SWCNTs are uncapped (to a larger extent when they undergo ultrasonication),[85] and therefore, in order to allow small molecules such as water and sodium counterions to fill the nanotube, the length of the simulation box was chosen to be about 0.9 nm longer than the nanotube length (recall that the diameter of a water molecule is around 0.35 nm using the OPLS-AA force field). The trajectories, velocities, and forces corresponding to all the atoms in the system were saved every 10,000 steps (20 ps) to satisfy the ergodicity criterion for data analysis.[74]

### **2.2.2 Simulated Systems**

To probe the adsorption and self assembly of SC on the SWCNT surface, a single (6,6) SWCNT was confined at the center of the simulation box, with its cylindrical axis oriented along the

z-direction. In order to quantify the effect of surfactant concentration on the adsorption morphology, I positioned different numbers of cholate ions (15 and 25) around the nanotube. Note that having 25 cholate ions on the 6.16 nm long (6,6) SWCNT in my simulation matches the experimentally-reported saturated SC surface coverage on a SWCNT.[89] Different numbers of added cholate ions correspond to different total concentrations of cholate ions, with 15 added cholate ions corresponding to a low concentration of 75 mM and 25 added cholate ions corresponding to a high concentration of 125 mM. Subsequently, the simulation box was filled with water molecules. In order to maintain electroneutrality, an appropriate number of water molecules were replaced by sodium counterions resulting from the added cholate ions. Each system was equilibrated for 240 ns, and only the last 20 ns of simulation were used for data analysis. The simulation was confirmed to have reached equilibrium by monitoring the SASAs (solvent accessible surface areas) of the cholate ions and the nanotube as a function of time (see Figure 2-A1 in the Appendix). SASA was traced out by a probe sphere of radius 0.2 nm (corresponding to the location of the first hydration shell),[116] which was rolled around the cholate ions or the nanotube to identify their solvent (water in this case) accessible regions.[117] Note that the region on the nanotube covered by cholate ions is not taken into account in the SASA calculation because water molecules in this region are excluded by the adsorbed cholate ions. As a result, I believe that the simulated SASA can nicely quantify the dynamics of adsorption and desorption of SC on the SWCNT surface, similar to what takes place when surfactants self assemble to form micelles.[118] The simulated system size, including the total numbers of SC and water molecules, the total number of atoms, the size of the simulation box, and the total simulation time, are summarized in Table 2-A1 in the Appendix.

To investigate the interactions between two parallel SC-coated (6,6) SWCNTs, I calculated the potential of mean force (PMF) by numerically integrating, in a trapezoidal manner, the forces exerted to separate the two nanotubes at various intertube separations.[93, 119] This integration process begins from the largest intertube separation of 3.48 nm (where the simulated force applied to separate the two nanotubes approaches zero) and proceeds to the smallest intertube



separation of 1.08 nm (where the force applied resulting from the hard-core steric repulsion between the two nanotubes overshoots). The force exerted at the center of mass of each SWCNT should include contributions from all the flexible molecules in the system, including the adsorbed cholate ions, the sodium counterions, and the water molecules. Note that the initial configuration of the SC-SWCNT assembly was obtained from the final configuration of the previous SC adsorption and self-assembly simulations corresponding to a SC surface coverage close to saturation (resulting from the 125 mM total SC concentration). In addition, note that in order to compare my results for SC with those for SDS where no SDS monomers were present,[93] the monomeric SC were removed to generate the initial configuration for the PMF calculation, assuming that their contribution to the PMF results are small. In order to carry out the PMF calculation for SC, I constructed a series of initial configurations in a manner similar to that in the work by Xu et al. for SDS.[93] The first configuration was generated by placing two parallel SC-SWCNT assemblies at an intertube separation of 3.48 nm, and then filling the simulation box with sufficient water molecules and an appropriate number of sodium counterions to maintain electroneutrality. Following that, the system was further equilibrated for 20 ps under the NPT ensemble. The subsequent initial configurations were constructed from the preceding final equilibrium configuration as follows: for a pair of parallel SC-SWCNT assemblies, only the two parallel bare SWCNTs were translated as rigid entities towards each other in increments of 0.04 nm, and subsequently, the system was equilibrated for 20 ps. Note that translating only the bare SWCNTs allowed the cholate ions to reorganize on the SWCNT surfaces to avoid collisions when the two SWCNTs are very close to each other. More specifically, the PMF profile was constructed by carrying out a total of 61 MD simulations with the intertube separation decreasing from 3.48 nm to 1.08 nm. After obtaining all the initial configurations, each system was equilibrated for 20 ns under the NPT ensemble. For the simulated systems at various intertube separations, only the last 5 ns, corresponding to the equilibrated systems, were used for data analysis, including the PMF calculations. The equilibration of each simulation run was verified by the convergence of the cumulative average force (averaged from time zero to time  $t$ ) as a

function of time  $t$ , as shown in Figure 2-A2 in the Appendix. The errors in the simulated PMF profile were estimated based on the errors of the simulated forces using the block-averaging method, while accounting for the integration process.[120] In addition, in order to decompose the contributions to the total PMF profile resulting from the two parallel bare SWCNTs to obtain the net contributions of SC,  $\Delta$ PMF, to the total PMF profile (the contribution of water is negligible, as will be discussed later), the forces required to confine two parallel bare SWCNTs at different intertube separations in vacuum were calculated in a similar manner using MD simulations, and the resulting PMF profile was calculated by integrating the forces.

## **2.3 Results and Discussion**

### **2.3.1 Sodium Cholate Adsorption and Surface Self Assembly on a SWCNT**

Representative post-equilibrium simulation snapshots of a (6,6) SWCNT in aqueous SC solutions at total concentrations (that is, the total number of SC molecules divided by the volume of the simulation box) of 75 mM and 125 mM are shown in Figure 2-2. A common feature shared by both snapshots is that the cholate ions wrap around the SWCNT like a ring with the hydrophobic faces pointing inwards and the hydrophilic faces (having oxygen atoms shown as red spheres in Figure 2-2) pointing outwards, as has been speculated in several recent experimental studies.[39, 85, 89, 101] Note that the precise orientations of the cholate ions with respect to the cylindrical axis of the SWCNT will be discussed later. Having the hydrophobic face pointing inwards tends to maximize the contact between the hydrophobic faces of the cholate ions and the surface of the SWCNT, as driven by the hydrophobic effect.[30] This organization of the cholate ions on the SWCNT surface can be seen more clearly by comparing the radial distribution function (RDF) of the entire cholate ions (Figure 2-3-a) relative to the RDF of the charged carboxylate groups (Figure 2-3-b): the charged carboxylate groups (with the largest peak at around 1.2 nm at both 75 mM and 125 mM) are positioned farther away from the cylindrical axis of the SWCNT than the entire cholate ions (with the largest peak at around 0.8 nm at both 75 mM and 125 mM).

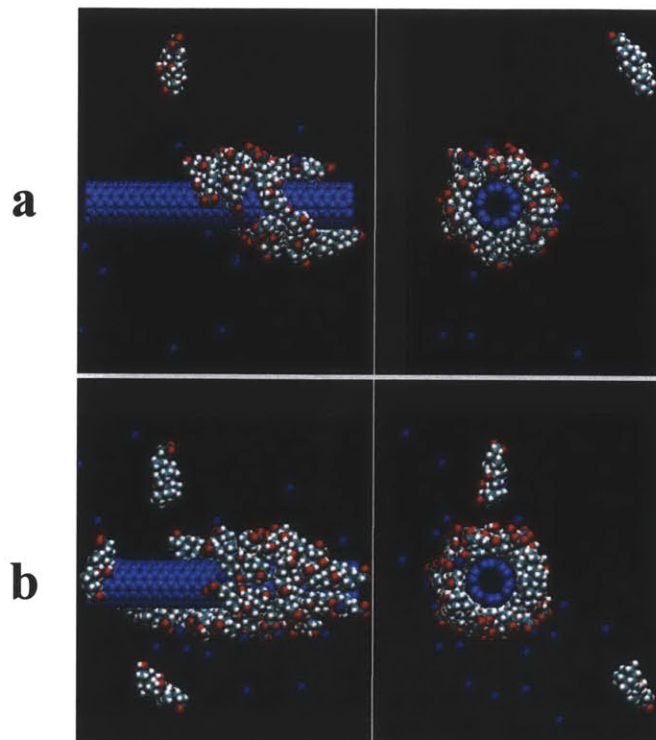


**Figure 2-2:** Representative post-equilibrium simulation snapshots of a (6,6) SWCNT in aqueous SC solutions at two different total SC concentrations: (a) 75 mM and (b) 125 mM. The two plots on the left are side views and the two plots on the right are corresponding front views. Water molecules are not shown for clarity. Color code: red – oxygen, blue – sodium counterion, light green – carbon, white – hydrogen, and purple – carbon atoms in the SWCNT.

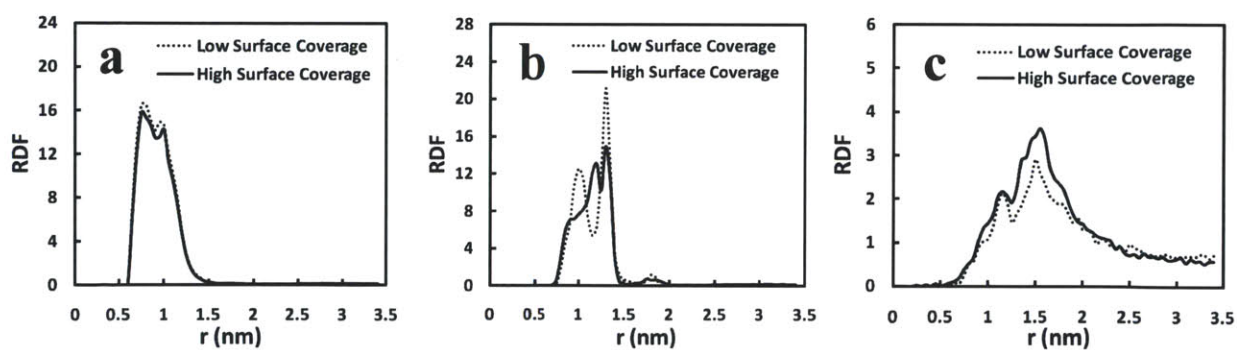


**Figure 2-3:** Simulated radial distribution functions (RDFs) relative to the cylindrical axis of a SWCNT (“ $r$ ” is measured radially from this axis): (a) RDF of the cholate ions, (b) RDF of the carbon atoms of the charged carboxylate groups, and (c) RDF of the sodium counterions. The RDFs are plotted for low (corresponding to a total SC concentration of 75 mM) and high (corresponding to a total SC concentration of 125 mM) SC surface coverages. Note that the radius of the (6,6) SWCNT considered here is around 0.55 nm when excluded-volume effects are accounted for, and explains why the three RDF profiles shown remain zero for  $r \leq 0.55$  nm.

Another interesting feature that can be seen in Figure 2-2 is that the adsorbed cholate ions prefer to distribute in a very compact manner around the SWCNT, independent of their surface coverage on the SWCNT surface. This is reflected in the RDF profiles in Figure 2-3-a, where the shape of the RDF curves corresponding to the cholate ions is nearly independent of the total SC concentration. The RDF profiles in Figure 2-3-a further indicate that this compact layer of cholate ions is located within 1.5 nm around the SWCNT (since the two RDF curves decay to almost zero beyond 1.5 nm), and have a thickness of around 0.9 nm (as reflected in the width of the RDF curve in Figure 2-3-a). This finding for SC is very different than for SDS, where the RDF becomes wider (the SDS molecules organize perpendicular to the SWCNT surface) as the SDS surface coverage increases.[91, 93] This unique surface adsorption morphology of SC, compared to those of more conventional surfactants possessing flexible linear tails,[91-96] results from the rigid, steroid-ring structure of SC (see Figure 2-1).

Another common feature shared by the two side-view simulation snapshots in Figure 2-2 is that, instead of distributing uniformly around the nanotube,[85, 89] the adsorbed cholate ions prefer to self assemble side-by-side (see Figure 2-A3-a for zoomed-in snapshots), due to the hydrophobic effect.[30] Note that this side-by-side SC organization tends to minimize contact between the hydrophobic faces of the cholate ions and water, similar to what has been reported in the case of SDS adsorption onto SWCNTs.[91] This side-by-side SC self-assembly is also facilitated by the condensation (or binding) of positively-charged sodium counterions onto single, or multiple, negatively-charged cholate ions (typically, onto the charged carboxylate groups, as shown in Figures 2-S3-b and 2-S3-c). Similar to what has been reported in the case of SDS adsorption onto SWCNTs,[91, 104] this sodium counterion condensation shields the electrostatic repulsions between the charged carboxylate groups and effectively brings them closer to each other. This interesting feature can also be seen in Figure 2-3-c, where the largest peak of the RDF of the sodium counterions around the SWCNT (at around 1.5 nm) is closely located to the largest peak of the charged carboxylate groups (at around 1.2 nm, see Figure 2-3-b), reflecting the strong electrostatic attractions between these oppositely-charged groups. The difference in the positions

of these two peaks, 0.3 nm, reflects the center-to-center distance between a sodium counterion and a charged carboxylate group at contact.

As shown in Figure 2-2, as the total SC concentration increases from 75 mM in (a) to 125 mM in (b), one can clearly observe that both the number of cholate ions adsorbed on the SWCNT surface and the number of cholate ions in the aqueous phase away from the SWCNT increase. In particular, the monomeric SC concentration (that is, the number of SC monomers divided by the size of the simulation box) in Figure 2-2-b is doubled compared to that in Figure 2-2-a. In order to relate the SC surface coverage to the monomeric SC concentration, I carried out a population analysis at different total SC concentrations. Based on this population analysis, I found that different total SC concentrations yield different SC surface coverages and related monomeric SC concentrations. The time-averaged number of cholate ions adsorbed on the SWCNT surface was computed by integrating the number density profiles (RDF times the average number density) of the cholate ions around the SWCNT up to a cutoff distance of 1.5 nm, within which the cholate ions are considered to be adsorbed on the nanotube, and beyond which the cholate ions are considered as monomers. The computed average numbers of adsorbed cholate ions at 75 mM and 125 mM are consistent with the results based on a visual analysis of the post-equilibrium simulation snapshots shown in Figure 2-2. Subsequently, the SC surface coverage was computed based on the diameter of 0.81 nm for the 6.16 nm long (6,6) SWCNT that I simulated. In addition, estimating the average monomeric SC concentrations at different total SC concentrations is quite straightforward. Specifically, the average number of SC monomers is equal to the difference between the total number of SC molecules present in the simulation box and the average number of SC molecules adsorbed on the nanotube. Detailed results of the population analysis discussed above are reported in Table 2-1, where I have also reported experimental values of the saturated SC surface coverage on SWCNTs[89] and of the CMC of SC[102] (a very good indicator of the monomeric SC concentration), in order to compare the population analysis results at 75 mM and 125 mM with experiment.

**Table 2-1: Population Analysis Results and Relevant Experimental Data**

System	Average Number of Adsorbed Cholates Ions	Average Number of Monomeric Cholates Ions	Average SC Surface Coverage (molecules/nm <sup>2</sup> )	Linear Packing Density of SC (molecules/nm)	Average Monomeric Concentration of SC (mM)
1 <sup>a</sup>	13.87	1.13	0.89	2.25	5.6
2 <sup>b</sup>	21.84	3.16	1.39 (1.53 ± 0.34) <sup>c</sup>	3.55 (3.60 ± 0.80) <sup>c</sup>	15.6 (16.3) <sup>d</sup>

<sup>a</sup> Sodium cholate adsorption and surface self-assembly simulations on single (6,6) SWCNTs under the low total SC concentration of 75 mM.

<sup>b</sup> Sodium cholate adsorption and surface self-assembly simulations on single (6,6) SWCNTs under the high total SC concentration of 125 mM.

<sup>c</sup> The numbers in parentheses are the experimental values for the saturated surface coverage of cholates ions around a (6,5) SWCNT from Ref. [89].

<sup>d</sup> The number in parenthesis is the experimental CMC of sodium cholate from Ref. [102].

As shown in Figure 2-2-a, at the low total SC concentration of 75 mM, the majority of the cholates ions adsorb onto the SWCNT surface, which results in an average SC surface coverage of 0.89 molecule/nm<sup>2</sup> and an average monomeric SC concentration of 5.6 mM (see Table 2-1). As shown in Figure 2-2-b, at the high total SC concentration of 125 mM, more cholates ions adsorb onto the SWCNT surface, which results in an average surface coverage of 1.39 molecule/nm<sup>2</sup> and an average monomeric SC concentration of 15.6 mM (see Table 2-1). As expected, since I chose the high total SC concentration of 125 mM to reproduce the experimental saturated SC surface coverage, the simulated surface coverage at 125 mM (1.39 molecule/nm<sup>2</sup>) agrees well with the experimental value of 1.53 ± 0.34 molecules/nm<sup>2</sup> estimated for a (6,5) SWCNT (see Table 2-1).[89] It is interesting to recognize that, based on the simulations under the saturated SC surface coverage, cholates ions can only partially cover the SWCNT surface, consistent with the experimentally estimated ratio of around 70%.[89] This should be contrasted with the SDS case, where dodecyl sulfate ions can completely cover the SWCNT surface based on both experimental and simulation observations.[76, 91, 93] Note that the saturated SC surface

coverage was estimated based on the linear packing density of  $3.6 \pm 0.8$  cholate ions adsorbed per unit length (in nm) on (6,5) SWCNTs (with a diameter of 0.75 nm, as calculated based on the centers of mass of the carbon atoms), which was estimated based on the density of SC-SWCNT assemblies measured using an analytical ultracentrifuge in a 46 mM SC solution.[89] For my estimation, I have assumed that the linear packing density of SC on the experimentally-studied (6,5) SWCNTs is the same as that on the (6,6) SWCNTs considered here due to the similar diameters of these two SWCNTs. Although the total SC concentration studied in Ref. [89] (46 mM) is higher than the CMC of SC (16.3 mM),[102] in view of my previous discussion, the saturated SC surface coverage should be independent of the experimental total SC concentration beyond the CMC of SC. In addition, note that the estimated monomeric SC concentration of 15.6 mM at the simulated total SC concentration of 125 mM is similar to the experimental CMC of SC (16.3 mM[102]), confirming that the SC surface coverage on the SWCNTs that I obtained at 125 mM reproduced reasonably well the experimental saturated SC surface coverage. Note that, due to the limited simulation box size, if the total SC concentration in the simulation box is further increased, the SC surface coverage on the SWCNTs would continue to increase beyond the experimental saturated SC surface coverage (more cholate ions would adsorb onto the SWCNTs instead of contributing to an increase in the micelle population).[31, 91, 93-96] As a result, it is inappropriate to simulate even higher total SC concentrations. However, in future studies, coarse-grained models may be implemented based on my simulation results (e.g., the RDF profiles of the cholate ions, the charged carboxylate groups, and the sodium counterions around the SWCNT) to more accurately calculate the adsorption isotherm of SC on SWCNTs.

As discussed earlier, the cholate ions prefer to wrap around the SWCNT like a ring. However, the precise orientations of the cholate ions with respect to the cylindrical axis of the SWCNT still need to be determined. For this purpose, I calculated the distribution of the angles between the principal axis of the cholate ions (defined in Figure 2-4) and the cylindrical axis of the SWCNT. As shown in Figure 2-4, for both SC surface coverages, the cholate ions prefer to orient almost parallel to the cylindrical axis of the SWCNT (the largest peaks in the angle distribution profile

are close to  $0^\circ$  and  $180^\circ$ ), consistent with observations in recent MD simulations of SDS-coated SWCNTs.[91, 93] In addition, Figure 2-4 shows that the cholate ions also have a small tendency to orient perpendicular to the cylindrical axis of the SWCNT (the angle distribution profile also exhibits a smaller peak at around  $90^\circ$ ) to accommodate their own slightly bent planar chemical structures with respect to the curved SWCNT surface, an interesting finding that is consistent with recent speculative experimental reports.[89, 101] Note that the perpendicular orientation of the cholate ions can be clearly seen in Figure 2-A3-a. This multi-peak feature in the angle distribution profile may reflect the fact that adsorbed cholate ions need to adapt both configurations to accommodate the SWCNT circumference. This is indeed driven by the need to form a closed ring consisting of a discrete number of cholate ions in order to wrap around the SWCNT. This last finding suggests that the orientation of the cholate ions relative to the cylindrical axis of the SWCNT may vary as a function of the nanotube diameter, due to the rigidity of the cholate ions, a unique feature which has not been observed with other conventional surfactants possessing flexible linear hydrocarbon chains.[91, 93] In the future, it will be interesting to carry out MD simulations as a function of nanotube diameter to further corroborate this suggestion.



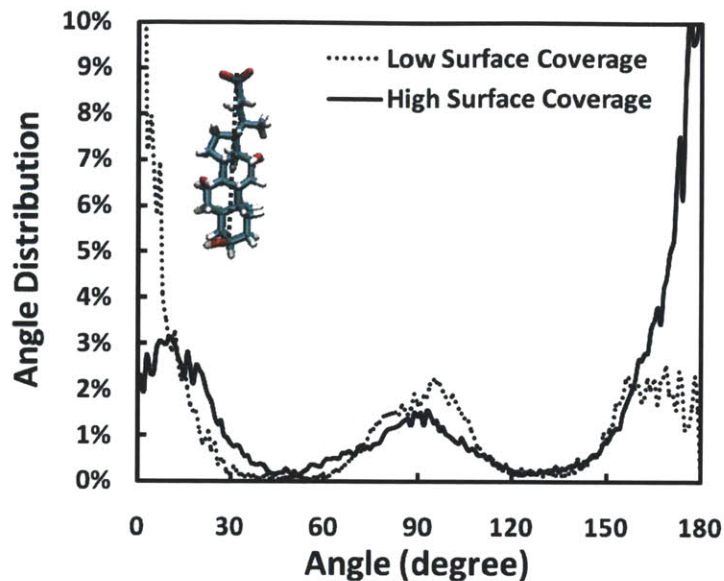


**Figure 2-4:** Simulated distribution profiles of the angle,  $\theta$ , between the principal axis of the cholate ions and the cylindrical axis of the SWCNT. Note that bias resulting from variations in solid angle has been removed by a weighting factor of  $(1/\sin \theta)$ . In the SC molecular structure shown, the dotted line connecting the carbon atom in the carboxylate group with the carbon atom at the end of the steroid ring defines the principal axis of the cholate ion (refer also to Figure 2-1).

### 2.3.2 Interactions between Two Parallel SWCNTs with Adsorbed Cholate Ions

The interactions between two parallel SWCNTs with cholate ions adsorbed at approximately the saturated SC surface coverage were quantified using the potential of mean force (PMF) per unit length (in nm) of the nanotube, as a function of the intertube separation,  $d$ , as shown by the solid line in Figure 2-5-a. The simulated PMF profile exhibits a primary, long-range repulsive potential energy barrier possessing a maximum of around 28 kJ per mole per nanometer of the simulated SWCNTs, extending from 2.0 nm to 3.48 nm (reflected by the fact that the slope of the PMF curve here is negative). This primary potential energy barrier prevents the SWCNTs from approaching each other under the vdW attractions between the two SWCNTs, and as a result, prevents coagulation of the SWCNT aqueous dispersion. The PMF profile in Figure 2-5-a also exhibits a secondary, attractive potential energy region extending from 1.7 to 2.0 nm (reflected by the fact that the slope of the PMF curve here is positive). The depth of this attractive energy

well is around  $-23$  kJ/mol/nm, which counter-balances most of the repulsive energy barrier, and as a result, the PMF profile approaches a small minimum of 5 kJ/mol/nm at around 1.7 nm. As the intertube separation decreases further from 1.7 to 1.5 nm, the PMF profile goes up again, giving rise to a small repulsive energy barrier of around 10 kJ/mol/nm.

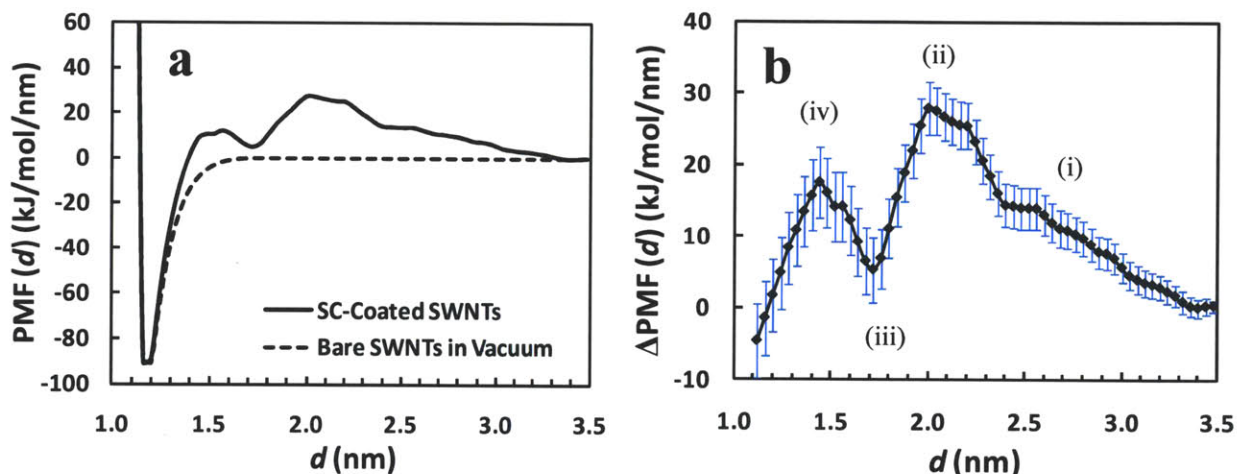


**Figure 2-5:** (a) Simulated potential of mean force (PMF) corresponding to: (i) two parallel SWCNTs coated with cholate ions (solid line), and (ii) two parallel bare SWCNTs in vacuum (dashed line), as a function of the intertube separation,  $d$ . Note that the two PMF profiles overlap for  $d \leq 1.2$  nm, (b) Net contribution of SC to the PMF profile,  $\Delta$ PMF, corresponding to two parallel SWCNTs coated with cholate ions. The error bars (in blue) were computed using the block averaging method discussed in the text. Note that the y-axis in (b) has been rescaled relative to that in (a) for clarity. In addition, the designations (i) to (iv) in (b) correspond to plots (a) to (d) in Figure 2-7, where 2D atom number density plots of the cholate ions and the sodium counterions are shown at selected intertube separations in order to help explain the features exhibited by the  $\Delta$ PMF profile discussed in the text.

Although in their recent simulations of SDS adsorption onto SWCNTs, Xu et al. did not study the PMF profile of two parallel SDS-coated SWCNTs at intertube separations smaller than 1.5 nm,[93] I extended my simulations to include this separation region in the case of sodium cholate. As the intertube separation decreases from 1.5 to 1.2 nm, the PMF profile drops down sharply (the primary attractive energy region) and reaches its minimum energy well of around  $-90$  kJ/mol/nm, as determined by the strong vdW attraction between the two parallel bare SWCNTs (see the dashed line in Figure 2-5-a). This reflects the fact that the separated SWCNTs will

eventually rebundle as a result of this minimum energy well, and therefore, surfactants can only stabilize SWCNTs in aqueous solutions temporarily through the induced repulsive energy barrier. Finally, as the intertube separation decreases further below 1.2 nm, the PMF profile goes up sharply, as determined by the hard-core steric repulsion between the two parallel bare SWCNTs (note that the solid line and the dashed line overlap in this region, as shown in Figure 2-5-a).

All the features of the PMF profile discussed above for sodium cholate agree well qualitatively with recent computational studies of grafted polymers,[121] the adsorbed cationic surfactant, n-decyltrimethylammonium chloride (DTMAC),[122] and the adsorbed anionic surfactant, SDS,[93, 119] on SWCNTs using mean-field theory,[121] statistical mechanics,[122] and MD simulations,[93, 119] respectively. Comparing my PMF results for SC with those of Xu et al. for SDS,[93] I have found, quantitatively, that SC is more effective than SDS at stabilizing aqueous dispersions of individual SWCNTs, when the SWCNTs are covered with the saturated amounts of each surfactant type. Specifically, (i) the simulated potential energy barrier induced by SC at 2.0 nm is 40% higher than that induced by SDS at 2.4 nm,[93] and (ii) the simulated attractive energy well induced by SC at 1.7 nm (see Figure 2-5-a) is 50% smaller than that induced by SDS at the same intertube separation.[93] Note that a shallower attractive energy well can still enhance the dispersion stability based on the theory of slow colloid coagulation,[123] where the integration of the exponential of the PMF between two colloidal particles (two SC-coated SWCNTs in the present case) along the inter-particle distance is inversely proportional to the coagulation rate of these two colloidal particles.

To further understand the mechanism responsible for the superior dispersion stability induced by SC, it is instructive to decouple the contribution resulting from the two parallel bare SWCNTs (including the vdW attraction and the hard-core steric repulsion) to the total PMF profile. To this end, I subtracted the PMF profiles corresponding to the solid line (with SC) and the dashed line (without SC) in Figure 2-5-a. The resulting net SC contribution,  $\Delta\text{PMF}$ , to the total PMF profile is shown in Figure 2-5-b, where I have assumed that the contribution due to the water molecules is negligible compared to that due to SC based on the recent studies by Xu et al in the case of

SDS.[93] This approximation may also be rationalized by the fact that the magnitude of the simulated PMF induced by water molecules is quite small when two SWCNTs are present in pure water.[124] Note that, in general, water molecules only contribute to the repulsive energy barrier in the simulated PMF profile at small intertube separations ( $d < 2.0$  nm considered here), when they are confined by the surfactant-coated SWCNTs.[124] As a result, in the case of SC, this confinement-induced water repulsion is expected to slightly reduce the net contribution of SC to the simulated PMF profile at small intertube separations, while this water-induced repulsive contribution should be negligible at large intertube separations. The net contribution of SC to the PMF profile (the solid line in Figure 2-5-b) exhibits features which are similar to those exhibited by the total PMF profile (the solid line in Figure 2-5-a). This is due to the fact that the interaction between the two parallel bare SWCNTs is negligible until the intertube separation decreases below 1.7 nm (see the dashed line in Figure 2-5-a).

At intertube separations greater than 2.0 nm (see Figure 2-5-b), the onset of the repulsive potential energy barrier in the  $\Delta$ PMF profile is dominated by the long-range electrostatic repulsion between the two parallel SC-coated SWCNTs, which behave as two parallel, negatively-charged cylinders, mediated by the positively-charged sodium counterions. This contribution to the potential energy barrier has been widely recognized as reflecting the electrostatic contribution which appears in the continuum DLVO (Derjaguin-Landau-Verwey-Overbeek) theory.[43, 99, 125, 126] Based on the Poisson-Boltzmann equation,[127] the electrostatic portion of the DLVO potential between two SC-coated SWCNTs considered here is approximately proportional to the effective surface charge density on the SWCNT surface,  $\sigma$ . Although the saturated surface coverage of SDS used in the recent MD simulations by Xu et al.,[93] as well as observed experimentally (2.8 molecules/nm<sup>2</sup>),[128] is twice that of SC used in my MD simulations (1.4 molecule/nm<sup>2</sup>),[89] after accounting for the effect of sodium counterion binding, the difference between the effective surface charge densities in the SC and the SDS cases should be greatly reduced. This expectation is consistent with the fact that the extent of sodium counterion dissociation for a SDS aggregate (= 0.124) is much smaller than that for a SC

aggregate (= 1.000).[129] The simulated number of sodium counterions bound to the charged carboxylate groups in cholate ions (under high total SC concentration) is consistent with the experimental observation of a high degree of sodium counterion dissociation associated with a SC aggregate (see Figure 2-A4 in the Appendix for more details).

In addition to the repulsive electrostatic interaction described by the DLVO theory, other repulsive interactions operate between two SC-coated SWCNTs.[99] In particular, the ion-induced steric repulsion[99, 130, 131] has been reported recently to play a role in repelling two SDS-coated SWCNTs in the simulation study by Xu et al.[93] In fact, the existence of a concentrated ion wall can be seen in the simulated contour plot of the density profile of the sodium counterions along the x-axis of the simulation box (which is parallel to  $d$ ), as a function of the intertube separation,  $d$ , as shown in Figure 2-6. The ion wall is defined here as a layer of sodium counterions with a concentration of around  $15 \text{ kg/m}^3$ , which is two times greater than their bulk concentration of around  $5 \text{ kg/m}^3$ , following the same definition by Xu et al.[93] The ion wall is present at  $d$  values ranging from 1.7 to 2.8 nm (denoted by the red color in Figure 2-6). The existence of this ion wall can also be seen in the 2D atom number density plots (averaged along the cylindrical axis of the SWCNT) of the sodium counterions at two intertube separations, as shown in Figures 2-7-a and 2-7-b. The fact that the ion wall in the case of SC spans a wider range of intertube separations (1.1 nm) than that in the case of SDS (0.9 nm)[93] may explain the higher potential energy barrier induced by SC. Indeed, if the ion-induced steric repulsive force in the SC case operates over a wider range of intertube separations, then, the potential energy barrier obtained by integrating the repulsive forces over this wider range of separations will be higher.

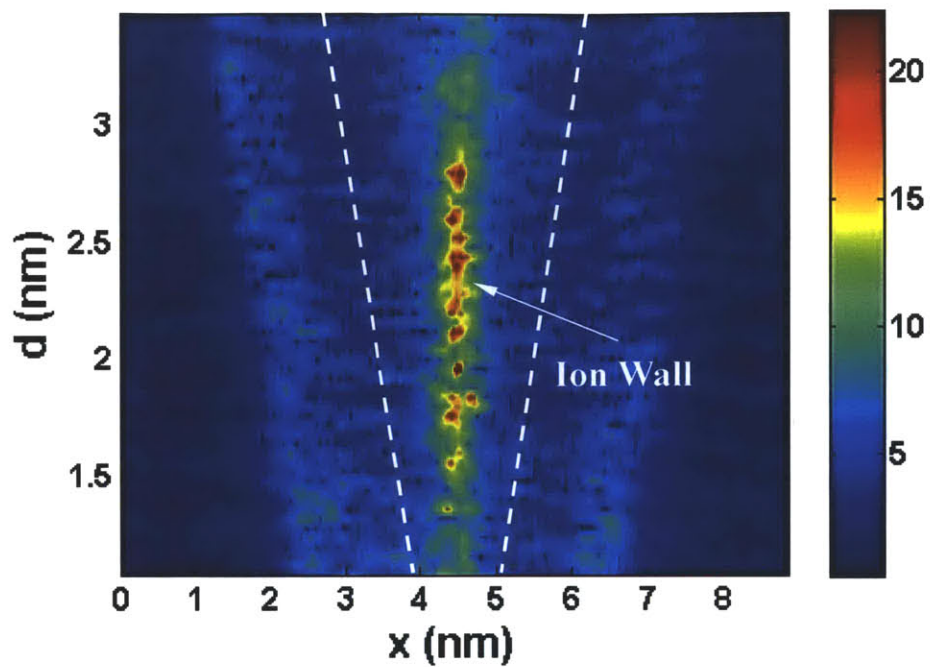


**Figure 2-6:** Simulated contour plot of the density profile of the sodium counterions (in units of  $\text{kg/m}^3$ ) along the x-axis of the simulation box (which is parallel to  $d$ ), as a function of the intertube separation,  $d$ . The density scale is shown in the side color bar. As shown, the ion wall extends from an intertube separation of  $d = 1.7$  to  $d = 2.8$  nm. The locations of the two SWCNT cylindrical axes along the x-axis are shown by the two white dashed lines.



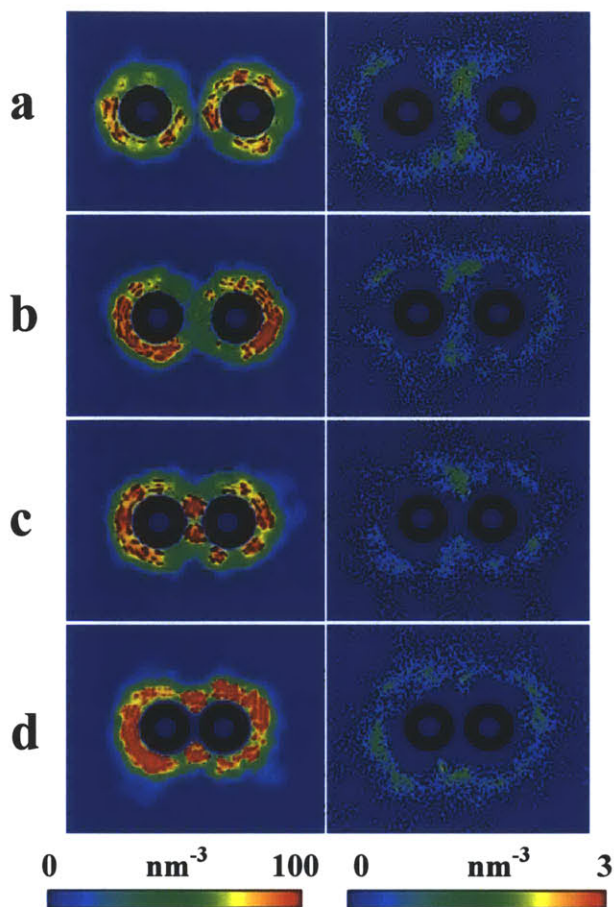


**Figure 2-7:** 2D atom number density plots of the cholate ions (left panel) and the sodium counterions (right panel) at selected intertube separations of: (a) 2.48 nm, (b) 2.00 nm, (c) 1.68 nm, and (d) 1.32 nm. These four intertube separations were selected in order to help explain the features exhibited by the PMF profile discussed in the text. The atom number density scale is shown in the bottom color bars. The density plots in (a) – (d) represent front views of the simulation box. The black rings denote the locations of the two parallel SWCNTs.

At shorter intertube separations below 2.0 nm (see Figure 2-5-b), the cholate ions on the two SWCNT surfaces begin to contact each other (the two green rings overlap in Figure 2-7-b), which triggers direct interactions between them. These interactions between the cholate ions on the two SWCNT surfaces results in the oscillatory behavior of the  $\Delta$ PMF profile (for  $d$  values ranging from 1.08 nm to 2.0 nm in Figure 2-5-b), which has been widely recognized to result from the interplay between the short-range vdW attraction and the short-range hard-core steric repulsion between molecules (the cholate ions in the present case) in close contact.[132] Note that once the two layers of cholate ions interleave with each other to merge into a single layer,

the electrostatic force acting along the x-axis responsible for repelling the two parallel SWCNTs will no longer exist. This oscillatory behavior, reflecting the molecularity of all condensed phases in nature, has been extensively studied experimentally in the case of liquids confined to molecular separations by two approaching smooth mica surfaces.[133-135] As expected, the continuum DLVO theory breaks down at molecular separations, and fails to reproduce the oscillatory  $\Delta$ PMF profile computed using MD simulations.

The interactions between cholate ions are shown in the 2D atom number density plots of the cholate ions at selected intertube separations to help explain the features exhibited by the  $\Delta$ PMF profile (see Figure 2-7). Note that although the cholate ions on the SWCNT surfaces begin to contact each other at a larger intertube separation of 2.48 nm (the two green rings begin to overlap in Figure 2-7-a), the partially-covered SWCNT surface allows the cholate ions to exchange between the two nanotubes to efficiently cover the empty surface without incurring steric penalties (no red color within the intertube gap in Figure 2-7-b). As expected, if the density of the cholate ions within the intertube gap is large (denoted by the red color in Figure 2-7-c), then, the cholate ions are confined, and do exert a strong steric repulsive force between the two SWCNTs. On the other hand, if the density of cholate ions within the intertube gap is small (denoted by the green color in Figures 2-7-a and 2-7-b), then, the cholate ions have vacancies around them that can be filled, and do exert a strong vdW attractive force between the two SWCNTs. Therefore, the simulated oscillatory  $\Delta$ PMF profile as the intertube separation decreases can be rationalized as follows: (i) the intertube gap begins to accommodate only a single layer of cholate ions from  $d = 2.0$  to 1.7 nm (see Figure 2-7-b), (ii) the two SWCNTs begin to compress the single layer of cholate ions from  $d = 1.7$  to 1.5 nm (see Figure 2-7-c), and (iii) the single layer of cholate ions is squeezed out of the intertube gap, leaving a vacancy from  $d = 1.5$  to 1.08 nm (see Figure 2-7-d). Note that this relationship between the density of the cholate ions and the direction of the exerted force is analogous to the relationship between the density of cholate ions and the osmotic pressure within the intertube gap.[99] Note also that the mechanism underlying the vdW attraction between rigid molecules is slightly different from the



bridging attraction between flexible polymers grafted onto colloidal particles,[99] contrary to the recent discussion in Ref. [93]. Interestingly, when there is a single layer of sparsely-packed cholate ions located within the intertube gap from  $d = 1.7$  to  $2.0$  nm, the cholate ions are able to rotate (see Figure 2-A5 in the Appendix) in order to fill the vacancy within this fixed intertube gap, due to their bean-like chemical structure. This unique feature of SC was not observed in the case of SDS, because of the linear, rod-like shape of the SDS molecule. As a result, the attractive energy well at  $d = 1.7$  nm induced by sodium cholate is not as deep as that induced by SDS.

## 2.4 Conclusions

In summary, I reported the first detailed large-scale all-atomistic MD simulation study of the adsorption and surface self assembly of the bile salt surfactant, sodium cholate, on a (6,6) SWCNT in aqueous solution. My results on: (i) the radial distribution function of the cholate ions around the cylindrical axis of the SWCNT, and (ii) the distribution of the principal angles of the cholate ions with respect to the cylindrical axis of the SWCNT allow verification of previous speculations, featuring the “two-faced”, slightly-bent, rigid steroid-ring structure of bile salts. In addition, I studied the relation between the surface coverage of the cholate ions on the SWCNT surface and the monomeric SC concentration by considering low and high total SC concentrations. I selected a high total SC concentration to carry out the simulations, so that the simulated surface coverage of the cholate ions would match the experimental SC saturated surface coverage. Subsequently, I utilized the final configuration of a single SC-coated SWCNT, under this saturated surface coverage, to carry out a series of simulations to compute the PMF between two parallel SC-coated SWCNTs as a function of intertube separation. The net contribution of sodium cholate to the PMF profile,  $\Delta\text{PMF}$ , may be explained reasonably well by: (i) the long-range electrostatic repulsion between the two SC-coated SWCNTs (as described in the continuum DLVO theory) at large intertube separation, (ii) the short-range ion-induced steric repulsion at large intertube separation, and (iii) the short-range vdW attraction and steric repulsion (oscillatory force) induced by the adsorbed cholate ions at small intertube separation.

By comparing my simulated PMF profile of SC with the PMF profile of SDS when the SWCNTs are coated with the saturated surface coverages corresponding to each surfactant type, I am able to show that SC is a better stabilizer than SDS (it has a higher repulsive energy barrier and a shallower attractive energy well), a finding that is consistent with the wide-spread use of SC to disperse SWCNTs in aqueous solution. In particular, the shallower attractive energy well induced by SC compared to that induced by SDS is due to the rigid, bean-like chemical structure of SC which allows this bile salt surfactant to more effectively accommodate the intertube gap.

I believe that the simulation study presented here enhances our quantitative and qualitative understanding of the role of bile salts like SC in enhancing the dispersion stability of individual SWCNTs in aqueous solution. Moreover, this study may shed light on the future design of novel surfactants capable of more efficiently stabilizing aqueous dispersions of other nanoscaled materials, such as graphene, which will be discussed in details in Chapter 3. In the case of bile-salt analogues, such a design may include enhancing the hydrophilic face of the “two-faced” surfactants by attaching more hydrophilic groups on the carbon backbone, or modifying the rigid chemical structure of the “two-faced” surfactants to better accommodate the curvature of SWCNTs.

## 2.5 Appendix: Supporting Tables and Figures

**Table 2-A1: Summary of Simulated Systems**

System	Number of Sodium Cholates Molecules	Number of Water Molecules	Total Number of Atoms	Simulation Box Size <sup>c</sup> (nm <sup>3</sup> )	Simulation Time (ns)
1 <sup>a</sup>	15	10,816	34,083	6.96 × 6.96 × 6.96	240 ns
2 <sup>a</sup>	25	10,572	34,041	6.95 × 6.95 × 6.95	240 ns
3-63 <sup>b</sup>	44	13,000	43,236	8.88 × 6.91 × 6.91	20 ns each

<sup>a</sup> Sodium cholates adsorption and surface self-assembly simulations on single (6,6) SWCNTs.

<sup>b</sup> Simulations for 61 intertube separations between two parallel confined (6,6) SWCNTs carried out to calculate the PMF.

<sup>c</sup> Averaged over the production run of the simulation with small fluctuations from the pressure coupling.

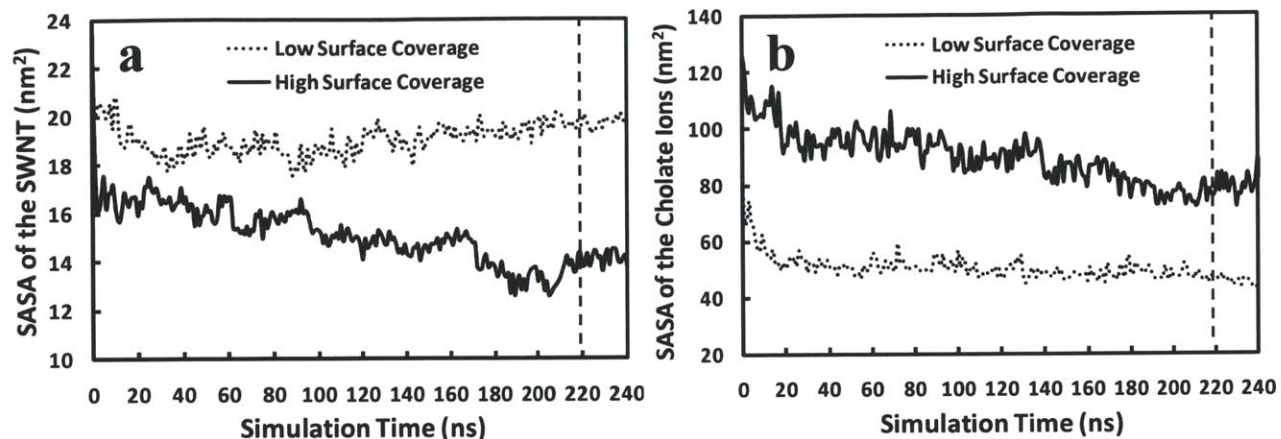


**Figure 2-A1:** Solvent accessible surface areas (SASAs) of: (a) a SWCNT and (b) the cholate ions under low and high SC surface coverages, monitored as a function of simulation time. As shown, the fluctuations in the SASA curves are significant at the beginning, and are dampened after about 200 ns, indicating that the system has reached equilibrium. Therefore, data analysis was performed during the last 20 ns of the entire simulation run, as indicated by the time period beyond the vertical dashed lines.

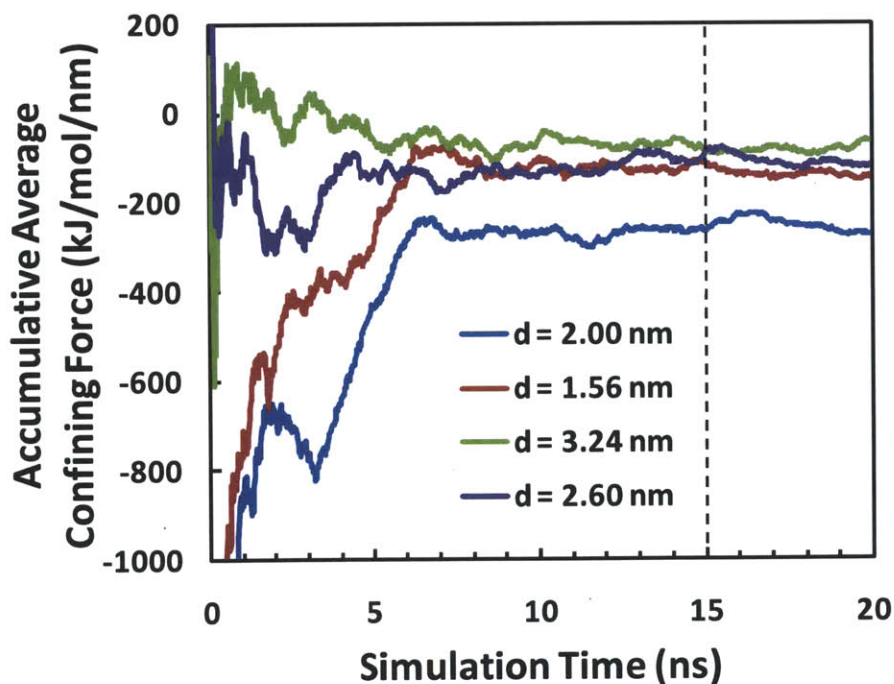


**Figure 2-A2:** Cumulative average forces as a function of simulation time at several selected intertube separations,  $d$ . As shown, the fluctuations in the force curves are significant at the beginning, and are dampened after about 10 ns, indicating that the system has reached equilibrium. Therefore, data analysis was performed during the last 5 ns of each simulation run, as indicated by the time period beyond the vertical dashed line.

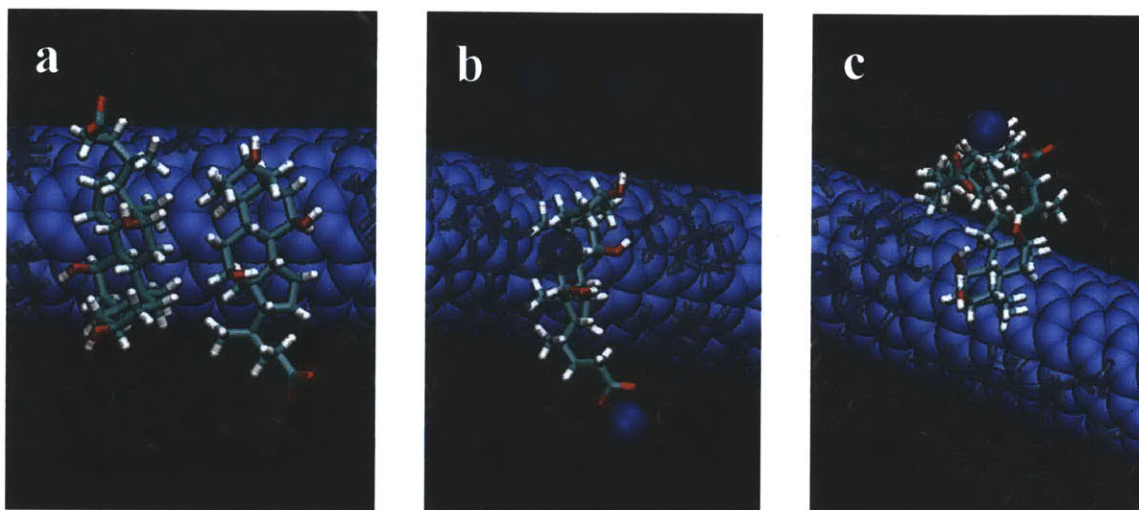


**Figure 2-A3:** Zoomed-in plots of representative post-equilibrium simulation snapshots of a (6,6) SWCNT in aqueous SC solutions, showing that: (a) the cholates prefer to self-assemble side-by-side (perpendicular to the nanotube axis) in order to minimize contact of their hydrophobic faces with water, (b) the side-by-side self assembly is facilitated by the condensation of positively-charged sodium counterions onto the negatively-charged carboxylate group of a single cholates ion, and (c) the side-by-side self assembly is also facilitated by the condensation of a positively-charged sodium counterion onto the negatively-charged carboxylate groups of two cholates ions. Water molecules are not shown in all the plots for clarity. Note that in (a), the sodium counterions are also not shown for clarity, and all the irrelevant cholates ions are shown in a transparent fashion in order to highlight the relevant ones. In addition, in (b), all the irrelevant cholates ions and sodium counterions are shown in a transparent fashion in order to highlight the relevant ones. The color code is the same as that in Figure 2-2.

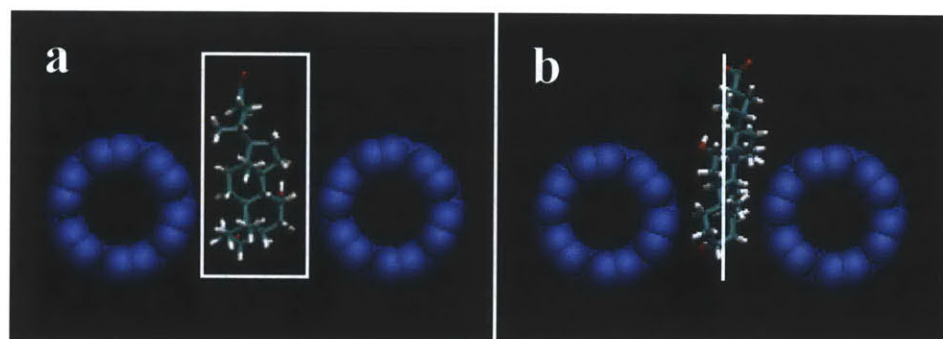


**Figure 2-A4:** Post-equilibrium MD simulation snapshots at intertube separations of: (a) 1.96 nm and (b) 1.68 nm, illustrating the orientation of the steroid-ring plane of one cholates ion when only a single layer of cholates ions resides within the intertube gap. At  $d = 1.96$  nm, the plane in white orients perpendicular to the SWCNT surface in order to accommodate the fixed, sparsely-packed intertube gap, while at  $d = 1.68$  nm, the plane in white orients parallel to the SWCNT surface.

## Chapter 3

### Molecular Insights into the Surface Morphology, Layering Structure, and Aggregation Kinetics of Surfactant-Stabilized Graphene Dispersions

#### 3.1 Introduction

In Chapter 2, I discussed the role of surfactants in stabilizing SWCNTs in aqueous solutions. Surfactants are also very important in the solution-phase production of graphene at the large scale. As discussed in Section 1.1, graphene, a two-dimensional, one-atom-thick hexagonal lattice of carbon atoms,[13] has generated considerable attention as a result of its outstanding electronic, mechanical, optical, thermal, and chemical properties.[15] While the earliest graphene samples were produced using micromechanical cleavage from highly-ordered pyrolytic graphite (HOPG),[13, 14] significant effort has been devoted in recent years to develop larger scale methods to produce graphene. Such methods involve two main approaches: direct chemical growth of graphene on substrates (e.g., chemical vapor deposition, CVD),[27, 136] and direct exfoliation of graphene from naturally occurring graphite flakes in various solvents.[43, 50] As discussed in Section 1.2, the latter, solution-phase method offers several significant advantages since it: (i) utilizes inexpensive and readily available graphite flakes, (ii) does not require transferring the graphene from the growth substrate, (iii) employs existing technologies (e.g., sonication and centrifugation) for scaled-up large volume processing, and (iv) allows solution-phase chemical functionalization of graphene.[43]

Among various available solvents, the use of water avoids the toxic polar organic solvents (e.g., NMP[137] and DMF[58]), and allows the use of graphene for biological applications, including molecular sensors and transistors.[138-140] Due to the hydrophobic nature of pristine graphene, the use of surfactants is essential to assist in the dispersion of graphene in an aqueous phase. It was recently demonstrated that graphite flakes (from inexpensive graphite powder) can be

exfoliated and dispersed into pristine, unfunctionalized graphene sheets in aqueous media using the conventional linear ionic surfactant sodium dodecylbenzene sulfonate (SDBS), with the aid of bath sonication and centrifugation.[45] The electrostatic repulsions between the SDBS-covered graphene sheets were quantified experimentally by measuring the zeta potential of the graphene-SDBS assemblies using electrophoresis.[45] Very recently, the bile salt surfactant, sodium cholate (SC), has also been utilized to disperse graphene in aqueous solution at high concentrations.[141] Moreover, Green et al. utilized horn ultrasonication and density gradient ultracentrifugation (DGU) to isolate SC-stabilized graphene with controlled thickness.[40] However, the graphene dispersions reported in Ref. [40] were found to be turbostratic (non-AB stacked) after DGU, as quantified using Raman spectroscopy.

It is well known that solution-phase graphene dispersions are polydisperse with various layer numbers and interlayer registrations (layering structure), where these characteristics determine the electronic and optical properties.[23] For multilayer graphene, the Bernal AB-stacking found in natural graphite is the most energetically favorable structure. More importantly, AB-stacked multilayer, most notably, bilayer and trilayer, graphene have properties that are distinct from those of monolayer graphene (which is a semimetal with zero bandgap). This is because bilayer and trilayer graphene exhibit tunable bandgaps in response to applied gate bias or external electric fields,[20, 142] thus imparting great flexibility in the design and optimization of electronic and optical devices. However, the solution-phase exfoliated bilayer and trilayer graphene sheets after DGU exhibit primarily a turbostratic, non-AB stacking structure, as quantified using Raman spectroscopy.[40] This is similar to what is observed in CVD-graphene samples and those grown on SiC,[143] and suggests disordering of the graphene sheets due to the weak interlayer coupling. As a result, most of the multilayer graphene, except for those produced using micromechanical cleavage, are turbostratic, where slight deviations from the AB stacking destroys the unique electronic structures of bilayer and trilayer graphene, and renders them electronically similar to monolayer graphene.[29] For example, theoretical analysis has predicted that an external electric field, applied normal to the turbostratic bilayer graphene, cannot open an

electronic bandgap.[144] Therefore, understanding the formation of the turbostratic layering structure of multiplayer graphene is very important to improve the solution-phase exfoliation process. If layering can be controlled during exfoliation, this would provide a viable route for the mass-production of AB-stacked multilayer graphene on arbitrary substrates for electronic devices. When combined with the well-developed intercalation chemistry of graphite,[145] it becomes possible to obtain graphene dispersions with layering control. Graphene sheets from covalent graphite intercalation compounds (GICs),[146-148] ionic GIC,[46, 149, 150] and expanded graphite (EG)[151] have been reported. Very recently, our group successfully utilized Stage-2 and Stage-3 ionic GICs to produce AB-stacked bilayer- and trilayer-enriched graphene dispersions with the aid of slow homogenization and mild centrifugation, respectively.[152]

Another notable approach to modify the electronic properties (e.g., opening bandgaps) of graphene is to covalently functionalize the surface of graphene with special reactants.[73, 153] The source for functionalization can be either from defect-free graphene from micromechanical exfoliation,[13, 14] CVD growth,[27, 136] and solution exfoliation,[40, 45] or from reduced graphene oxides (GOs) which are produced from graphite oxidation and have many defects (also referred to as chemically converted graphene, CCG).[153] The extent of reaction of graphene with the reactants, most notably, diazonium salts, is largely controlled by the amounts of available reaction sites on the graphene surface,[73] similar to the functionalization of single-walled carbon nanotubes (SWCNTs), which will be discussed in detail in Chapter 4.[154] Since most of the reactions take place in aqueous media, anionic surfactants are usually added to either disperse graphene before functionalization,[153] or to accelerate the reaction process by concentrating the diazonium cations near the graphene surface.[73] According to the two-step reaction mechanism proposed by Usrey et al.,[90] the only selective step in the functionalization process of SWCNTs is not the actual reaction, but the adsorption of reactants to the available binding sites on the surfactant-covered SWCNT surface. If I draw analogies between SWCNT and graphene, then, the available reaction sites should be determined by the surfactant surface coverage. In addition, the adsorption of the diazonium cations onto the ionic surfactant-covered



graphene surface should also be greatly affected by the sign of the charge of the surfactant molecules due to electrostatic interactions.

In spite of the extensive experimental reports on solution-phase graphene production and functionalization, to date, a molecular understanding of the surface morphology of monolayer and multilayer graphene-surfactant assemblies has not been developed. In addition, the origin of the turbostratic multilayer graphene structure following the DGU process in the work by Green et al. has not been elucidated.[40] Furthermore, the mechanism underlying the dispersion stability and aggregation kinetics of surfactant-stabilized graphene, produced by aqueous solution-phase exfoliation, is not well understood. Theoretically, a simple model based on the traditional DLVO theory has been proposed to describe: (i) the electrostatic repulsions between graphene sheets imparted by the adsorbed ionic surfactants, and (ii) the strong van der Waals (vdW) attractions between the graphene sheets.[43, 45] Several molecular dynamics (MD) simulation studies of the adsorption of the conventional linear surfactant, sodium dodecyl sulfate (SDS), on graphite, rather than graphene, have been reported.[92, 104, 155] Very recently, our group has investigated the dispersion stability of liquid-phase-exfoliated graphene in organic polar solvents using MD simulations and the kinetic theory of colloid aggregation.[156]

With all of the above in mind, in the present study, I carried out molecular simulations, theoretical modeling, and experimental measurements to elucidate several important aspects of aqueous solution-phase exfoliated graphene dispersions. First, I carried out molecular dynamics (MD) simulations to investigate the surface morphology of the ionic surfactant sodium cholate (SC) on a monolayer graphene sheet. The electrostatic potential around the graphene-SC assembly was calculated using the simulated charge density profile through the Poisson equation, as well as the theoretical Poisson-Boltzmann (PB) equation, in order to estimate the zeta potential around the assembly as a quantitative measure of colloid stability. The computed zeta potential was further compared to the experimental value obtained in the present study for a SC-stabilized graphene aqueous dispersion, as well as to the value reported in the literature in the case of SDBS-stabilized graphene aqueous dispersions. To quantify the interactions between



graphene sheets covered with cholate ions, I subsequently carried out a potential of mean force (PMF) calculation for two parallel graphene-SC assemblies, as a function of the intersheet separation,  $d$ , and compared the simulated results with those predicted using the traditional DLVO theory. Based on the simulated PMF profile, I then proposed a surfactant-stabilized metastable structure for the exfoliated multilayer graphene sheets, which explains their turbostratic structure. Finally, to understand the kinetics of graphene aggregation, I combined the PMF results obtained using MD simulations with a kinetic theory of colloid aggregation to predict the time-dependent concentration and distribution of graphene with various thicknesses (or numbers of layers). I further decomposed each graphene layer type into subtypes, including the AB-stacked species and various turbostratic species. To study the dispersion stability of the graphene sheets in aqueous media, I prepared SC-stabilized graphene dispersions and monitored the graphene total mass concentration (including all graphene layer types) as a function of time based on the optical absorbance of the solution. Note that the initial layer number distribution of the prepared graphene sheets was characterized based on the experimentally-obtained 2D Raman spectra. These experimental data were also used as inputs to our kinetic model to obtain the average collision area which is the only fitting parameter in the model.

## **3.2 Methods**

### **3.2.1 Simulation Methods**

Simulations of the self-assembly of sodium cholate on the graphene surface in aqueous solution were carried out using the GROMACS 4.0 software package.[103] Monolayer graphene was modeled as an infinite rigid sheet in the x-y plane, similar to our recent simulations of graphene exfoliation in polar solvents.[156] The carbon atoms of graphene were treated as uncharged Lennard-Jones (LJ) spheres with  $\sigma = 0.34$  nm and  $\varepsilon = 0.223$  kJ/mol.[157] Water molecules and SC molecules were modeled using the SPC/E model[105] and the OPLS-AA force field,[107] respectively, similar to my recent simulations of SC-stabilized SWCNT aqueous dispersions.[158] Bond lengths and angles in water molecules were constrained using the SETTLE algorithm,[106]

while bond lengths in the cholate ions were constrained using the parallel version of the LINCS algorithm.[109] Lennard-Jones interactions were treated with a cutoff distance of 0.9 nm, with those between different atoms calculated using the standard geometric averaging rule implemented in the OPLS-AA force field.[107] Long-range electrostatic interactions were treated using the particle mesh Ewald (PME) summation method.[110, 111] The velocity-rescaled Berendsen thermostat was implemented to maintain a constant system temperature of 298.15 K.[114] The semiisotropic Berendsen pressure coupling was applied,[115] where a pressure of 1 bar is coupled only in the z direction, such that the x and y dimensions of the simulation box can be fixed to match the size of the graphene sheet.

In the present study, 28 SC molecules were initially positioned near each side of a 56.6 nm<sup>2</sup> monolayer graphene sheet (i.e., a total of 56 SC molecules on both sides), which yields a surface coverage of  $28/56.6 = 0.49$  molecule/nm<sup>2</sup> for each side of the sheet. As a point of reference, the experimental saturated SC surface coverage on a graphite surface, based on the Langmuir plot, was found to be around 0.38 molecule/nm<sup>2</sup>. [159] A more rigorous simulation study involving various SC surface coverages to estimate the saturated SC surface coverage is in progress. For comparison with the case without SC, I also simulated a graphene sheet in water in the absence of SC. The energy of the simulated system was first minimized using the steepest-descent method.[103] The simulated system was then equilibrated for 250 ns, and data were collected for another 50 ns. The simulation was confirmed to have reached equilibrium within 250 ns by monitoring the SASAs (solvent accessible surface areas) of the cholate ions and graphene as a function of time (see Figure 3-A1 in Appendix A). The simulated system size, including the total numbers of SC and water molecules, the total number of atoms, the size of the simulation box, and the total simulation time, are summarized in Table 3-A1 in Appendix A.

The electrostatic potential around the graphene-SC assembly,  $\Psi(z)$ , along the z-axis of the simulation box, normal to the graphene surface, is related to the local charge density,  $\rho(z)$ , via the Poisson equation:[160]

$$\frac{d^2\Psi(z)}{dz^2} = -\frac{\rho(z)}{\epsilon\epsilon_0} \quad (3-1)$$

where  $\epsilon_0 = 8.85 \times 10^{-12}$  C/m·V is the vacuum dielectric permittivity, and  $\epsilon = 78.5$  is the relative dielectric permittivity (or dielectric constant) of water at 25°. Note that the charge density,  $\rho(z)$ , results from the partial charges assigned to all the atoms in the system according to their force fields. In MD simulations,  $\Psi(z)$  is calculated by integrating  $\rho(z)$  twice along the z-axis numerically after dividing the simulation cell into many slabs along the z-axis. Details on the calculation of the electrostatic potential can be found in a recent review.[161]

To investigate the interactions between two parallel SC-covered graphene sheets, I calculated the potential of mean force (PMF) at various intersheet separations (along the z-axis of the simulation box),  $d$ , from  $d_1 = 0.9$  nm to  $d_2 = 3.4$  nm, with an increment of 0.05 nm. For  $d \leq 0.9$  nm, the two graphene sheets cannot be compressed any further in my simulations due to the extremely long simulation time required for equilibration. For  $d \geq 3.4$  nm, the average force exerted by the two graphene sheets is very close to zero. The PMF is calculated by numerically integrating, in a trapezoidal manner, the time-averaged force,  $\langle F(d) \rangle$ , exerted to separate the two graphene sheets at various  $d$  values. Specifically,[93]

$$PMF(d) = \int_d^{d_2} \langle F(r) \rangle dr \quad (3-2)$$

where  $r$  is the reaction coordinate which is the same as  $d$ . For a detailed discussion of the PMF calculations, the interested reader is referred to my recent publications[156, 158]. Note that, in the PMF simulations, the x and y dimensions of the simulation box are larger than the lateral size of the graphene sheets (see Table 3-A1 in Appendix A), in order to allow molecules which are confined between the two graphene sheets to escape from the intersheet gap. As a result, the graphene sheets in the PMF calculations are no longer infinite in the x-y plane, and therefore, an isotropic pressure coupling was applied to carry out the PMF calculations. The equilibration of each simulation run was verified by the convergence of the cumulative average force as a function of the simulation time, as shown in Figure 3-A2 in Appendix A.

### 3.2.2 Experimental Methods

The bilayer-enriched SC-stabilized graphene dispersion, as reported in my recent work,[152] was used for the time-dependent graphene total mass concentration measurements carried out in the present study. The graphene solution was first decanted into 3 quartz cuvettes (to determine statistical errors), and the solution optical absorbance was then measured using a UV/visible spectrophotometer (Beckman Coulter DU800). The optical absorbance of the 2 wt% SC solution, which was used to prepare the graphene solution, was also measured and used as a reference. The correlation between the graphene total mass concentration and the optical absorbance per unit path length ( $A/l$ ) was determined based on the Lambert-Beer law ( $A = \alpha C_0 l$ , where  $C_0$  is the initial graphene total mass concentration measured using vacuum filtration,  $\alpha$  is the absorbance coefficient, and  $l = 0.01$  m for the cuvette).[162] The graphene total mass concentration (in mg/L),  $C(t)$ , was monitored for two weeks based on the optical absorbance of the solution. The zeta potential of the graphene dispersion was measured using a Brookhaven ZetaPALS instrument at room temperature. The experimental procedures to prepare and characterize bilayer-enriched graphene dispersion using Stage-2 graphite intercalation compounds (GICs) are summarized in Appendix B.

## 3.3 Results and Discussion

### 3.3.1 Surface Morphology of the Monolayer Graphene-SC Assembly

Representative post-equilibrium simulation snapshots of a monolayer graphene sheet covered with cholate ions are shown in Figures 3-1-a and 3-1-b. Similar to the surface self-assembly structure of cholate ions on a SWCNT,[158] the cholate ions adsorb parallel to the graphene surface, with their hydrophilic faces (having oxygen atoms shown as red spheres in Figure 3-1-c) located farther away from the hydrophobic graphene surface, and consequently, with their hydrophobic faces facing the hydrophobic graphene surface. This finding is consistent with the speculation that the planar SC molecules form a stable charged encapsulation layer on each side of the suspended graphene sheets.[40] This organization tends to maximize the contact between

the hydrophobic faces of the cholate ions and the graphene surface, and is driven by the hydrophobic effect.[30] Another interesting feature in the front-view simulation snapshot in Figure 3-1-a is that, instead of distributing uniformly on the graphene surface, the adsorbed cholate ions prefer to self-assemble side-by-side, also due to the hydrophobic effect.[30] Note that this side-by-side SC organization (highlighted by the orange dashed ellipse) tends to minimize contact between the hydrophobic faces of the cholate ions and water. This side-by-side SC self-assembly is also facilitated by the condensation (or binding) of positively-charged sodium counterions onto single, or multiple, negatively-charged cholate ions (typically, onto the charged carboxylate groups, as shown in Figures 3-1-a and 3-1-b). Indeed, the sodium counterion condensation shields the electrostatic repulsions between the charged carboxylate groups and effectively brings them closer to each other.

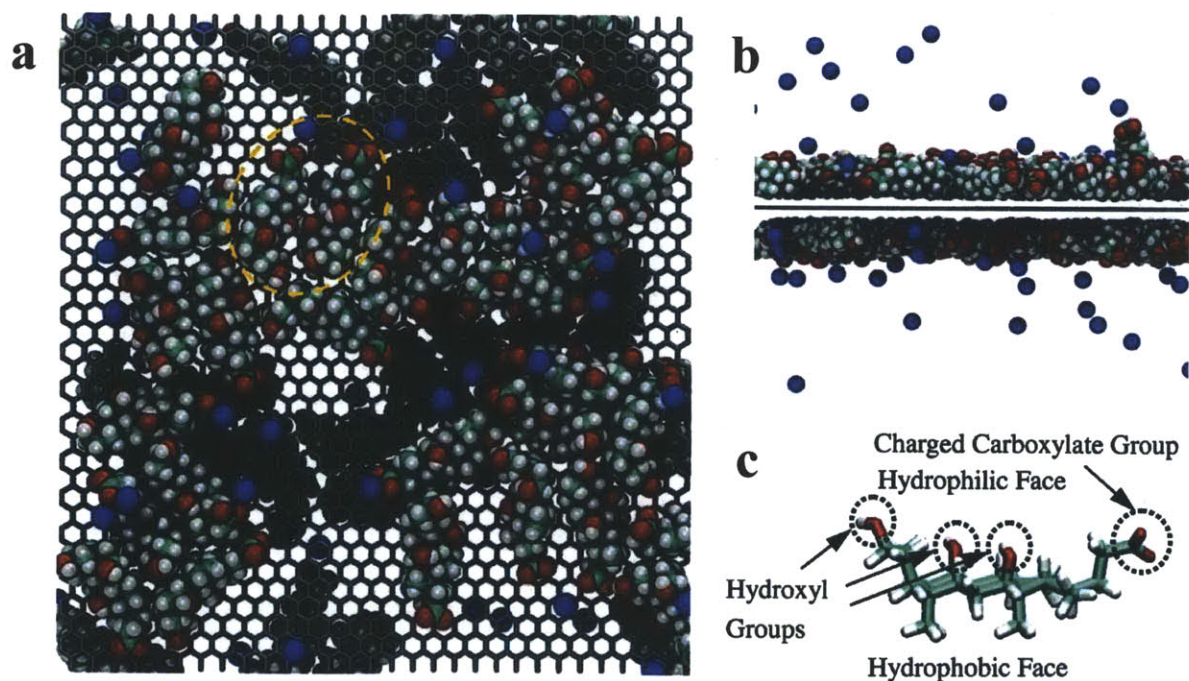


**Figure 3-1:** Representative post-equilibrium simulation snapshots of SC-stabilized monolayer graphene: (a) top view, (b) side view, and (c) chemical structure of the cholate ion. Water molecules are not shown for clarity. Note that in (a) and (b), SC is shown in the volume-filled form, while the graphene sheet is shown in the stick form. The cholate ions at the back of the graphene sheet can also be visualized in a darker fashion. Note that the orange dashed ellipse highlights two side-by-side self-assembled SC molecules. Color code: red – oxygen, blue – sodium, light green – carbon, white – hydrogen, and silver – graphene carbon.

The organization of SC on the graphene surface is further quantified in the density profiles of the water molecules, the cholate ions, and the sodium counterions along the z-axis (normal to the graphene sheet, see Figure 3-2-a). The density profile of the cholate ions (red line in Figure 3-2-a) indicates that they prefer to distribute in a very compact manner within 1 nm on the graphene surface (where the density profile decays to zero beyond  $z = \pm 1$  nm). Taking into account the thickness of the graphene sheet ( $\approx 0.4$  nm), the result in Figure 3-2-a shows that cholate ions aggregate as a compact layer with a thickness of  $1 \text{ nm} - 0.4 \text{ nm}/2 = 0.8$  nm, consistent with their molecular thickness of around 0.7 nm. The sodium counterion condensation effects can also be observed in Figure 3-2-a, where the largest peak of the density profile of the sodium counterions around the graphene sheet (green line,  $z = \pm 0.75$  nm) is closely located to the largest peak of the cholate ions (red line,  $z = \pm 0.5$  nm), reflecting the strong electrostatic attractions between these oppositely-charged ions. The difference between these two peaks,  $0.75 - 0.5 = 0.25$  nm, is consistent with the vdW radius of 0.21 nm of a sodium counterion. The unbound sodium counterions diffuse away from the graphene-SC assembly to the bulk region (with a bulk concentration of around  $1.7 \text{ kg/m}^3$ , measured at the z-boundary of the simulation box). Water ordering on the hydrophobic graphene surface is well known in the literature,[163] which is demonstrated by fluctuations (with sharp peaks representing the hydration layers) in the density profile near the graphene surface (the blue dashed line in Figure 3-2-a corresponding to the water density profile without SC). Interestingly, in the presence of the adsorbed cholate ions (the blue line in Figure 3-2-a), the first and the second hydration layers, corresponding to the two closest peaks in the density profile at each side of the graphene sheet, are suppressed (about 50% for the first hydration layer, with the second hydration layer no longer visible) compared to the case without SC. It is noteworthy that the third hydration layer is not affected at all, because the cholate ions do not extend beyond the location of the second hydration layer.



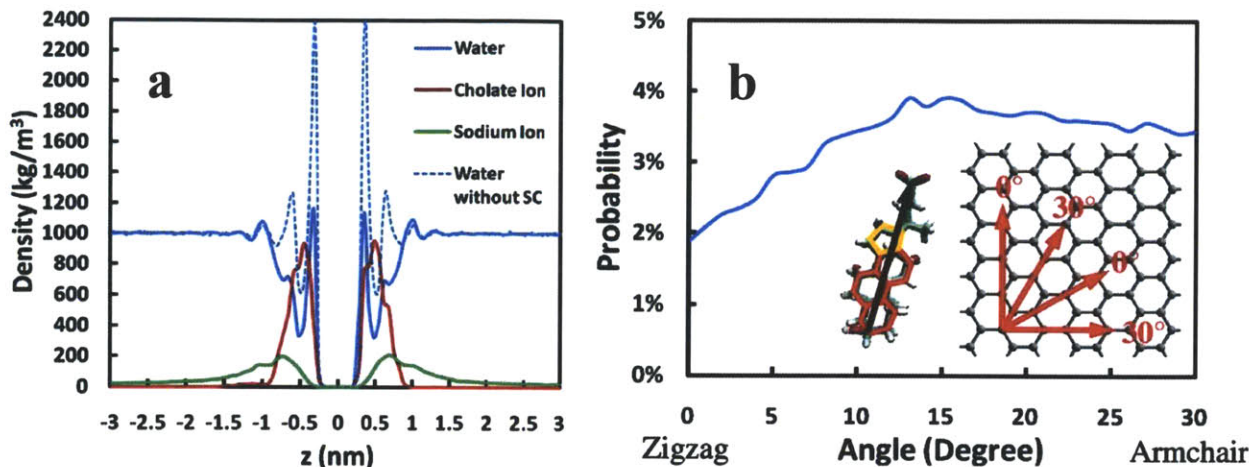


**Figure 3-2:** (a) Simulated density profiles of water molecules, cholate ions, and sodium counterions along the z-axis normal to the monolayer graphene. Note that the z-axis was shifted so that the graphene sheet is located at  $z = 0$ . The water density profile for the simulation of graphene in water, without SC, is shown as the blue dashed line for comparison. Note also that the density of the sodium counterions was amplified 10 times for clarity. (b) Simulated distribution profile of the angles (with a  $1^\circ$  interval) between the principal axis of the cholate ions and the zigzag axis ( $0^\circ$ ) of graphene. In the SC molecular structure shown, the solid black line connecting the carbon atom in the carboxylate group with the carbon atom at the end of the steroid ring defines the principal axis of the cholate ion. Furthermore, the three red hexagonal rings represent the “armchair-like” cyclohexane rings in the cholate ion, while the orange pentagonal ring represents the cyclopentane ring in the cholate ion.

As discussed earlier, the cholate ions prefer to adsorb parallel to each other on the graphene surface. However, the precise orientations of the cholate ions with respect to the zigzag or armchair axes of graphene still need to be determined. For this purpose, I calculated the distribution of the angles (with a  $1^\circ$  interval) between the principal axis of the cholate ions (defined in Figure 3-2-b) and the zigzag axis of graphene. As shown in Figure 3-2-b, the cholate ions orient quite uniformly on the graphene sheet (the probabilities range from 2% to 4%). In other words, the cholate ions do not exhibit a large tendency to orient along the zigzag ( $0^\circ$ ) or the armchair ( $30^\circ$ ) axes of graphene. However, they do exhibit a small tendency to orient in between the two axes (the largest peak in the angle distribution profile corresponds to  $15^\circ$ ). Comparing the angle distribution near  $0^\circ$  and  $30^\circ$ , one can conclude that the cholate ions have a slightly greater tendency to orient along the armchair axis than along the zigzag axis. This angular orientation is probably due to the fact that the three cyclohexane rings in the cholate ion (see

Figure 3-2-b) form an “armchair-like” structure (with respect to its principal axis), which favors the orientation along the armchair axis of graphene. Furthermore, it is highly possible that the cyclopentane ring in the cholate ion (see Figure 3-2-b) disfavors such an orientation and shifts the peak to 15°.

Finally, to confirm that the simulated surface coverage of cholate ions agrees with the experimental saturated value, I calculated the density of a monolayer graphene-SC assembly,  $\rho_{GRA-SC}$ , by averaging the total density profile along the z-axis (including those corresponding to the graphene sheet,  $\rho_{GRA}$ , the cholate ions,  $\rho_{Cholate}$ , the sodium counterions,  $\rho_{Sodium}$ , and the bound hydration shell of water molecules,  $\rho_{Water}$ ) from  $z_1 = -1.5$  to  $z_2 = 1.5$  nm (see Figure 3-2-a), as follows:

$$\rho_{GRA-SC} = \frac{1}{z_2 - z_1} \int_{z_1}^{z_2} (\rho_{GRA} + \rho_{Cholate} + \rho_{Sodium} + \rho_{Water}) dz \quad (3-3)$$

The bound hydration shell of water molecules is defined to be located along the z-axis from  $z_1 = -1.5$  to  $z_2 = 1.5$  nm. Note that  $z = \pm 1.5$  nm corresponds to the position where the water density profile initially reaches its bulk value (namely, beyond  $z = \pm 1.5$  nm, the water density fluctuations begin to disappear, see Figure 3-2-a). Consistent with the buoyant density of the monolayer graphene-SC assembly measured experimentally (1.16 g/mL),[40] the simulated value of  $\rho_{GRA-SC}$  is equal to 1.18 g/mL. Note that the experimentally-estimated saturated surface coverage of SC on graphene, obtained by fitting the buoyant densities of the graphene-SC assemblies comprising various graphene layers to a simple geometric model (1.35 molecules/nm<sup>2</sup>),[40] is about two times larger than the simulated value (0.49 molecules/nm<sup>2</sup>). For comparison, the experimental saturated SC surface coverage on the graphite surface estimated based on a Langmuir plot is approximately equal to 0.38 molecule/nm<sup>2</sup>,[159] which is significantly closer to the simulated value. In the simulation, the cholate ions only partially cover the graphene surface with an estimated fraction of 60% of the graphene surface area, based on



the surface area of  $1.5 \text{ nm} \times 0.8 \text{ nm} = 1.2 \text{ nm}^2$  occupied by a cholate ion. On the other hand, the experimentally-reported value is 94%, based on a surface area of  $0.7 \text{ nm}^2$  occupied by a cholate ion,[40] which is smaller than the value that I estimated. I believe that this discrepancy is probably due to the limitation of the simple geometric model proposed by Green et al.,[40] which is based on the assumption that there are no molecules confined between multilayer graphene sheets (see discussion in Section 3.4).

Interestingly, visual analysis of Figure 3-1-a suggests that the cholate ions adsorbed on the two sides of the graphene sheet overlap very little with each other, with a visually estimated overlap area of 25% over the graphene surface area. Note that the theoretical minimum overlap area should be  $2 \times 60\% - 100\% = 20\%$  over the graphene surface area. On the other hand, the overlap area for cholate ions that are independently distributed on each side of the graphene sheet should be  $60\% \times 60\% = 36\%$  over the graphene surface area. This difference may be due to the correlation between the cholate ions on each side of the graphene sheet resulting from electrostatic repulsions between the negatively-charged cholate ions, which favors a smaller overlap area.

### 3.3.2 Electrostatic Potential around the Monolayer Graphene-SC Assembly

The simulated electrostatic potential,  $\Psi(z)$ , around the graphene-SC assembly, along the positive z-axis, is shown in Figure 3-3. For comparison, I predicted the electrostatic potential based on the traditional Poisson-Boltzmann (PB) equation. It is quite reasonable to assume that the cholate ions are bound tightly onto the graphene surface and do not contribute to the solution ionic strength, since the simulated concentration of the cholate ions in the bulk solution is negligible compared to that of the sodium counterions. This results in:[160]

$$\frac{d^2\Psi(z)}{dz^2} = -\frac{\rho_\infty}{\epsilon\epsilon_0} \exp\left(-\frac{e\Psi(z)}{k_B T}\right) \quad (3-4)$$

where  $\rho_\infty = 7.12 \times 10^6 \text{ C/m}^3$  is the bulk charge density of the sodium counterions based on their

bulk concentration of  $1.7 \text{ kg/m}^3$  (obtained in Section 3.1),  $e = 1.60 \times 10^{-19} \text{ C}$  is the electronic charge,  $k_B = 1.38 \times 10^{-23} \text{ J/K}$  is the Boltzmann constant, and  $T = 298.15 \text{ K}$  is the simulated room absolute temperature. By solving Eq. (3-4) at the simulated boundary conditions, where  $\Psi = 0$  and  $d\Psi/dz = 0$  at the  $z$ -boundary of the simulation box, I obtain:[160]

$$\Psi(z) = \frac{2k_B T}{e} \ln\left(\cos \frac{\kappa z}{\sqrt{2}}\right) \quad (3-5)$$

where  $\kappa = \sqrt{\frac{e\rho_\infty}{\epsilon\epsilon_0 k_B T}}$  is the inverse of the Debye-Hückel (DH) screening length (or the double-layer thickness). Note that the result in Eq. (3-5) is different from that obtained using the Gouy-Chapman theory,[160] which yields the solution to the PB equation at a different boundary condition where  $\Psi(z \rightarrow \infty) = 0$ . Furthermore, note that due to the periodic boundary conditions imposed by the simulation box, the predicted  $\Psi(z)$  profile was shifted such that  $\Psi(z_{\max}) = 0$ , where  $z_{\max} = \pm 3.2 \text{ nm}$  is the boundary of the simulation box along the  $z$ -axis, in order to allow comparison with the simulated  $\Psi(z)$  profile.

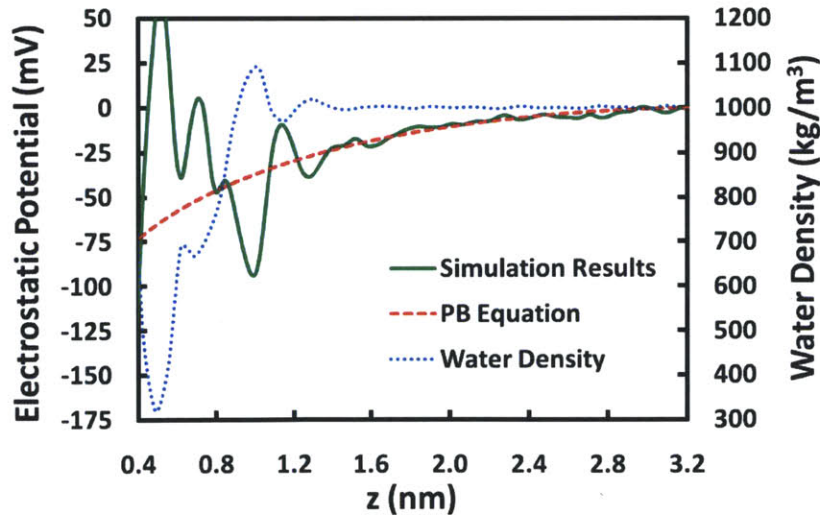


**Figure 3-3:** Simulated electrostatic potential around the graphene-SC assembly as a function of  $z$ , compared to that predicted based on the traditional Poisson-Boltzmann (PB) equation. The water density profile is shown for comparison purposes.

As shown in Figure 3-3,  $\Psi(z)$  predicted using the PB equation (the red dashed line) is always negative due to the negatively-charged cholate ions adsorbed on the graphene surface. In the far-field continuous aqueous media region away from the graphene surface ( $z \gg 1/\kappa$ , Debye-Hückel screening length,  $1/\kappa = 1.6$  nm), the simulated  $\Psi(z)$  (the green line) agrees very well with  $\Psi(z)$  predicted using the PB equation, whose magnitude decays in an exponential manner due to the screening effects of the positively-charged sodium counterions. However, in the near-field region close to the graphene surface ( $z \leq 1/\kappa = 1.6$  nm), the simulated  $\Psi(z)$  fluctuates significantly, unlike the smooth curve obtained using the PB equation for  $z \gg 1.6$  nm. By comparing the fluctuations in the simulated water density profile (the blue dotted line) and in the simulated  $\Psi(z)$ , one can observe a strong negative correlation between the simulated water density and  $\Psi(z)$  profiles (i.e., when there is a peak in  $\Psi(z)$ , there is a valley in the water density profile, and vice versa). This results from the algorithm used to divide the  $z$ -dimension of the simulation box into small slabs (0.05 nm in thickness) to determine the water density profile and  $\Psi(z)$ . For water molecules which are highly ordered, there is a non-uniform distribution of mass inside of each slab. The slabs in which more oxygen atoms (heavier than hydrogen atoms) are located, will possess higher local densities, corresponding to the peaks in the water density profile. Similarly, the hydrogen atoms contribute to the valleys in the water density profile. By drawing the analogy between mass and charge and taking into account the relations between  $\Psi(z)$  and the local charge density,  $\rho(z)$ , through Eq. (3-1), one can observe that the negatively-charged oxygen atoms contribute to the valleys in  $\Psi(z)$ , while the positively-charged hydrogen atoms contribute to the peaks in  $\Psi(z)$ . I can therefore conclude that the fluctuations observed in the simulated  $\Psi(z)$  profile result from the ordering of water molecules near the graphene surface, a discrete molecular event that cannot be reproduced by the traditional PB equation where water is treated as a continuum.[164]

In order to determine the zeta potential,  $\zeta$ , of the graphene-SC assembly, one needs to determine the location of the surface of shear at which  $\zeta$  is defined.[31] Considering the surface of the graphene-SC assembly as a negatively-charged wall due to the adsorbed cholate ions, an

appropriate definition of the surface of shear is the outer surface of the cholate ions, where the density profile of the cholate ions approaches zero at  $z = 1$  nm (see Figure 3-2-a). The simulated  $\zeta$  is equal to  $-93$  mV at  $z = 1$  nm, which is about two times larger in magnitude than the  $\zeta$  value predicted using the PB equation ( $-37$  mV). For comparison, the zeta potential for SC-stabilized graphene measured in the present study is  $-45 \pm 5$  mV based on 5 different measurements, which is similar to the reported value of  $-50$  mV for SDBS-stabilized graphene.[45] Based on the simulated  $\zeta$  value, I can conclude, not surprisingly perhaps, that the traditional PB equation is not able to accurately predict the near-field properties, including  $\zeta$ , of graphene-SC assemblies. It is also quite clear that the commonly used Debye-Hückel (DH) approximation to the PB equation (which should be appropriate when  $|\zeta| \ll k_B T / e = 25.7$  mV for monovalent ions),[160] cannot be used in the case of graphene-SC assemblies for which  $\zeta = -93$  mV. Note that charged surfactants adsorbed on the graphene surface may facilitate the adsorption of oppositely-charged reactants present in the solution.[73] As a result, the impact of the graphene surface charge resulting from charged surfactant adsorption is also an important factor in determining the functionalization selectivity of graphene, in addition to the surfactant surface coverage. Moreover, specific binding (e.g., hydrophobic bonding, hydrogen bonding, or ring stacking) between surfactants and reactants should also be taken into consideration in determining the functionalization selectivity of graphene.

### 3.3.3 Interactions between Two Graphene-SC Assemblies

The interactions between two parallel graphene-SC assemblies were quantified using the potential of mean force (PMF) between them, as a function of the intersheet separation,  $d$ , as shown in Figure 3-4-a. The simulated PMF profile (the red circles) exhibits a primary, long-range repulsive potential energy barrier possessing a maximum of around 10 kJ per mole and per unit area (in  $\text{nm}^2$ ) of the simulated graphene sheet, extending from  $d = 1.2$  to 3.4 nm. The PMF profile in Figure 3-4-a also exhibits a local energy minimum of  $-3$  kJ/mol· $\text{nm}^2$  at  $d = 1.05$  nm. As  $d$  decreases further from 1.05 to 0.9 nm, the PMF profile goes up sharply until the point

where the two graphene sheets cannot be compressed any further in my simulations due to the extremely long simulation time required for equilibration.

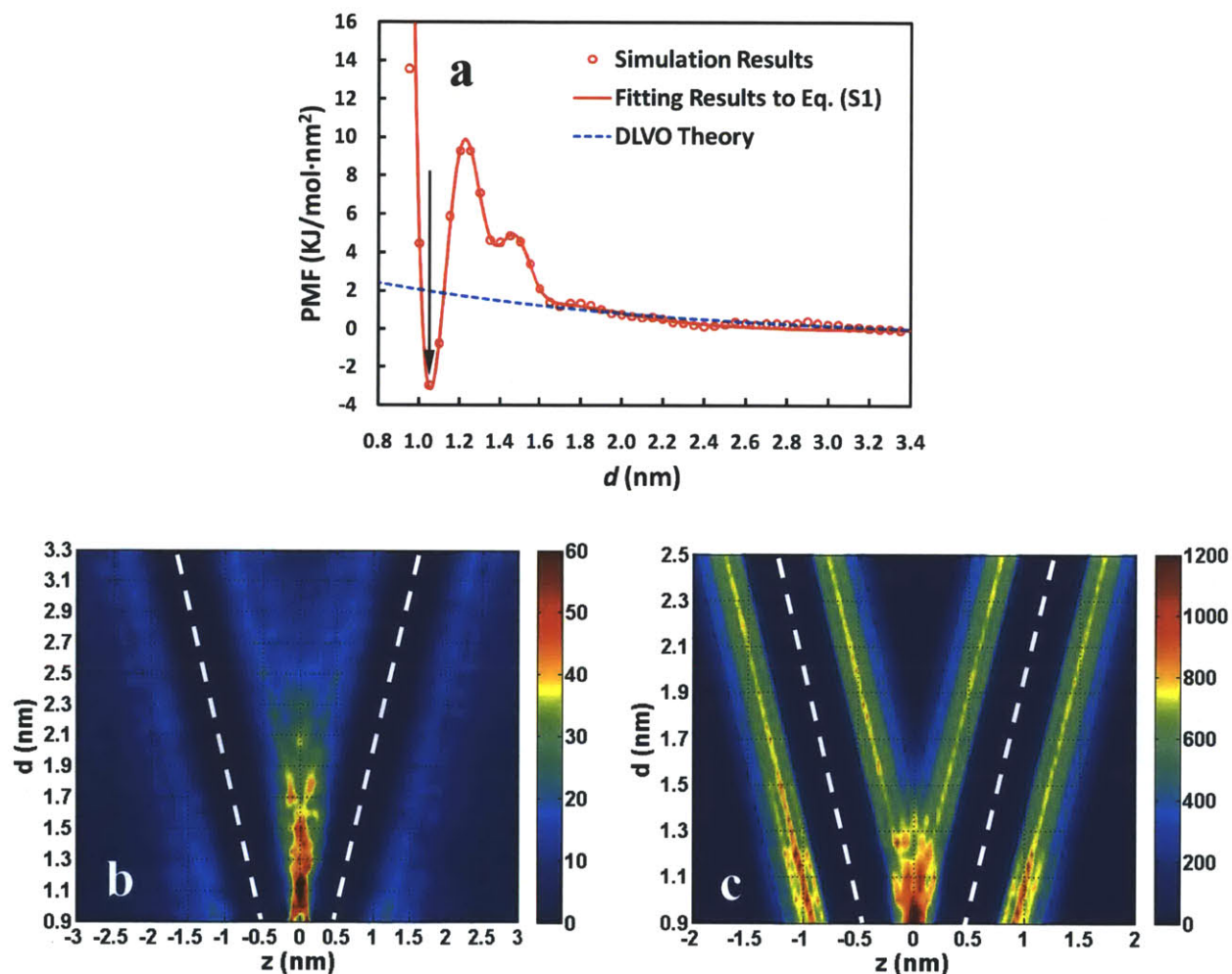


**Figure 3-4:** (a) Simulated potential of mean force (PMF) between two parallel graphene-SC assemblies as a function of the intersheet separation,  $d$ . The fitting results to the simulated PMF data (shown in red circles) using Eq. (3-A1) in Appendix C corresponds to the red solid line. The predicted electrostatic repulsive potential using the DLVO theory corresponds to the blue dashed line, and is shown for comparison. Note that the arrow shows the position of the local minimum at  $d = 1.05$  nm in the PMF profile. (b) & (c) The contour plots of the density (in units of  $\text{kg/m}^3$ ) profiles of: (b) the sodium counterions, and (c) the cholate ions, both along the  $z$ -axis, as a function of  $d$ . The red-color regions illustrate the existence of: a sodium ion wall in (b), and a single layer of cholate ions in (c), both being confined by the two graphene sheets. Note that the density increases as the color changes gradually from blue to red. Note also that the white dashed lines denote the  $z$ -axis positions of the graphene sheets, as a function of  $d$ .

From  $d = 2.2$  to  $3.4$  nm, the onset of the repulsive potential energy barrier in the PMF profile is due to the long-range electrostatic repulsion between the two parallel graphene-SC assemblies, which behave as two parallel, negatively-charged plates, mediated by the positively-charged sodium counterions. This contribution to the potential energy barrier has been widely recognized to result from the electrostatic contribution which appears in the traditional DLVO theory.[160] Considering that the DH approximation for low potentials is not appropriate for the case considered here, the repulsive electrostatic potential per unit area in the DLVO theory should be calculated under the weak-overlap approximation as follows:[160]

$$U(d) = \frac{64k_B T \rho_\infty \gamma^2}{e \kappa} \exp(-\kappa d) \quad (3-6)$$

where  $\gamma = \tanh\left(\frac{e\Psi_0}{4k_B T}\right)$ , and the surface potential  $\Psi_0$  can be calculated using the Grahame equation,[160] where  $\Psi_0 = -\frac{k_B T}{e} \ln\left(\frac{e\sigma^2}{2\varepsilon\varepsilon_0 k_B T \rho_\infty} + 1\right) = -83$  mV, and the surface charge density resulting from the bound cholate ions,  $\sigma = -0.08$  C/m<sup>2</sup>. Note that this value of  $\Psi_0$  is slightly different from that of the simulated zeta potential  $\zeta = -93$  mV. This is due to the fact that the  $\zeta$  value was obtained from the monolayer graphene simulation rather than from the bilayer graphene simulation used here. In addition, note that the calculated  $U(d)$  profile in Eq. (3-6) was shifted such that  $U(d_{\max}) = 0$ , where  $d_{\max} = 3.4$  nm is the largest intersheet separation, to allow comparison with the simulated PMF profile.

As shown in Figure 3-4-a, the simulated repulsive electrostatic potential and that predicted using the DLVO theory (Eq. (3-6), blue dashed line) agree very well in the far-field continuous aqueous media region ( $d \geq 1.6$  nm). In addition, the DLVO contribution to the primary potential energy barrier is quite small, which is somewhat unexpected based on recent theoretical reports,[43, 45] due to the fact that only the electrostatic effect was considered in these reports.

As expected, the DLVO theory prediction deviates significantly from the simulated PMF in the near-field region ( $d \leq 1.6$  nm) due to the neglect of the molecularity of the directly contacted cholate ions, sodium counterions, and water molecules in the DLVO theory. As will be discussed in Section 3.4, the major contribution to the energy barrier inhibiting graphene aggregation is the steric repulsion exerted by the sodium counterions wall and the single layer of cholate ions which are confined between the two graphene sheets. This finding is consistent with my recent simulation studies on: (i) surfactant-stabilized SWCNTs,[158] and (ii) liquid-phase-exfoliated graphene in polar solvents.[156] Note that, typically, only long-chain polymers are presumed theoretically to contribute to the steric repulsion between colloiddally-dispersed particles such as graphene.[165] On the other hand, I demonstrate here that small surfactant molecules like SC can also contribute greatly to the steric repulsion, as a result of their high binding affinities to the graphene sheet.

For  $d \leq 2.2$  nm, the onset of sodium counterion-induced steric repulsion[130, 131, 160] between two graphene-SC assemblies further enhances the potential energy barrier (see Figure 3-4-a), a phenomenon that has also been observed in the case of SWCNTs stabilized by SC.[158] In fact, the existence of a concentrated sodium counterion wall for  $d \leq 2.2$  nm is shown in Figure 3-4-b, which illustrates the simulated contour plot of the density profile of the sodium counterions along the z-axis of the simulation box normal to the graphene surface, as a function of  $d$ . For  $d \leq 1.5$  nm, the cholate ions adsorbed on the graphene surfaces begin to establish contact with each other (see Figure 3-4-c for a contour plot of their density profile), which results in direct interactions between them. These interactions lead to the oscillatory behavior of the PMF profile (for  $d \leq 1.5$  nm in Figure 3-4-a), which has been widely recognized to result from the interplay between the van der Waals (vdW) attraction and the hard-core steric repulsion between materials.[132] This oscillatory behavior, reflecting the molecularity of all condensed phases in nature, has been extensively studied experimentally in the case of liquids confined to molecular separations by two approaching smooth mica surfaces.[133-135]

Although the cholate ions adsorbed on the graphene surfaces begin to contact each other at  $d \leq$

1.5 nm, the partially-covered graphene surfaces allow the cholate ions to exchange between them to efficiently cover the empty areas on both surfaces (the merging of the two green bands in Figure 3-4-c) without incurring steric penalties (from  $d = 1.2$  to 1.05 nm in Figure 3-4-a). The density of the cholate ions in the intersheet gap increases from  $d = 1.2$  to 1.05 nm (from green to orange in Figure 3-4-c). As the intersheet separation decreases from 1.05 to 0.9 nm, the density of the cholate ions in the intersheet gap further increases (from orange to red in Figure 3-4-c), and as a result, a single layer of cholate ions is confined and exerts a strong steric repulsive force between the two graphene sheets (from  $d = 1.05$  to 0.9 nm in Figure 3-4-a). Accordingly, the simulated oscillatory PMF profile as the intersheet separation decreases can be rationalized as follows: (i) the cholate ions begin to contact each other and exchange between the two graphene surfaces from  $d = 1.5$  to 1.2 nm, (ii) the intersheet gap begins to accommodate only a single layer of cholate ions from  $d = 1.2$  to 1.05 nm, (iii) the two graphene sheets begin to compress the single layer of cholate ions for  $d \leq 1.05$  nm. Note that in Figure 3-4-c, the density of the cholate ions on the outer surface of the bilayer graphene-SC assembly (the left-most and the right-most bands) increases (from green to orange) slightly for  $d \leq 1.5$  nm, which suggests that some of the cholate ions, originally confined between the two sheets, desorb from (or are squeezed out of) the intersheet gap and then re-adsorb onto the outer surface.

### 3.3.4 Metastable Bilayer Graphene and the Turbostratic Layering Structure

Most interestingly, as a result of the local energy minimum at  $d = 1.05$  nm (see Figure 3-4-a), the bilayer graphene-SC assembly, featuring a single layer of cholate ions and a sodium-ion wall confined between the two graphene sheets (see Figure 3-5-a), is metastable in the aqueous solution. Note that my proposed “sandwich-like” bilayer graphene structure is referred to as “metastable” because the most stable structure of bilayer graphene should occur when the two graphene sheets contact each other directly. As reported in other simulation studies,[156, 163] the two graphene sheets establish the global energy minimum at  $d = 0.35$  nm, resulting from the balance between the intersheet vdW attractions and steric repulsions. A more detailed



characterization of the bilayer graphene structure shown in Figure 3-5-a can be obtained by examining the simulated density profile of the cholate ions and the sodium counterions around two graphene sheets at the local energy minimum where  $d = 1.05$  nm, as shown in Figure 3-5-b. The high cholate ion and sodium counterion densities at the intersheet gap greatly hinders the aggregation of the two graphene sheets by counterbalancing the intersheet vdW attraction with the SC-induced steric repulsion. When such steric repulsion precisely counterbalances the intersheet vdW attraction, the two graphene sheets are locked in the normal direction. Moreover, due to the relatively short-ranged vdW attraction between two graphene sheets (we recently showed that it decays to almost zero when  $d > 1.0$  nm, see Figure 2 of Ref. [156]), at  $d = 1.05$  nm, the two graphene sheets should be able to translate freely parallel to each other. As a result, the layering structure of the two parallel graphene sheets is turbostratic even before they are able to re-aggregate to form AB-stacked bilayers by completely squeezing out the confined cholate ions and sodium counterions. The local minimum in the PMF profile induced by the confined solvent molecules was also observed in the case of liquid-phase-exfoliated graphene in polar solvents, as shown in my recent simulation study.[156] However, the difference between the two cases may be summarized as follows: (i) in the polar solvent case, the steric repulsion is induced by the last confined layer of solvent molecules before desorption from the intersheet gap, due to the stronger affinity between the solvent molecules and graphene, (ii) in the surfactant case, the steric repulsion is induced by the last confined layer of cholate ions and sodium counterions, rather than by the solvent (water) molecules, due to that fact that water molecules do not have strong affinity for graphene, while the cholate ions do. In addition, the positively-charged sodium counterions are able to associate electrostatically with the negatively-charged cholate ions.

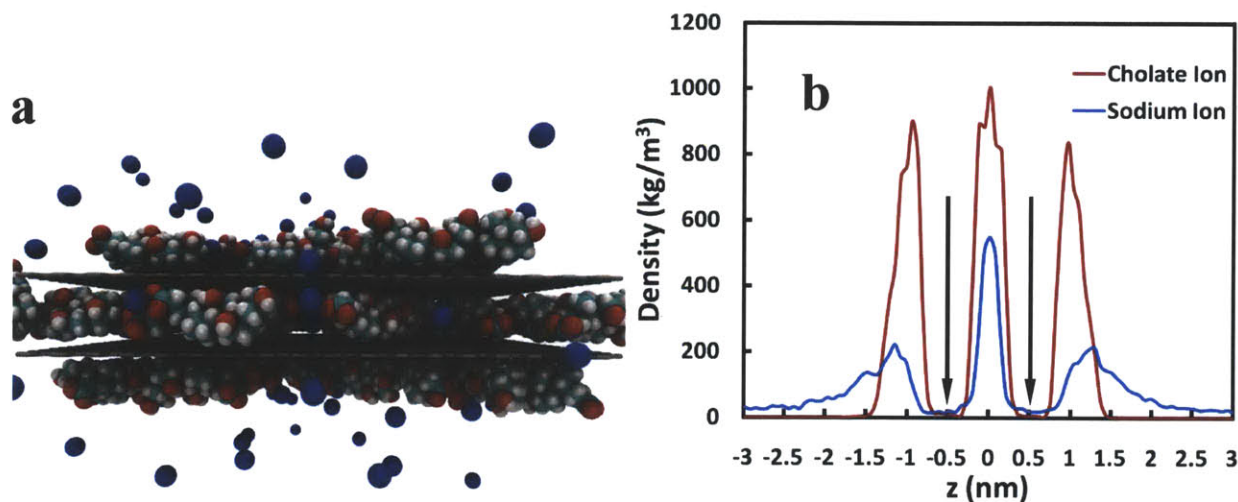


**Figure 3-5:** (a) Post-equilibrium simulation snapshot of the metastable bilayer graphene-SC assembly at an intersheet separation of  $d = 1.05$  nm, showing a single layer of cholate ions and a sodium counterion wall confined between the two graphene sheets. Water molecules are not shown for clarity. The color code is the same as in Figure 3-1. (b) The simulated density profiles of the cholate ions and the sodium counterions along the  $z$ -axis, showing a single layer of cholate ions and a sodium counterion wall (both peaked at  $z = 0$  nm) being confined between the two graphene sheets located at  $d = 1.05$  nm (or at  $z = \pm 0.525$  nm, as pointed out by the two arrows). Note that the other four peaks (two peaked at  $z = \pm 0.9$  nm and two peaked at  $z = \pm 1.5$  nm) show the adsorbed cholate ions and sodium counterions at the outer surfaces of the two graphene sheets.

For multilayer graphene, the Bernal AB-stacking found in natural graphite is the most energetically favorable structure. Nevertheless, turbostratic non-AB stacking graphene sheets have been observed in solution-phase samples after DGU.[40] Here, I found that the existence of a single layer of confined cholate ions and sodium counterions not only efficiently extends the aggregation process as mentioned earlier, but also greatly disorders the AB stacking structure of the multilayer graphene sheets. Specifically, I observe that the surfactant, or the polar solvent, acts like a double-edged sword: it prevents the re-aggregation of both monolayer and multilayer graphene sheets, but it also prevents the re-aggregation of two monolayer graphene sheets into one bilayer graphene sheet (as well as into AB-stacked bilayer graphene). When the surfactants or the polar solvents eventually completely desorb from the intersheet gaps, one would expect that the original bilayer graphene has already re-aggregated with other graphene sheets to form much thicker multilayer graphene sheets (although they have become AB-stacked, they are too

thick for practical applications). In other words, surfactants or polar solvents are not able to selectively stabilize monolayer, bilayer, or trilayer graphene sheets when they form initially as part of the exfoliation process (see Section 3.5 for additional discussion). Therefore, I may conclude that the simulated metastable bilayer graphene structure can explain well the experimental observation of large populations of non-AB stacked bilayer and trilayer graphene.[40] My explanation is also consistent with the experimental speculations that this source of disorder may be induced during strong horn ultrasonication, as well from re-aggregation of previously exfoliated graphene sheets covered with surfactants.[40]

To further confirm the proposed metastable bilayer graphene structure, I calculated the density for the bilayer graphene-SC assembly at  $d = 1.05$  nm (see Figure 3-5-a). Based on the method (Eq. (3-3)) discussed in Section 3.1 for monolayer graphene, the calculated density for the bilayer graphene-SC assembly is equal to 1.25 g/mL, consistent with the buoyant density of bilayer graphene measured experimentally (1.23 g/mL).[40] This further suggests that: (i) the bilayer graphene dispersions obtained by Green et al. using the DGU method may be composed of the metastable, “sandwich-like” graphene proposed here, and (ii) DGU may not be a viable approach to exfoliate graphite to yield AB-stacked graphene, probably due to the long-time centrifugation which concentrates graphene near the isopycnic point such that the re-aggregation is accelerated.

### 3.3.5 Experimental and Predicted Total Graphene Dispersion Stability

As shown in Figure 3-6-a, the correlation between the graphene total mass concentrations and the optical absorbance per unit path length ( $A/l$ ) was calibrated based on the Lambert-Beer law ( $A = \alpha C_0 l$ ). The linear regression yielded  $\alpha = 0.71$  L/mg·m ( $\pm 0.03$  L/mg·m from the mean square error of the regression). The time-dependent graphene total mass concentration,  $C(t)$ , monitored based on the solution optical absorbance, is shown in Figure 3-6-b. The concentration decreases from an initial value of around 31 mg/L to a relatively stable value of around 11 mg/L within a week. The concentration vs. time profile in Figure 3-6-b exhibits an exponential decay, similar to

that observed in the case of graphene exfoliated in polar organic solvents,[137] with a loss of around 65% in the graphene concentration. The initial graphene layer number distribution is shown in Figure 3-6-d (the blue line at day zero), exhibiting a bilayer-enriched graphene solution. To connect the initial graphene layer number distribution to the initial graphene number concentrations,  $N_{i0}$ , I took into account the initial graphene total mass concentration ( $C_0 = 31$  mg/L) and assumed that all the graphene sheets have the same area of  $1 \mu\text{m}^2$ , which corresponds to the average value observed by transmission electron microscopy (TEM). Therefore, the weight of monolayer graphene ( $4.7 \times 10^5$  mg/mol) could be obtained. Subsequently, the weight of other multilayer graphene could be obtained by multiplying the weight of monolayer graphene by the layer numbers.

The MD simulation results presented so far have provided a thermodynamic description of the dispersion stability of solution-phase exfoliated graphene. However, for practical purposes, the aggregation kinetics of graphene must be investigated to quantify the life time and the quality of these dispersions. Recently, I developed a theoretical model that combines the PMF results from MD simulations with the theory of slow colloid coagulation.[123, 156] In my study of graphene dispersions in organic polar solvents, this model was used to correlate the simulated PMF results[156] with the time-dependent graphene layer number distribution observed in actual experiments.[137] In the present study of SC-stabilized graphene dispersions, I generalize this model to correlate the simulated PMF results with the time-dependent graphene concentration observed in our experiments. The kinetic theory of graphene aggregation is discussed in detail in Appendix C.

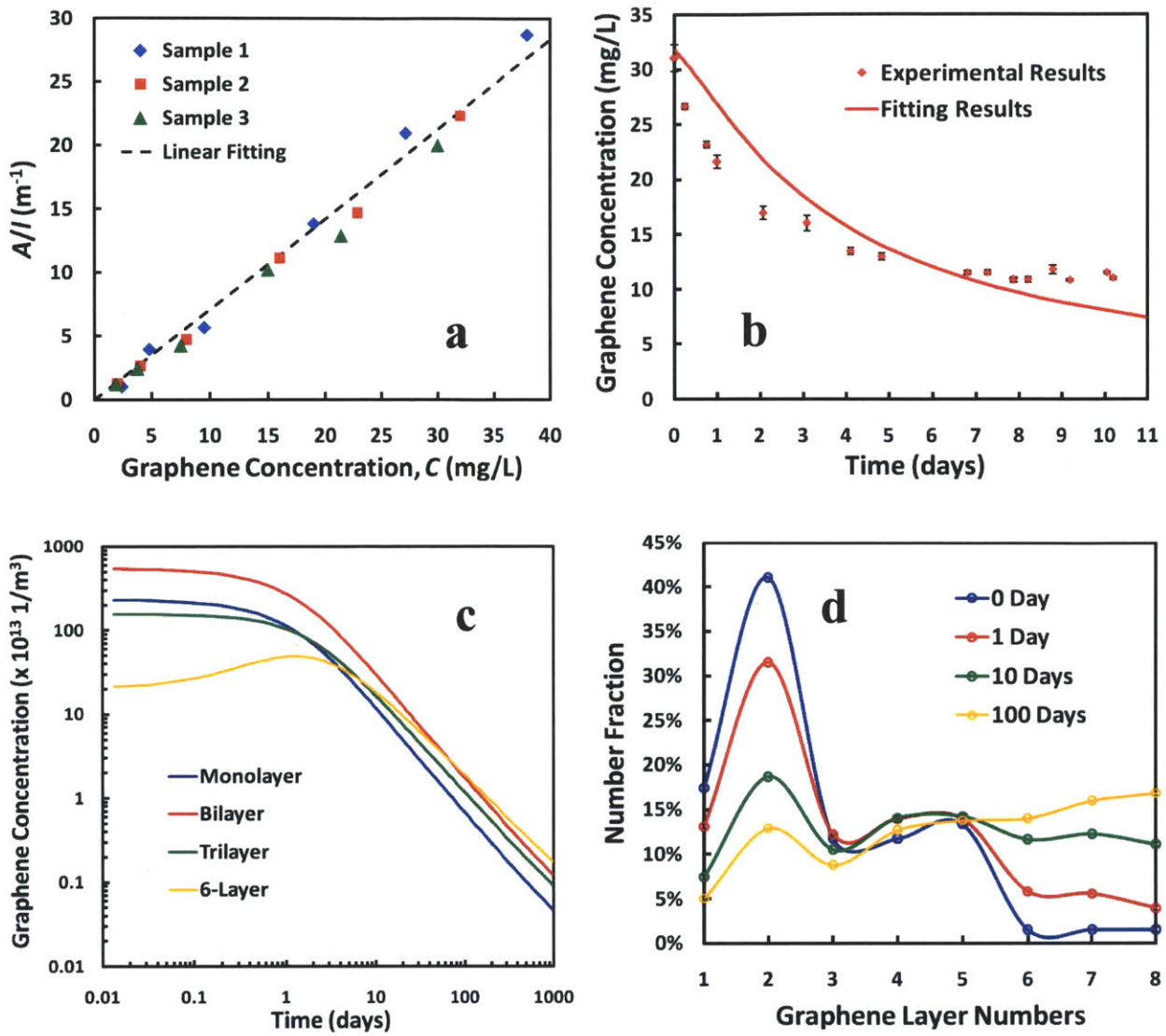


**Figure 3-6:** (a) Measured optical absorbance (at 660 nm wavelength) per unit path length ( $A/l$ ) as a function of the total graphene mass concentration,  $C$ . Note that three different samples (corresponding to the red, blue, and green symbols) were prepared using the same procedure. (b) Time-dependent graphene total mass concentration,  $C(t)$ , as a function of time. The red line denotes the numerical fitting results from Eqs. (3-A1)–(3-A6) in Appendix C. The errors in the experimental results (the black markers) were obtained from the standard deviations in the optical absorbance of the three cuvette samples. (c) Predicted time-dependent number concentrations of graphene with various layer numbers,  $N_i(t)$ , as a function of time. Note that 6-layer graphene is used to represent thicker multilayer graphene. (d) Predicted distributions of graphene layer numbers as a function of time. Note that the circles are the actual values, and each line that smoothly connects the circles is just a guide to the eye.

In order to utilize the kinetic model described above to calculate the time-dependent number concentration of various graphene layer types,  $N_i(t)$ , it is first necessary to estimate the value of  $A_C$ . The collision area,  $A_C$ , can be obtained by least-square fitting the predicted time-dependent graphene total number concentration,  $N_{total}(t)$ , to the measured graphene total mass concentration,  $C(t)$ . Specifically,  $N_{total}(t)$  can be calculated as the sum over the time-dependent concentrations of all the  $i$ -layer graphene sheets, that is,

$$N_{total}(t) = \sum_{i=1}^M N_i(t) \quad (3-7)$$

We can relate the various components of  $N_{total}(t)$  (in  $1/m^3$ ) with  $C(t)$  (in mg/L) using the assumption that all the graphene sheets have the same area of  $1 \mu m^2$ . The nonlinear minimization algorithm for the least-squares fitting was carried out utilizing the interior-reflective Newton method subroutine in the MATLAB numerical library. After incorporating Eq. (3-7) into Eqs. (3-A1)–(3-A6) in Appendix C, as shown in the fitting curve in Figure 3-6-b, I deduced the best-fit average collision area,  $A_C = 1.57 \text{ nm}^2$ , and the rate constant of aggregation,  $k = 7.54 \times 10^{-22} \text{ m}^3/\text{s}$ . The total least-square error of the fitting is  $173.2 \text{ mg}^2/\text{L}^2$ , which corresponds to a significant error of 3.2 mg/L (around 10%, for an initial concentration of 31 mg/L and of 30% of a steady-state concentration of 11 mg/L) for each fitted concentration value, using solely the single fitted parameter,  $A_C$ . A more complex model with additional fitting parameters is probably required to replace this error, but is outside the scope of this project.

Next, using the deduced  $A_C$  value of  $1.57 \text{ nm}^2$ , I predict the time-dependent graphene number concentration of various layer types, as shown in Figure 3-6-c. Using a similar procedure, I predicted the time-dependent graphene layer number distributions in Figure 3-6-d. In Figure 3-6-c, all the monolayer, bilayer, and trilayer graphene concentrations decrease with time in an exponential manner. If one defines the lifetime of solution-phase graphene as the time required for the concentration of monolayer or bilayer graphene sheets to be reduced by  $1/e$ , the lifetime of graphene is only about 1 day. However, in the case of trilayer graphene, the lifetime is about 2 days, as a result of having both monolayer and bilayer graphene as sources. Moreover, in the

case of thicker multilayer graphene, such as 6-layer graphene, its number concentration actually increases to a maximum in about 2 days and then decreases, with a lifetime which is longer than 10 days (see Figure 3-6-c). This behavior results primarily from the re-aggregation of monolayer and thinner multilayer graphene, which in general shifts the layer number distribution in the direction of thicker layers as time evolves, as shown in Figure 3-6-d. Although the number concentration of bilayer graphene decreases by 1/e in about 1 day (see Figure 3-6-c), its layer number distribution is still higher (18%) compared to other layer types up to 10 days (see Figure 3-6-d), which may be attributed to the initial bilayer-enriched graphene solution from Stage-2 GICs.

### **3.3.6 AB-Stacked and Turbostratic Graphene Dispersion Stability**

As discussed in Section 3.4, for the SC-stabilized graphene dispersions considered here, the re-aggregated graphene tends to be turbostratic with one additional SC monolayer sandwiched between the two graphene sheets. As a result, the re-aggregated graphene sheets are intrinsically different from the as-prepared AB-stacked graphene. It then follows that each layer-number type graphene should consist of multiple subtypes of graphene, including the as-prepared AB-stacked species and various turbostratic species generated after the dispersion is prepared (considering all possible collisions). For example, as shown schematically in Figure 3-7-a, there is only one subtype of turbostratic bilayer graphene which is generated from the re-aggregation of two monolayer graphene. On the other hand, there are two subtypes of turbostratic trilayer graphene which are generated from the re-aggregation of one monolayer graphene and one AB-stacked bilayer graphene (denoted as type I), and from the re-aggregation of one monolayer graphene and one turbostratic bilayer graphene (denoted as type II). For other thicker turbostratic  $m$ -layer graphene, there are even more possible subtypes, but here, I will only focus on bilayer and trilayer graphene since they are the most important graphene types for practical applications.



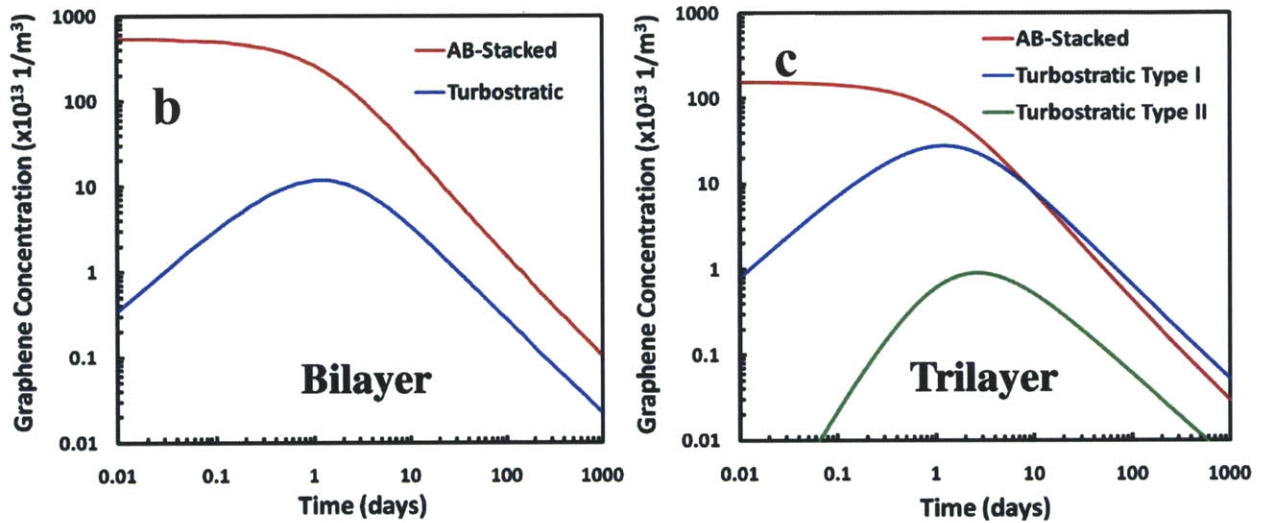
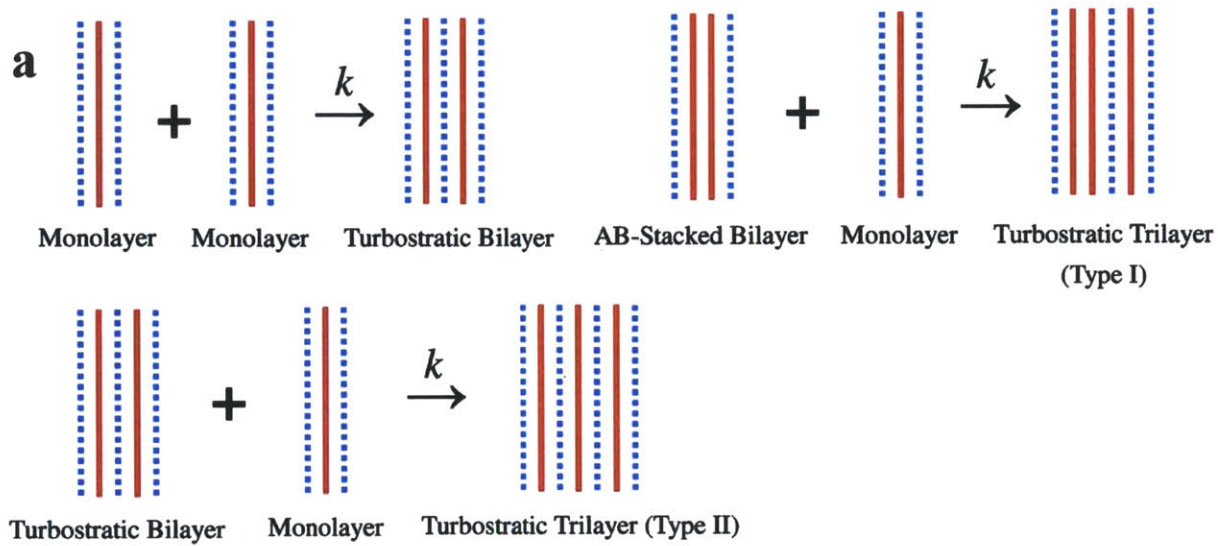


**Figure 3-7:** (a) Re-aggregation mechanisms of turbostratic bilayer and trilayer graphene. The turbostratic bilayer graphene results from the re-aggregation of two monolayer graphene sheets. The turbostratic trilayer graphene results from the re-aggregation of one AB-stacked bilayer graphene and one monolayer graphene (type I), or from the re-aggregation of one turbostratic bilayer graphene and one monolayer graphene (type II). (b) Predicted time-dependent concentrations of AB-stacked bilayer graphene (red line) and turbostratic bilayer graphene (blue line). (c) Predicted time-dependent concentrations of AB-stacked trilayer graphene (red line) and turbostratic trilayer graphene (type I — blue line, and type II — green line).

In order to obtain the time-dependent AB-stacked bilayer and trilayer graphene number concentrations, I can decompose  $N_2(t)$  and  $N_3(t)$  as follows:

$$N_2(t) = N_{2,AB}(t) + N_{2,turbo}(t) \quad (3-8)$$

$$N_3(t) = N_{3,AB}(t) + N_{3,turbo}^I(t) + N_{3,turbo}^{II}(t) \quad (3-9)$$

where the additional subscripts “AB” and “turbo” denote AB-stacked and turbostratic graphene, respectively, and the superscripts “I” and “II” denote type I and type II trilayer graphene, respectively. Specifically, the reaction kinetics of the generations of bilayer and trilayer graphene subtypes can be modeled as follows:

$$\frac{dN_{2,AB}(t)}{dt} = -\sum_{i=1}^M kN_{2,AB}(t)N_i(t) \quad (3-10)$$

$$\frac{dN_{2,turbo}(t)}{dt} = kN_1(t)N_1(t) - \sum_{i=1}^M kN_{2,turbo}(t)N_i(t) \quad (3-11)$$

$$\frac{dN_{3,AB}(t)}{dt} = -\sum_{i=1}^M kN_{3,AB}(t)N_i(t) \quad (3-12)$$

$$\frac{dN_{3,turbo}^I(t)}{dt} = kN_1(t)N_{2,AB}(t) - \sum_{i=1}^M kN_{3,turbo}^I(t)N_i(t) \quad (3-13)$$

$$\frac{dN_{3,turbo}^{II}(t)}{dt} = kN_1(t)N_{2,turbo}(t) - \sum_{i=1}^M kN_{3,turbo}^{II}(t)N_i(t) \quad (3-14)$$

By combining Eqs. (3-8)–(3-14) with the predicted reaction rate,  $k = 7.54 \times 10^{-22}$  m<sup>3</sup>/s, obtained in Section 3.5, one can calculate the time-dependent number concentrations of various subtypes of bilayer and trilayer graphene, as shown in Figures 3-7-b and 3-7-c, respectively. In the case of bilayer graphene (see Figure 3-7-b),  $N_{2,turbo}(t)$  increases with time due to the re-aggregation of two monolayer graphene, and then reaches a maximum in about 1 day due to the lack of source monolayer graphene, which has almost completely re-aggregated with all the other species (consistent with the life time of 1 day for monolayer graphene, as discussed in Section 3.5). Nevertheless, the proportion of the turbostratic bilayer graphene is significantly smaller than that of the AB-stacked graphene within 1 day (at least by a factor of 20). While the proportion of

turbostratic bilayer graphene becomes comparable to that of the AB-stacked graphene after 10 days, it is still smaller by a factor of 4. As a result  $N_{2,AB}(t) \approx N_2(t)$  for freshly-prepared bilayer graphene samples, and I conclude that the majority of the bilayer graphene in the solution is AB-stacked soon after preparation. In addition, I conclude that  $N_{2,AB}(t) \approx 80\% N_2(t)$  after 10 days of preparation.

Similarly, as shown in Figure 3-7-c, in the case of trilayer graphene, the concentrations of the two turbostratic subtypes,  $N_{3,turbo}^I(t)$  and  $N_{3,turbo}^{II}(t)$ , increase with time due to the re-aggregation of monolayer graphene and bilayer graphene (AB-stacked ones for type I and turbostratic ones for type II), and then reach maxima in about 2 days (for type I) and 3 days (for type II), respectively. However, note that the proportion of the type II trilayer graphene is much smaller than that of the type I species (at least by a factor of 5), as a result of the negligible proportion of its source (turbostratic bilayer graphene) compared to that of the type I species (AB-stacked bilayer graphene). In addition, contrary to the bilayer case in which the AB-stacked species always dominates the total composition,  $N_{3,turbo}^I(t)$  exceeds  $N_{3,AB}(t)$  by a small amount (less than a factor of 2) in about 10 days, enriching the total trilayer graphene dispersion in both AB-stacked and turbostratic species. This could probably be attributed to the high starting AB-stacked bilayer graphene composition of the dispersion after preparation.

### 3.4 Conclusions

I successfully combined molecular simulations, theoretical modeling, and experimental measurements to elucidate several important aspects of solution-phase exfoliated graphene aqueous dispersions. I probed experimentally and theoretically the surface coverage and electrostatic potential around a monolayer graphene-SC assembly, which exhibits a compact adsorbed monolayer of cholate ions surrounded by screening sodium counterions and ordered water molecules. The graphene surface is only partially covered by the cholate ions (~60%), leaving many available reaction sites for potential reactants for functionalization. However, it is

important to keep in mind that the graphene surface covered by charged surfactants may facilitate the adsorption of oppositely-charged reactants present in the solution.[73] As a result, the impact of the graphene surface charge resulting from surfactant adsorption is also an important factor in determining the functionalization selectivity, in addition to the surface coverage. In addition, specific binding (e.g., hydrophobic bonding, hydrogen bonding, or ring stacking) between surfactants adsorbed on the graphene surface and reactants should be taken into consideration.

From the potential of mean force (PMF) calculation for two parallel graphene-SC assemblies, I found that the traditional electrostatic interaction is not the dominant contribution to the repulsive energy barrier that inhibits graphene re-aggregation. Indeed, the dominant contribution is the steric hindrance induced by the last layer of cholate ions and sodium counterions confined between the two graphene sheets. Such bilayer graphene configuration corresponds to a local minimum in the PMF profile, which defines a surfactant-stabilized metastable structure for exfoliated multilayer graphene sheets. Such a metastable structure can explain experimental observations of turbostratic, non-AB stacked graphene.[40] When using surfactants to disperse and stabilize graphene in aqueous media, one faces the following dilemma: on the one hand, surfactants can certainly stabilize graphene dispersions, but on the other hand, they prevent the formation of new AB-stacked bilayer and trilayer graphene resulting from the re-aggregation process. Therefore, a possible route to obtain AB-stacked bilayer- or trilayer-enriched graphene is to pre-treat the raw graphite material to establish the corresponding layering of the graphite sheets. Indeed, our recent attempt to produce bilayer- and trilayer-enriched graphene dispersions using Stage-2 GICs addresses this issue nicely.[152]

By combining the PMF results with a kinetic model of colloid aggregation, I predicted the time-dependent concentration and distribution of graphene with various layer numbers, and I further decomposed each layer type into subtypes including the AB-stacked species and various turbostratic species. This theoretical model can be very useful in estimating the lifetime of graphene dispersions. In particular, the concentrations of AB-stacked bilayer and trilayer

graphene define the quality of the graphene dispersion for electronic and optical applications. Furthermore, the lifetime of monolayer graphene also influences the success of using functionalization to open their bandgaps. In general, monolayer, bilayer, and trilayer graphene are easily degradable as time evolves compared to thicker multilayer graphene, and therefore, the subsequent substrate-transferring or functionalization processes should be carried out using very fresh samples to increase the yields of electronic and optical graphene devices. My findings provide fundamental insights into the manufacturing of useful graphene-based electronic and optical devices using either functionalized monolayer graphene by controlling their surface morphology before reaction, or AB-stacked multilayer graphene by controlling their layer thickness before exfoliation. Future computational work may be carried out for other effective dispersants, including surfactants (e.g., SDS, SDBS, Triton X100, and CTAB)[165] and polymers (e.g., biocompatible block copolymers).[166]

### 3.5 Appendix A: Supporting Tables and Figures

**Table 3-A1: Summary of Simulated Systems**

<b>System</b>	<b>Number of Graphene Sheets</b>	<b>Number of SC Molecules</b>	<b>Number of Water Molecules</b>	<b>Total Number of Atoms</b>	<b>Simulation Box Size <sup>c</sup> (nm<sup>3</sup>)</b>	<b>Simulation Time (ns)</b>
1 <sup>a</sup>	1	56	10,981	38,967	7.38 x 7.67 x 6.69	300 ns
2-52 <sup>b</sup>	2	112	14,000	54,048	8.74 x 8.74 x 6.80	20 ns each

<sup>a</sup> Sodium cholate adsorption and surface self-assembly simulations on a graphene monolayer.

<sup>b</sup> Potential of mean force (PMF) simulations at 51 intersheet separations between two parallel graphene-SC assemblies.

<sup>c</sup> Averaged over the production run of the simulation with small fluctuations from the pressure coupling.

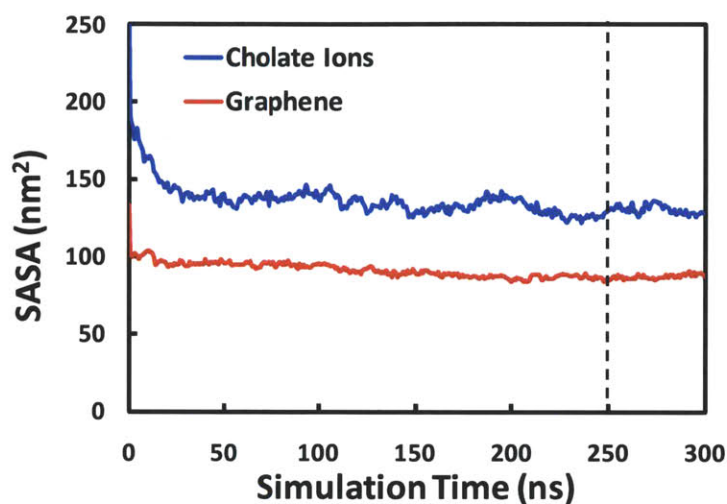


**Figure 3-A1:** Solvent accessible surface areas (SASAs) of a graphene monolayer and the cholates ions, monitored as a function of simulation time. As shown, the fluctuations in the SASA curves are significant at the beginning, and are dampened after about 200 ns, indicating that the system has reached equilibrium. Therefore, data analysis was performed during the last 50 ns of the entire simulation run, as indicated by the time period beyond the vertical dashed line.

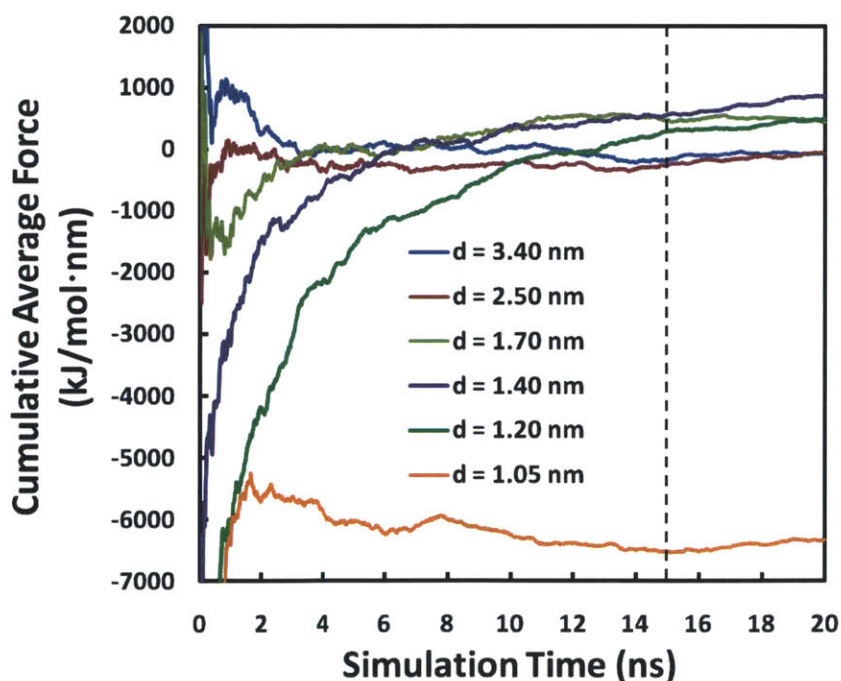


**Figure 3-A2:** Cumulative average forces as a function of simulation time at several selected inter-sheet separations,  $d$ . As shown, the fluctuations in the force curves are significant at the beginning, and are dampened after about 10 ns, indicating that the system has reached equilibrium. Therefore, data analysis was performed during the last 5 ns of each simulation run, as indicated by the time period beyond the vertical dashed line.

### 3.6 Appendix B: Summary of Experimental Procedures

Briefly, the bilayer-enriched graphene dispersion in aqueous SC solutions was prepared using Stage-2 GICs, as demonstrated in our recent report.[152] HOPG was chosen as a high-quality graphite source, and I used the halogen intercalant ICl to form Stage-2 ionic GIC. In this scheme, Stage-2 GICs have every 2nd layer of the graphite lattice intercalated. The Stage-2 GICs were first treated to yield expanded graphite (EG) by removing the ICl intercalant during the “thermal shock”. The foam-like EG was then immersed in 2 wt% SC aqueous solutions and subjected to slow homogenization (6,800 rpm, 30 minutes), mild sonication (40 kHz, 10 minutes), and centrifugation (2,000 rpm, 805 g, 20 minutes) to yield clear and grey dispersions. In order to locate and isolate large flakes from poly-disperse graphene solutions for further characterization, an on-chip separation method based on size utilizing the “coffee-ring effect” was used.[167] Using this method, the graphene flakes are separated based on the lateral size but independently of their thickness on a SiO<sub>2</sub>-Si substrate. Raman spectroscopy was used to characterize the isolated graphene flakes deposited on the substrate. The 2D peak corresponding to specific numbers of stacked layers in our exfoliated graphene flakes exhibits the same layering dependence as that observed in micromechanically-cleaved graphene on the same substrate,[168] indicating that the solution processed graphene flakes are AB-stacked.[152] Systematic statistical analysis of the initial thickness (or layer number) distributions for large graphene flakes was carried out using a combination of optical microscopy and Raman spectroscopy.

The Lambert-Beer plot of graphene-SC solutions was calibrated using graphite flakes as raw materials (see Figure 3-6-a). Graphene solutions were prepared by adding 1.5 g of natural graphite flakes (Sigma-Aldrich 332461) to 150 mL of 20 mg/mL sodium cholate aqueous solution in a 200 mL capped round-bottomed flask. Sonication was carried out in a sonication bath (VWR Aquasonic model 50D) for 30 minutes. After sonication, the sample was extracted from the flask into three centrifuge tubes (Falcon 50 mL polypropylene conical tubes), and left to stand overnight to allow thick graphite flakes to sediment out of the solution. The samples were then centrifuged for 30 minutes at 4000 rpm (990 g) in a Hettich Universal 320 centrifuge. After



centrifugation, the top half of the dispersion was extracted by vacuum pipette (~8 mL) and retained for use. A 10 mL of the graphene solution was diluted sequentially with the 20 mg/mL SC solution to obtain solutions at 6 different graphene concentrations. The original and the diluted solutions were decanted into 6 quartz cuvettes, and the optical absorbance was measured using a UV/visible spectrophotometer (Beckman Coulter DU800).

The graphene concentration of the original solution was obtained by vacuum filtering the solution (50 – 65 mL) through three layers of Millipore nitrocellulose membranes (~0.45  $\mu\text{m}$  pore size and 0.47 mm membrane diameter). After filtration, the membranes were rinsed with 100 mL Milli-Q water for ten times to get rid of the residue surfactants, and subsequently dried under room temperature overnight. The weight of the membranes before and after filtration was measured using a microbalance.

### 3.7 Appendix C: Kinetic Theory of Graphene Aggregation

To utilize the simulated PMF curve (see Figure 3-4-a) in the theoretical model, the first step involves fitting the PMF curve to a semi-empirical analytical model. To capture the primary features of the PMF curve, I propose the following model to describe the PMF per unit area,  $\Phi$ , between two parallel graphene sheets with an intersheet separation,  $d$ :

$$\Phi(d) = \varepsilon \left[ \left( \frac{r_0}{d} \right)^{12} - 2 \left( \frac{r_0}{d} \right)^6 \right] + \beta_1 \exp \left[ - \frac{(d-r_1)^2}{2\sigma_1^2} \right] + \beta_2 \exp \left[ - \frac{(d-r_2)^2}{2\sigma_2^2} \right] + \alpha \exp[-\kappa(d-r_3)] \quad (3-A1)$$

where  $\varepsilon$  and  $r_0$  are the well-known parameters in the Lennard-Jones (LJ) potential that characterize the depth and location, respectively, of the metastable energy well;  $\beta_1$ ,  $r_1$ , and  $\sigma_1$  characterize the height, location, and width, respectively, of the primary energy barrier;  $\beta_2$ ,  $r_2$ , and  $\sigma_2$  characterize the height, location, and width, respectively, of the small, secondary energy barrier; and  $\alpha$ ,  $\kappa$ , and  $r_3$  characterize the magnitude, decay rate, and location of the long-range repulsive electrostatic potential between the two SC-covered graphene sheets (see Figure 3-4-a). Note that to account for the electrostatic interactions present in the case of SC-covered graphene

dispersions considered here, I modified Eq. (3-1) of Ref.,[156] which results in Eq. (3-A1) used here. The parameters in Eq. (3-A1) were obtained by least-square fitting of Eq. (3-A1) to the simulated PMF curve in Figure 3-4-a, and are summarized in Table 3-A2.

**Table 3-A2:** Summary of Fitted Parameters in Eq. (3-A1). Note that  $\varepsilon$ ,  $\beta_1$ ,  $\beta_2$ , and  $\alpha$  are in units of  $\text{kJ/mol}\cdot\text{nm}^2$ ,  $r_0$ ,  $r_1$ ,  $\sigma_1$ ,  $r_2$ ,  $\sigma_2$ , and  $r_3$  are in units of nm, and  $\kappa$  is in units of  $\text{nm}^{-1}$

$\varepsilon$	$r_0$	$\beta_1$	$r_1$	$\sigma_1$	$\beta_2$	$r_2$	$\sigma_2$	$\alpha$	$\kappa$	$r_3$
46.27	1.05	16.77	1.20	0.10	4.23	1.46	0.08	13.29	2.74	1.43

Our kinetic model considers individually-suspended graphene sheets in a solution media, and makes the following assumptions:[156] (i) the aggregation process is diffusion controlled, (ii) since the graphene sheets can translate freely, they are modeled as effective spheres, (iii) the lateral size of all graphene sheets is the same, (iv) the estimated diffusivity of graphene sheets,  $D = 10^{-12} \text{ m}^2/\text{s}$ , is independent of its layer number,  $i$ , since the friction factor in the Stokes-Einstein relation depends primarily on the lateral size of a graphene sheet,[31] (v) the graphene sheets aggregate and precipitate when the number of stacking layers exceeds the maximum number of graphene sheet layers which exist in a solution phase stably,  $M = 10$ ,[156] and (vi) due to the relatively negligible thickness of the graphene sheets, the intersheet interaction potential energy is assumed to be independent of the number of layers in the two sheets.

Considering all possible collisions (reaction pairs), the time-dependent number concentration (in  $1/\text{m}^3$ ) of monolayer graphene,  $N_1(t)$ , as a function of time is given by the following consumption term:[156]

$$\frac{dN_1(t)}{dt} = -\sum_{i=1}^M kN_1(t)N_i(t) \quad (3-A2)$$

where  $N_i(t)$  is the time-dependent number concentration of  $i$ -layer graphene, and  $k$  is the reaction rate constant (i.e., the rate constant of aggregation in the present study). Similarly, the time-dependent number concentration of bilayer graphene,  $N_2(t)$ , is modeled as the sum of the source and consumption terms. Specifically,

$$\frac{dN_2(t)}{dt} = kN_1(t)N_1(t) - \sum_{i=1}^M kN_2(t)N_i(t) \quad (3-A3)$$

More generally, beginning with trilayer graphene, the time-dependent number concentration of  $m$ -layer graphene,  $N_m(t)$  ( $3 \leq m \leq M$ ), is modeled as the sum of the relevant source and consumption terms. Specifically,

$$\frac{dN_m(t)}{dt} = \frac{1}{2} \sum_{i=1}^{m-1} kN_i(t)N_{m-i}(t) - \sum_{i=1}^M kN_i(t)N_m(t) \quad (3-A4)$$

where the factor of 1/2 avoids counting the same collision twice in the source term. The rate constant of aggregation,  $k$ , can be expressed as follows:[156]

$$k = \frac{8\pi D}{\int_{r_0}^{\infty} \frac{\exp[V(r)/k_B T]}{r^2} dr} \quad (3-A5)$$

where  $r$  is the effective distance between two graphene sheets,  $r_0 = 1.05$  nm is the distance of closest approach at the metastable state, and  $V(r)$  is the intersheet interaction potential energy (see below). It is noteworthy that when two graphene sheets approach, all collision angles and areas are possible. Irrespectively of the collision angle, the graphene sheets need to overcome the dominant energy barrier resulting from the last layer of confined molecules which includes cholate ions and sodium counterions, as discussed in Section 3.4. Therefore, the ensemble average of all collision angles can be viewed as an effective face-to-face collision that I have considered in my analysis, where the radial coordinate,  $r$ , corresponds to the intersheet separation,  $d$ , in the MD simulations. Consequently, the intersheet interaction potential energy,  $V(d)$ , was further simplified as follows:

$$V(d) = \Phi(d) \times A_C \quad (3-A6)$$

where  $\Phi(d)$  is the PMF between two parallel graphene sheets per unit area obtained utilizing the MD simulations (see Figure 3-4-a), and  $A_C$  is the average collision area, which is the *single adjustable parameter* in the kinetic model. For given values of the parameter,  $A_C$ , and the initial number concentrations of the various graphene layer types,  $N_{i0}$ , the time-dependent number

concentration of various graphene layer types,  $N_i(t)$ , can be obtained by simultaneously solving Eqs. (3-A1)–(3-A6) numerically.

## Chapter 4

# Molecular Perspective on Diazonium Adsorption for Controllable Functionalization of Single-Walled Carbon Nanotubes in Aqueous Surfactant Solutions

### 4.1 Introduction

In Chapter 2, I discussed the role of surfactants in dispersing SWCNTs in aqueous solutions. The resulting stable SWCNT-surfactant complexes serve as a unique platform for subsequent chemical functionalization processes which involve the selective adsorption of reagents onto the SWCNT-surfactant complex surface. Selective adsorption of solutes onto a charged solid surface in an aqueous medium is a generic process utilized across industries and technologies,[169-171] which is often difficult to predict and control. Conventional continuum-based theories (e.g., the Langmuir isotherm and the Poisson-Boltzmann equation[31]) neglect the atomic-scale properties of the solute and the surface, and therefore, cannot be used to elucidate and molecularly predict many important adsorption phenomena. Among the properties neglected, surface heterogeneity[172] and surface-charge mobility[32] both contribute to the discrete and dynamic nature of the adsorption process. For example, amorphous silica ( $\text{SiO}_2$ ) substrates present surfaces with high roughness and non-uniformly-distributed charges.[172] In a more complex scenario, ionic surfactant-covered solid surfaces exhibit both surface roughness and charge-mobility, because the surfactant molecules can diffuse freely on the surface while adsorbed.[104, 155, 158, 173] Many solution-phase chemical processes involve the use of surfactants to disperse and decorate solid nanoparticles, including single-walled carbon nanotubes (SWCNTs) as discussed in Section 1.3.[174]

The surface roughness of surfactant-covered SWCNTs results from the molecular “islands” formed by agglomerated surfactant assemblies on the surface.[91, 93, 158] Such a surface is also charge-mobile (in the case of ionic surfactants), since the charged surfactant head groups can move freely on the surface.[91, 158] Studying these features at the molecular level can provide insight into useful methods to control the functionalization of SWCNTs.[175, 176] As mentioned in Section 1.3, there has been a significant recent interest in developing methods to functionalize the nanotube sidewall, such that the nanotube optical and electronic properties can be modified for a variety of applications,[61] ranging from drug-delivery vehicles[62] to molecular sensors.[63, 64] Among various functionalization methods used, reaction with diazonium salts (see Figure 4-1-d) represents a promising route for the covalent modification of the SWCNT.[174] Although this functionalization method involves covalent reaction of the negatively-charged diazonium ion with the neutral  $sp^2$  carbon atoms on the nanotube sidewall, it has been proposed that the step which is selective towards functionalization is the non-covalent adsorption/binding of the diazonium ion on the nanotube surface (see Figure 4-1-e for a schematic of the two-step functionalization process).[90] Recently, I have demonstrated that by decorating the SWCNT with different surfactants (sodium cholate (SC), sodium dodecyl sulfate (SDS), and cetyl trimethyl ammonium bromide (CTAB), see Figures 4-1-a, 4-1-b, and 4-1-c, respectively), one can control the extent of functionalization.[176]

With the above in mind, in the present study, I combined molecular dynamics (MD) simulations, experiments, and equilibrium reaction modeling to understand and model the extent of diazonium functionalization of SWCNTs coated with SC, SDS, and CTAB. A combined simulation-modeling framework is presented that can be used to guide the control of various sensitive experimental conditions needed to achieve the desired extent of SWCNT functionalization.

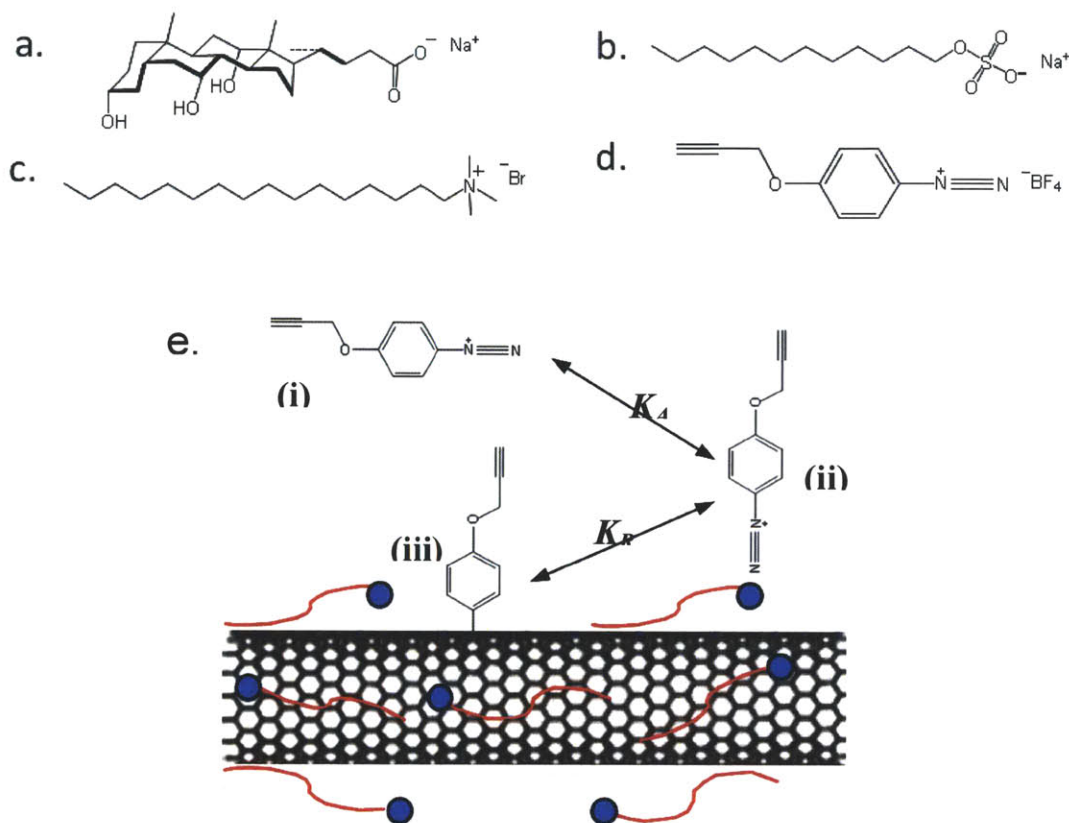


**Figure 4-1:** Chemical structures of the surfactants and the diazonium salt considered in this study: (a) sodium cholate (SC), (b) sodium dodecyl sulfate (SDS), (c) cetyl trimethylammonium bromide (CTAB), and (d) tetrafluoroborate ( $\text{BF}_4^-$ ) aryl diazonium. The bile salt SC has rigid steroidal backbones, which results in hydrophobic and hydrophilic “faces”. Therefore, SC can also be referred to as a “facial” surfactant. The rigidity of the SC molecules leads them to form a monolayer structure on the nanotube surface.[158] The flexible linear surfactants, SDS and CTAB, possess less rigid, hydrophobic chains, which tend to coat the nanotube in a more disordered manner at high surface coverages.[91] (e) Schematic of the equilibrium model proposed here, showing the three possible states of the diazonium ion during the functionalization process: (i) free in the surfactant aqueous solution, (ii) adsorbed on the SWCNT-surfactant complex (with an adsorption constant  $K_A$ ), and (iii) covalently bound to the SWCNT surface (with a reaction constant  $K_R$ ). Adsorbed surfactant molecules are shown as blue beads (the hydrophilic surfactant heads) connected with red lines (the hydrophobic surfactant tails).

## 4.2 Methods

### 4.2.1 Simulation Methods

Molecular dynamics (MD) simulations of diazonium ion adsorption onto the SWCNT-surfactant complex in aqueous solution were carried out using the GROMACS 4.0 software package.[103]



The (6,6) SWCNT was first covered with surfactants (SC, SDS, or CTAB) which were fully dissociated into surfactant ions and counterions ( $\text{Na}^+$  in the case of SC and SDS, and  $\text{Br}^-$  in the case of CTAB). Low and high surfactant surface coverages, having linear packing densities of 2.44 and 5.85 surfactants per nm of the SWCNT, respectively, as utilized in recent simulation studies,[91, 93] were chosen to investigate coverage effects on binding affinities. For comparison, the experimentally estimated linear packing densities of SDS[128], SC[89], and CTAB[176] are  $4.5 \pm 1.0$ ,  $3.6 \pm 1.0$ , and  $10 \pm 1.0$  molecules/nm, respectively. The equilibrated SWCNT-surfactant configurations corresponding to these surface coverages were generated using the same simulation method described in my recent simulation work on the SWCNT-SC assembly, where each simulation ran for more than 100 ns.[158] The simulation parameters used in this study and the force-field parameters for water, the SWCNT, and SC were also drawn from Ref. [158]. Note that a thermostat of 45°C was utilized for all the simulations in order to match the experimental conditions. The alkane tails of SDS and CTAB were modeled using the OPLS-AA force-field,[107] with updated dihedral parameters.[177] The sulfate head of SDS and its connection to the dodecyl tail were modeled following Lopes et al.,[178] while the trimethylammonium head of CTAB and its connection to the cetyl tail were modeled following Lopes and Pádua.[179] Note that the surfactant head-related force-field parameters developed by Pádua and coworkers were specifically developed in a manner that is consistent with the use of the OPLS-AA force field for each surfactant tail.[178, 179]

The tetrafluoroborate anion ( $\text{BF}_4^-$ ) of the aryl diazonium salt was modeled using the force-field parameters in Ref. [178]. The atomic charges of the positively-charged diazonium ion were not previously available in the literature, and were generated using the quantum mechanics (QM) software package, Gaussian 03,[180] together with the CHELPG electrostatic potential-fitting algorithm[181] at the MP2/cc-pVTZ(-f)//HF/6-31G\* level of theory. This level of theory was selected for the purpose of maintaining consistency with the models of Lopes et al.[178, 179, 182] The cc-pVTZ(-f) basis set was adapted from the cc-pVTZ basis set of Dunning,[183] as provided at the Basis Set Exchange,[184, 185] by removing the *d* polarization function from hydrogen and

the  $f$  polarization functions from heavier atoms.[182] All other force-field parameters for the diazonium ion were drawn from the OPLS-AA force field. The computed partial atomic charges of the diazonium ion are summarized in Table 4-A1 in Appendix A.

The interactions between the diazonium ion and the SWCNT-surfactant complex were quantified using the simulated potential of mean force (PMF). The case where no surfactants are present, corresponding to the bare SWCNT in water, was also investigated for comparison. To mimic the infinite dilution of the diazonium salt in the actual experiments, only one diazonium ion was introduced in the simulation cell. The diazonium ion was constrained at various radial positions,  $r$ , relative to the cylindrical axis ( $z$ -axis) of the SWCNT, and allowed to move freely on each concentric cylindrical surface around the nanotube (see Figure 4-3). I also monitored the coordinates of the diazonium ion as a function of simulation time (see Figure 4-A1 in Appendix A), which confirmed that the diazonium ion can move freely along, as well as around, the SWCNT for given  $r$  values. The simulation at each  $r$  value was equilibrated for 40 ns before recording the mean force (averaged over another 20 ns),  $\langle f(r) \rangle$ , that is required to constrain the center of mass (COM) of the diazonium ion at each  $r$  value. Note that the 40 ns equilibration time is necessary to allow the surfactant molecules to diffuse along the SWCNT surface to form local “hot spots” around the diazonium ion when approaching the nanotube (see Section 4.3.2 for details). The PMF, as a function of  $r$ , was obtained by numerically integrating  $\langle f(r) \rangle$  along  $r$ . Specifically,[176]

$$PMF(r) = \int_d^r \langle f(r) \rangle dr + k_B T \ln(r/d) \quad (4-1)$$

where  $d$  is the largest separation distance along  $r$ ,  $k_B$  is the Boltzmann constant, and  $T = 318$  K is the temperature in degrees Kelvin. Note that  $k_B T \ln(r/d)$  accounts for the entropy loss of the diazonium ion resulting from the decrease in the area of the concentric surface from  $2\pi dL$  to  $2\pi rL$ , where  $L$  is the length of the simulated SWCNT. Different initial diazonium ion configurations (different molecular orientations as well as different positions on the SWCNT cylindrical surface) were tested to ensure that the PMF results were independent of the initial

configuration.

#### **4.2.2 Experimental Methods**

Diazonium-SWCNT functionalizations in aqueous SDS and SC solutions were carried out by pre-heating 2 mL and 3 mL, respectively, of 15 mg/L SWCNT dispersion samples at pH = 5 to 45°C, allowing them to stabilize at that temperature, and initiating the functionalization by single additions of diazonium salt to the well-stirred vessel. The solutions were then allowed to react for 24 hours, at which point there was negligible residual diazonium ions in solution. Due to the repulsive interactions between the positively-charged SWCNT-CTAB complex and the positively-charged diazonium ion, the diazonium-SWCNT reactions in the aqueous CTAB solution took significant longer time to reach completion. The above functionalization was carried out at 27°C and pH = 5 in 2 mL of 15 mg/L SWCNT dispersion sample, and initiated by a single addition of diazonium salt. Samples were allowed to react for 2.5 weeks, at which point there was little residual diazonium ions in the solution. Photoluminescence (785 nm excitation) data were acquired using a home-built near-infrared fluorescence microscope which has been described elsewhere.[186] Deconvolution of the photoluminescence (PL) spectra allowed for more accurate analysis of the fractional quenching behavior of the (7,5) nanotube considered in this study (see Appendix B).

### **4.3 Results and Discussions**

#### **4.3.1 Free-Energy Calculations of Diazonium Ion Adsorption**

The surface self-assembly structures formed by several surfactants (e.g., SDS, SC, and SDBS (sodium dodecyl benzene sulfonate)) on SWCNTs have been studied previously using all-atomistic MD simulations.[91, 93, 158, 187] The simulated surface structures of the SWCNT-surfactant complexes considered here (SC, SDS, and CTAB which is simulated for the

first time) are shown in Figure 4-2. The simulated surface self-assembly structures are consistent with those reported earlier for both the flexible surfactant (SDS)[91] and the rigid surfactant (SC)[158] at low and high surface coverages on a (6,6) SWCNT.

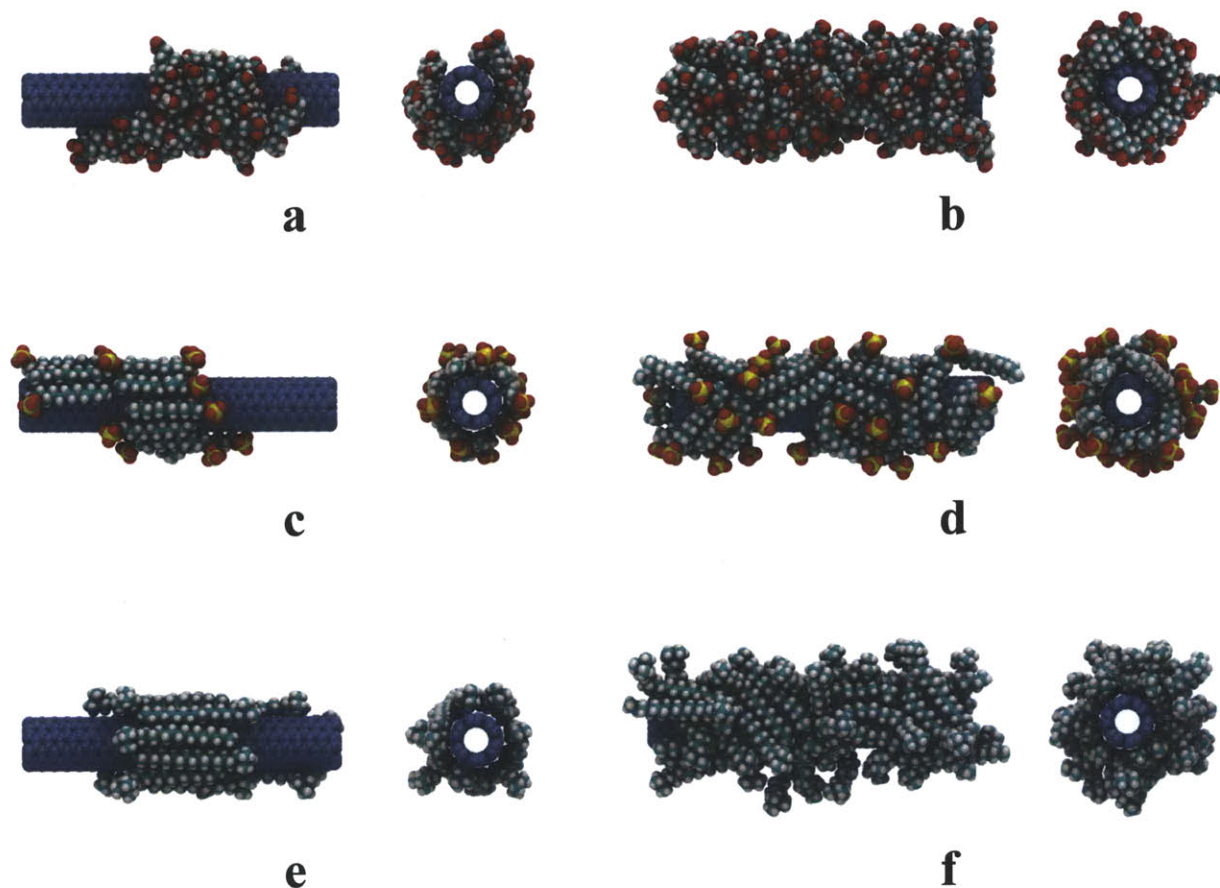


**Figure 4-2:** Post-equilibrium simulation snapshots of SWCNTs covered with surfactants, showing the surface structures of the various surfactants considered here. (a) and (b) for the SC case, (c) and (d) for the SDS case, and (e) and (f) for the CTAB case. Within each row, the side view is on the left and the front view is on the right. (a), (c), and (e) correspond to low surfactant surface coverages, while (b), (d), and (f) correspond to high surfactant surface coverages. Water molecules and counterions are not shown for clarity. Color code: red – oxygen, light blue – carbon, white – hydrogen, dark blue – nitrogen, and purple – carbon in the SWCNT.

The simulated potential of mean force (PMF) profiles between the single diazonium ion and the SWCNT-surfactant complexes are shown in Figure 4-3. For  $r > 1.8$  nm, where the diazonium ion

has very weak interactions with the SWCNT-surfactant complex through short-range van der Waals (vdW) forces (reflected in the Lennard-Jones model),<sup>[158]</sup> the long-range electrostatic interactions between the diazonium cation and the charged SWCNT-surfactant complexes dominate. Note that the interaction force between the diazonium ion and the SWCNT-surfactant complex is related to the slope of the PMF along  $r$ , because it is equal to the derivative of the PMF along  $r$  (see Eq. (4-1)). By convention, the attractive force is related to a positive slope and the repulsive force is related to a negative slope. As expected, the electrostatic forces exerted on the diazonium cation by the negatively-charged SWCNT-surfactant (SC and SDS) complexes are attractive, with the PMF profile exhibiting a positive slope (see the red solid and dashed lines for SC, as well as the blue solid and dashed lines for SDS in Figure 4-3). On the other hand, these forces are repulsive in the case of the positively-charged SWCNT-surfactant (CTAB) complex, with the PMF profile exhibiting a negative slope (see the purple solid and dashed lines in Figure 4-3). For comparison, the force exerted on the diazonium ion by the uncharged, bare SWCNT in water is almost zero, with a horizontal PMF profile (see the green dashed line in Figure 4-3). The different surface charge densities corresponding to the low and high surface coverages affect the strength of the long-range electrostatic interactions; however, these differences are negligible for large  $r$  values where the electrostatic interactions are relatively weak.

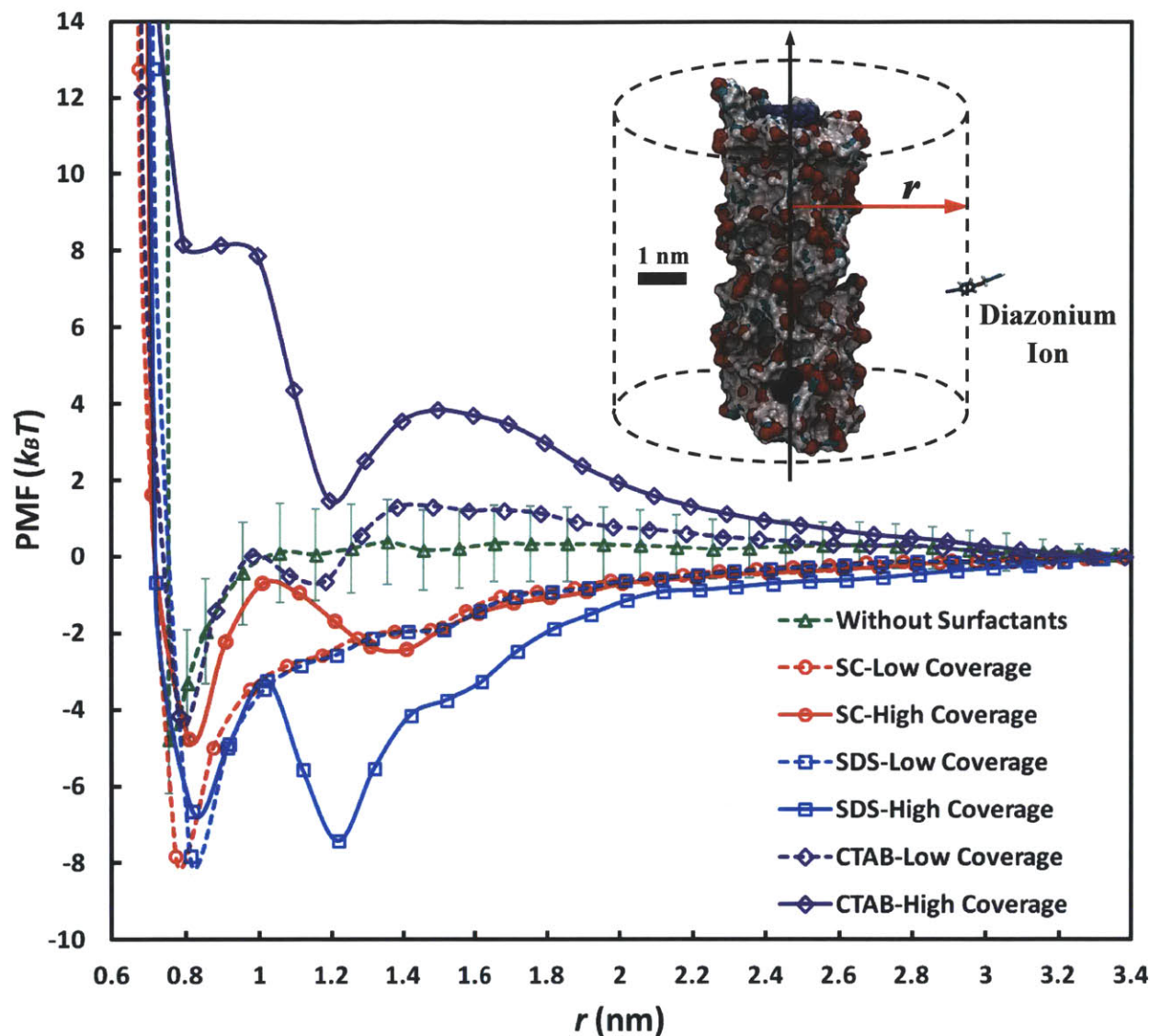


**Figure 4-3:** Simulated PMF profiles between the diazonium ion and the SWCNT-surfactant complexes corresponding to SC, SDS, and CTAB for both low and high surface coverages. The no surfactant case (that is, the bare SWCNT in water) is also shown for comparison. The error bars in green, corresponding to the simulated no surfactant case, represent the typical errors in the PMF calculations for the surfactant cases simulated here ( $< 2 k_B T$ ). The inset shows a schematic drawing of the cylindrical axis (z-axis) of the SWCNT (the black arrow), the constraint distance,  $r$ , between this axis and the diazonium ion (the red arrow), and the cylindrical surface on which the diazonium ion can move freely (the black dashed lines). The simulation snapshot of the high-surface coverage SWCNT-SC complex is used here. Water molecules and counterions are not shown for clarity. The color code is the same as the one used in Figure 4-2.

As the diazonium ion approaches the SWCNT-surfactant complex before establishing direct contacts with the complex ( $1.2 \text{ nm} < r < 1.8 \text{ nm}$ ), the strong vdW attraction between the diazonium ion and the SWCNT-surfactant complex comes into play, and favors adsorption of the diazonium ion. Note that the adsorption of the diazonium ion first occurs onto the coated surfactant layers rather than directly onto the nanotube surface. This results in a local free-energy minimum at  $r = 1.2 \text{ nm}$  (for SDS and CTAB, with a vdW radius of  $\sim 0.25 \text{ nm}$  for the cross-sectional area of the linear alkyl tail) or  $1.4 \text{ nm}$  (for SC, because of its larger molecular size as a rigid surfactant, with a thickness of  $\sim 0.45 \text{ nm}$  for the bean-like molecule[158]). Note that the adsorption discussed here is clearly seen only at high surfactant surface coverages, because at low surfactant surface coverages the attractive and the repulsive forces are both weak. Indeed, the PMF profiles for SC and SDS corresponding to the low surfactant surface coverages are very similar (see the red and the blue dashed lines in Figure 4-3), reflecting a lack of molecular discrimination between different surfactants of the same charge when the diazonium ions adsorb on low-surface-coverage SWCNT-surfactant complexes. Interestingly, however, one observes a much larger increase in the attraction between the positively-charged diazonium ion and the high-surface coverage, negatively-charged SWCNT-SDS complex than in the case of the high-surface coverage, negatively-charged SWCNT-SC complex (see the red and the blue solid lines in Figure 4-3). This stronger attraction is surprising because the electrostatic contribution to the PMF profile is expected to be similar for the same surfactant surface coverage (or surface charge density), as expected from the conventional Poisson-Boltzmann equation[31] for SWCNT-surfactant complexes with similar radii (discussed further in Section 4.3.2). The resulting local free-energy well depth is  $-7.4 \pm 2.0 k_B T$  at  $r = 1.2 \text{ nm}$  in the case of SDS, and  $-2.4 \pm 2.0 k_B T$  at  $r = 1.4 \text{ nm}$  in the case of SC. This clearly shows that the binding affinity of the diazonium ion on the surfactant layer of the SWCNT-SDS complex is much stronger (by  $-5.0 k_B T$ ) than that on the SWCNT-SC complex.

For  $r < 1.2 \text{ nm}$  (for SDS and CTAB) and  $r < 1.4 \text{ nm}$  (for SC), the diazonium ion begins to push away the adsorbed surfactant molecules in order to contact the SWCNT surface directly, which



results in the free-energy barrier for all the surfactant cases considered within the range  $1.0 \text{ nm} < r < 1.2 \text{ nm}$  (see Figure 4-3). Direct contact of the diazonium ion on the SWCNT surface results in the local free-energy minima observed at  $r = 0.8 \text{ nm}$  (again, for all the surfactant cases considered). For  $r < 0.8 \text{ nm}$ , the repulsive force between the diazonium ion and the SWCNT increases sharply, as clearly seen in Figure 4-3.

A quantitative measure of the free energy associated with the diazonium ion adsorption (prior to any covalent reaction),  $\Delta G_A$ , corresponds to the lowest PMF value at which the diazonium ion adsorbs stably onto the surfactant layer (for SDS and CTAB, both at  $r = 1.2 \text{ nm}$ ) or directly onto the SWCNT (for SC, at  $r = 0.8 \text{ nm}$ ). This difference in the stably-adsorbed positions may be due to the competing effects between electrostatic, vdW, and steric interactions for the different surfactant cases. Experimentally, surfactants are typically added into the SWCNT solution at saturation levels. Consequently, I utilized the simulated PMF profiles corresponding to the high-surface coverage SWCNT-surfactant complexes to determine the value of  $\Delta G_A$  for SDS, CTAB, and SC. Although it has been proposed that the covalent reaction of the diazonium ions with the  $sp^2$  carbons on the nanotube sidewall occurs directly on the SWCNT surface, contact of the diazonium ions with the surfactant layers may still affect the reaction with the SWCNT. In fact, the actual reaction pathway corresponding to the SWCNT-surfactant complex functionalization by diazonium salts is still unknown, and therefore, the definition of the free energy of diazonium adsorption presented here should be viewed as an approximate quantitative measure, with additional reaction-pathway studies required in the future. The simulated  $\Delta G_A$  values are listed in Table 4-1 for the SC, SDS, and CTAB cases. The negative  $\Delta G_A$  values for SC ( $-4.8 \pm 2.0 k_B T$ ) and SDS ( $-7.4 \pm 2.0 k_B T$ ) indicate preferential adsorption of diazonium ions onto SWCNTs. On the other hand, the positive  $\Delta G_A$  value for CTAB ( $1.5 \pm 1.0 k_B T$ ) indicates preferential desorption of diazonium ions from the SWCNTs. Overall, the binding affinity ( $K_A$ , see Eq. (4-3) in Section 4.3.3) of the diazonium ions on various SWCNT-surfactant complexes ranks as follows: SDS > SC > CTAB, while the experimental extent of diazonium functionalization (see Section 4.3.3 for the definition) is ranked as follows: SDS > CTAB > SC

(see Figure 4-5-a). This discrepancy (the switch between CTAB and SC) indicates that covalent reactions between diazonium ions and SWCNTs, in addition to noncovalent adsorptions, may also be affected by the surfactants used, and will be discussed further in Section 4.3.3.

### 4.3.2 Understanding the Synergetic Binding Affinity

To better understand the role of surfactants in determining the ranking of the  $\Delta G_A$  values using the simulated PMF profile, I calculated the interaction potential energies between the diazonium ion and the SC, SDS, and CTAB molecules adsorbed onto the SWCNT surface at high surfactant surface coverages as a function of  $r$ . The calculated potential energy profiles in Figure 4-4-a capture the main feature of the PMF profile in Figure 4-3, showing that the SDS curve (blue line) lies below the SC curve (red line), which reflects the stronger interaction (having a more negative potential energy value) between the diazonium ion and the SDS molecules than between the diazonium ion and the SC molecules. In addition, the CTAB curve (green line) lies above both the SC and the SDS curves, which reflects the weakest interaction (having more positive potential energy values) between the diazonium ion and the CTAB molecules. This ranking of the magnitudes of the potential energies (SDS > SC > CTAB) is fully consistent with that of the predicted binding affinities based on the free energies of adsorption. This indicates that the potential energy contribution to the free energy of adsorption is dominant, compared to other contributions such as the solvent effect (e.g., the confinement of water molecules between the diazonium ion and the SWCNT-surfactant complex), or the entropic effect (e.g., the orientational entropy of water molecules around the diazonium ion and the surfactant molecules, and the orientational entropy of the diazonium ion itself). Note that the various minima and maxima observed in Figure 4-4-a are consistent with those in Figure 4-3, with similar features being observed in Figures 4-4-b and 4-4-c.

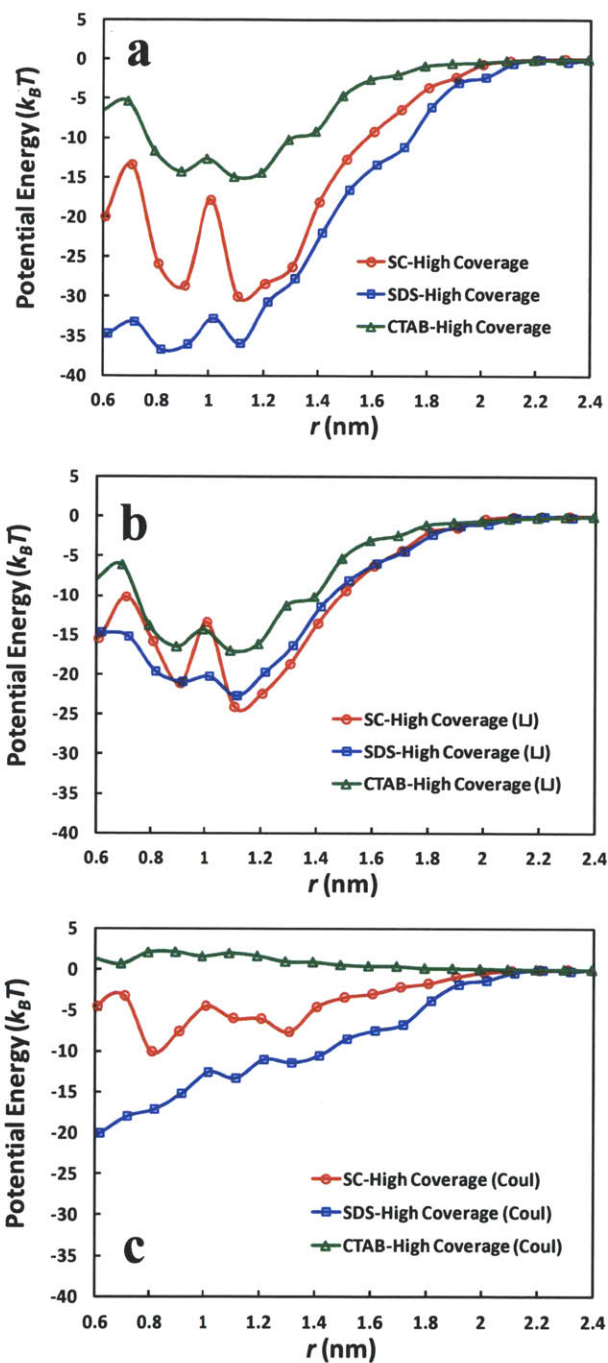


**Figure 4-4:** (a) Interaction potential energy between the diazonium ion and SC, SDS, and CTAB molecules adsorbed on the SWCNT surface at high surfactant surface coverages, as a function of  $r$ . (b) The Lennard-Jones (LJ) contribution to the potential energy in (a), which reflects both the vdW and the steric interactions between the diazonium ion and the surfactant molecules. (c) The Coulombic (Coul) contribution to the potential energy in (a), which reflects the electrostatic interactions between the diazonium ion and the surfactant molecules.

The potential energy was further decomposed into Lennard-Jones (LJ) and Coulombic (Coul) contributions, as shown in Figures 4-4-b and 4-4-c, respectively. Note that the vdW and steric interactions are reflected in the LJ contribution, while the electrostatic interactions are reflected in the Coul contribution. As shown in Figure 4-4-b, the LJ contributions to the potential energies for SC, SDS, and CTAB are relatively close (within  $5 k_B T$  from each other), exhibiting various overlaps for the three curves. On the other hand, in Figure 4-4-c, the Coul contributions are quite different from each other, with positive values for the positively-charged CTAB molecules (which repel the diazonium ion) and negative values for the negatively-charged SDS and SC molecules (which attract the diazonium ion). The clear ranking of the binding affinities due to the Coul contribution (SDS > SC > CTAB) is fully consistent with that of the predicted binding affinities based on the free energies of adsorption. This finding confirms that the primary contribution to the binding affinities of the diazonium ions with the SWCNT-surfactant complexes is electrostatic.

We would like to better understand the unexpected, strong binding affinity between the diazonium ion and the SWCNT-SDS complex relative to that corresponding to the SWCNT-SC complex, with particular emphasis on the role of the electrostatic interaction, which as shown above, are the dominant ones. As discussed earlier, SWCNT surfaces covered with surfactants are heterogeneous, with mobile charges carried by the surfactant heads. It is therefore important to monitor how these mobile charges distribute as a diazonium ion approaches the SWCNT-surfactant complex. A useful way developed here to visualize the charge distribution involves using simulated density maps of the charged surfactant head groups (carboxylate for SC, sulfate for SDS, and trimethylammonium for CTAB) projected onto an unrolled, 2D, flat SWCNT surface. The simulated density maps are shown in Figure 4-5, where each map has been centered at the position of the charged diazo group ( $-N^+ \equiv N$ ) of the diazonium ion, as projected on the SWCNT surface.

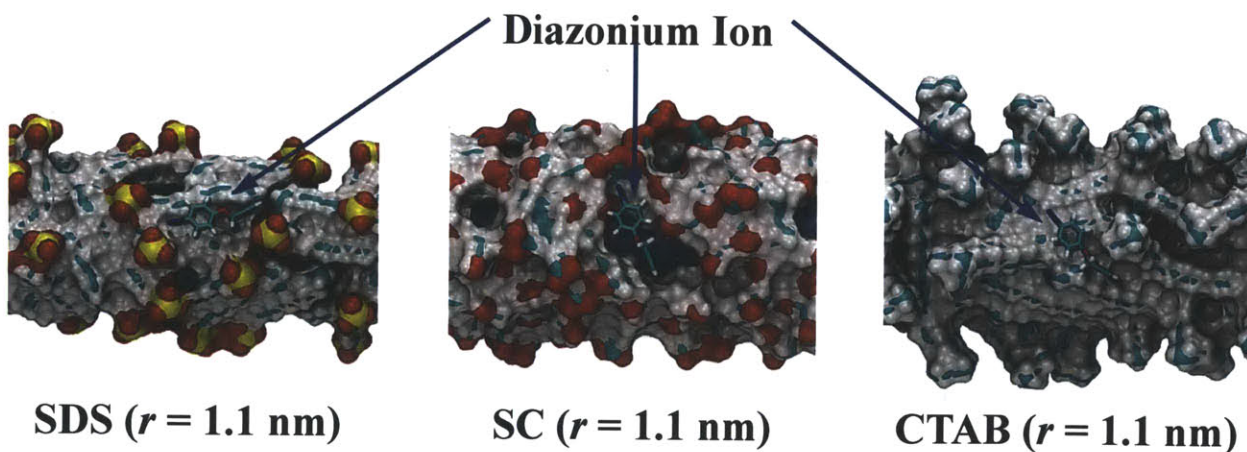
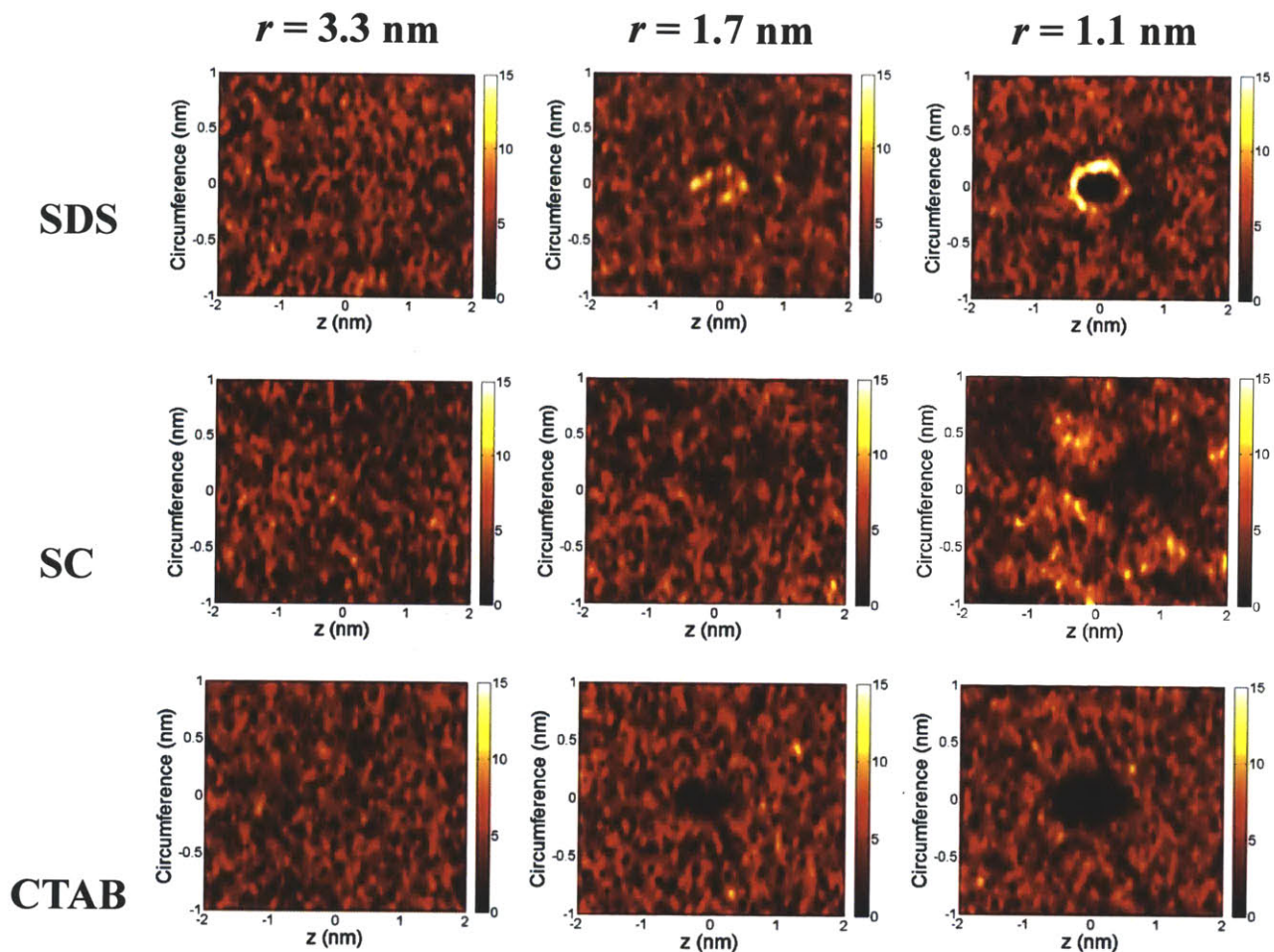


**Figure 4-5:** Projected density maps of charged surfactant head groups on the unrolled SWCNT surface (tube length  $\times$  tube circumference) for: SDS (top row), SC (middle row), and CTAB (bottom row). Within each plot, the diazonium ion approaches the SWCNT-surfactant complex gradually from the left to the right, where the left subplot:  $r = 3.3$  nm, middle subplot:  $r = 1.7$  nm, and right subplot:  $r = 1.1$  nm. The y-axis measures the circumference of the SWCNT, and the z-axis measures the length of the SWCNT. Density maps are shown as contour plots with arbitrary

units. Color bar code: lighter color corresponds to high surfactant head densities and darker color corresponds to low surfactant head densities. The origin of each plot at  $y = z = 0$  denotes the projected position of the charged diazo group ( $-N^+ \equiv N$ ) of the diazonium ion. Each density map was averaged over the last 20 ns of each simulation. Representative simulation snapshots showing the binding of the diazonium ion (the blue arrows) to the charged surfactant layer on the SWCNT surface are shown at the bottom of the density maps corresponding to  $r = 1.1$  nm. The color code is the same as the one used in Figure 4-2. Note that the diazonium ion and the various SWCNT-surfactant complexes are drawn in the “Licorice” and the “Surf” representation in VMD,[188] respectively, to facilitate distinction between the two.

For  $r = 3.3$  nm, the density maps are very similar for the three surfactants considered, demonstrating a homogeneous distribution of the surfactant head groups. This is expected, since the diazonium ion is not close enough to the SWCNT surface to affect the surface organization of the surfactant molecules via electrostatic interactions. For  $r = 1.7$  nm, the diazonium ion begins to interact with the surfactant molecules directly through the formation of ionic bonds (attractive for SC and SDS, and repulsive for CTAB),[176] similar to the formation of a salt bridge in the case of counterion binding.[31] The ionic bonding is even stronger when the diazonium ion can approach the SWCNT-surfactant complex closer to make direct contact at  $r = 1.1$  nm, as reflected by the increase in the extents of both the “hot spots” (high surfactant head density) and “cold spots” (low surfactant head density). This reflects the increase in the synergistic electrostatic interaction (attractive for “hot spots” and repulsive for “cold spots”) between the diazo group and the surfactant heads. Note, however, that ionic bonding is only apparent for the linear surfactants (SDS and CTAB, see the  $r = 1.1$  nm column in Figure 4-5), and not for the rigid surfactant (SC, see the  $r = 1.1$  nm column in Figure 5). Indeed, as shown in the  $r = 1.1$  nm column in Figure 4-5, the cationic diazo group attracts anionic SDS sulfate groups (brighter ring), while it repels cationic CTAB trimethylammonium groups (appears as a dark hole in the plot, since the origin of the density map is always occupied by the diazo group itself at small  $r$  values).

In the case of SC (see the middle row in Figure 4-5), for  $r = 1.7$  nm or 1.1 nm, I did not observe any “hot spots” for the carboxylate head groups around the diazo group, although one can

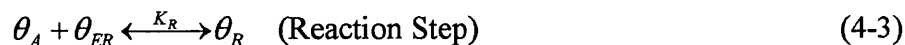
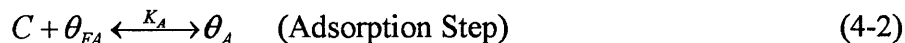
observe a small extent of ordering of the carboxylate groups at  $r = 1.1$  nm. Synergistic electrostatic attractions between the cationic diazo group and the anionic SDS and SC head groups lead to the rearrangement of these surfactant molecules on the SWCNT surface, leading to their localization around the diazonium ion, and giving rise to the local “hot spots”. This surface rearrangement can maximize the contacts of the anionic SDS and SC molecules with the cationic diazo group, thereby lowering the free energy of the system. On the other hand, antagonistic electrostatic repulsions occur between the cationic diazo group and the cationic CTAB head groups, giving rise to the local “cold spots”. The finding that the linear, flexible SDS molecules can rearrange on the SWCNT surface more readily than the bulkier, rigid SC molecules and thereby generate a greater extent of “hot spots” formation, is consistent with my recently reported numbers of ionic bonds formed between the diazo groups and the head groups of SDS ( $\sim 2.4$  at  $r = 1.1$  nm) and SC ( $\sim 1.5$  at  $r = 1.1$  nm),[176] which can serve as a quantitative measure of the local “hot spots”. The three representative simulation snapshots at the bottom of Figure 4-5 show the close binding of the diazonium ion to the charged surfactant layer (SDS, SC, and CTAB) on the SWCNT surface at  $r = 1.1$  nm. The diazonium ion lies in parallel to the SWCNT surface when closely bound to the surfactant layer. Its orientation relative to the SWCNT axis is not fixed, and it depends on the detailed self-assembly structure of the surfactant layer.

### 4.3.3 Model for the Extent of SWCNT Functionalization

We have recently modeled kinetic properties, such as reaction rates associated with the diazonium-SWCNT functionalization process, by combining a diffusion-limited model and the Poisson-Boltzmann equation.[176] Here, I focus on modeling the equilibrium (steady-state) extent of diazonium-SWCNT functionalization using the simulated free energies of adsorption and experimental data. It is noteworthy that the simulated free energy of adsorption may be used to replace the Poisson-Boltzmann equation when combined with the diffusion-limited model in



order to predict kinetic properties, such as the aggregation rate, as I have shown recently.[156, 173] Specifically, I propose the following two-step adsorption-reaction model for the diazonium-SWCNT functionalization process (see Figure 4-1-e), a description that is more general than that presented in Ref. [90]. Specifically,



where  $C$  denotes the bulk concentration of the diazonium salt (in units of diazonium/water molar ratio),  $\theta_{EA}$  denotes the number of empty adsorption sites available to the diazonium ions on the nanotube surface (in units of diazonium/water molar ratio per nm, which is a linear packing density on the SWCNT surface),  $\theta_A$  denotes the number of sites occupied by the adsorbed diazonium ions,  $\theta_{ER}$  denotes the number of empty reaction sites available to the diazonium ions, and  $\theta_R$  denotes the number of sites occupied by the reacted diazonium ions (where the units of  $\theta_A$ ,  $\theta_{ER}$ , and  $\theta_R$  are the same as that of  $\theta_{EA}$ ),  $K_A$  is the adsorption constant, and  $K_R$  is the reaction constant. Unlike the previous model,[176] I assume that the adsorbed diazonium ions can react with the carbon atoms on the SWCNT sidewall reversibly in order to investigate the equilibrium reaction properties (e.g.,  $\theta_{ER}$ ,  $\theta_R$ , and  $K_R$ ).

Knowing  $\Delta G_A$ , the simulated free energy of adsorption (i.e., the free-energy difference between the adsorbed and the desorbed states), which can be obtained from the PMF calculations, the adsorption constant,  $K_A$ , can be determined using Arrhenius' law, in order to relate  $C$ ,  $\theta_{EA}$ , and  $\theta_A$ . Specifically,

$$K_A = \frac{\theta_A}{C \theta_{EA}} = e^{-\Delta G_A / k_B T} \quad (4-4)$$

The total number of available adsorption sites on the nanotube,  $\theta_{TA}$ , is given by  $\theta_{TA} = \theta_{EA} + \theta_A$ . Since the reaction is carried out at infinite dilution of the diazonium salt, it follows that  $\theta_{TA} \gg \theta_A$ , which leads to  $\theta_{EA} \approx \theta_{TA}$ . Using this result in Eq. (4-4), it follows that:



$$\theta_A = K_A \theta_{TA} C \quad (4-5)$$

Note that Eq. (4-5) is the celebrated Henry's adsorption isotherm, where  $K_A$  is Henry's constant. Note also that the bulk concentration of the diazonium salt,  $C$ , decreases as the number of adsorbed diazonium ions,  $\theta_A$ , increases. This observation can be expressed as follows:  $C = C_0 - l \theta_A$ , where  $C_0$  is the initial concentration of the diazonium salt added to the SWCNT solution, and  $l$  is the total length of the SWCNTs in the solution. Note that the effect of adsorption on the value of  $C$  cannot be neglected, because  $l$  is typically quite large. Using the expression for  $C$  in terms of  $C_0$  and  $l$  in Eq. (4-5), and rearranging results in:

$$\theta_A = \frac{K_A \theta_{TA} C_0}{1 + K_A \theta_{TA} l} \quad (4-6)$$

The total number of available reaction sites on the nanotube,  $\theta_{TR}$ , is given by  $\theta_{TR} = \theta_{ER} + \theta_R$ . Unlike the adsorption step,  $\theta_R$  is not negligible relative to  $\theta_{TR}$ . Therefore, the reaction step associated with the reaction constant,  $K_R$ , may be modeled using a Langmuir isotherm. It is important to recognize that the incorporation of a ceiling for reaction,  $\theta_{TR}$ , is essential in order to capture the quenching saturation phenomenon as  $C_0$  increases.[176] Indeed, this saturation phenomenon cannot be simply explained by the diazonium adsorption process, as described using the linear relationship in Eq. (4-6). Specifically,

$$K_R = \frac{\theta_R}{\theta_A \theta_{ER}} = \frac{\theta_R}{\theta_A (\theta_{TR} - \theta_R)} \Rightarrow \theta_R = \frac{K_R \theta_A}{1 + K_R \theta_A} \theta_{TR} \quad (4-7)$$

Experimentally, the equilibrium extent of functionalization,  $f_{(m,n)}^i$ , as a function of both the carbon nanotube type (i.e., chirality),  $(m,n)$ , and the surfactant type,  $i$ , was estimated from the fractional quenching data in the PL spectra (the change in the PL intensity after functionalization, normalized by the original intensity).[176] Here, as proof-of-concept, I have only investigated one carbon nanotube species (7,5), with diameter  $d = 0.81$  nm, and  $i =$  CTAB, SDS, and SC. Since I am only considering a single nanotube species, differences in electronic structure, across

nanotube species, are not relevant to the physical adsorption of the diazonium ions. As a result,  $K_A$ ,  $K_R$ ,  $\theta_{TA}$ , and  $\theta_{TR}$  are only functions of the nanotube diameter,  $d$ , and the surfactant type,  $i$ . Note that the simulated (6,6) SWCNT has almost the same tube diameter as the (7,5) SWCNT, and therefore, can be utilized to approximate the (7,5) SWCNT disregarding the difference in chirality. This is suggested in a recent simulation study showing that surfactants adsorbed on a graphite surface are highly disordered without any orientation preference for chirality angles.[155] Assuming that each diazonium ion contributes the same extent of PL quenching to the total extent of PL quenching, I can relate the extent of functionalization considered here,  $f_{(7,5)}^i$ , to the reacted diazonium surface coverage,  $\theta_R$ , through a simple proportionality relationship, with a proportionality constant  $P$  (in units of nm per diazonium/water molar ratio). Specifically,

$$f_{(7,5)}^i = P\theta_R \quad (4-8)$$

By substituting Eqs. (4-6) and (4-7) into Eq. (4-8), I can obtain a master equation that relates  $f_{(7,5)}^i$  to various parameters. Specifically:

$$f_{(7,5)}^i = \frac{P\theta_{TR}\theta_{TA}K_RK_AC_0}{1 + \theta_{TA}K_RK_AC_0 + \theta_{TA}K_AI} = \frac{AK_RK_AC_0}{1/\theta_{TA} + K_RK_AC_0 + K_AI} \quad (4-9)$$

where  $A = P\theta_{TR}$ , which is equal to the saturated (or maximum) extent of functionalization,  $\max(f_{(7,5)}^i)$ , as  $C_0$  approaches infinity. Note that  $K_A$  can be predicted using the simulated  $\Delta G_A$  values for each surfactant type, and  $C_0$  is tuned experimentally. On the other hand, estimates of  $A$ ,  $\theta_{TA}$ , and  $K_R$  are not available directly from either simulations or experiments. Fortunately, I can obtain these three unknown parameters by fitting Eq. (4-9) to the available experimental data for the diazonium-functionalized (7,5) SWCNTs in SC, SDS, and CTAB solutions ( $f_{(7,5)}^{SC}$ ,  $f_{(7,5)}^{SDS}$ , and  $f_{(7,5)}^{CTAB}$ ), respectively. The resulting fitting curves for various  $C_0$  values are shown in Figure 4-6-a. Note that, in Figure 4-6-a, the  $C_0$  value was converted into diazonium/carbon (one carbon atom in the SWCNT) molar ratio, according to the carbon/water molar ratio of  $2.25 \times 10^{-5}$  (for the 15

mg/L SWCNT solution used here). Specifically, the  $l$  values were estimated from the total mass of the SWCNTs (see Section 4.2.2), and the number of carbon atoms in the SWCNT per unit length ( $\sim 100$  atoms/nm for the (7,5) SWCNT as a rough approximation).

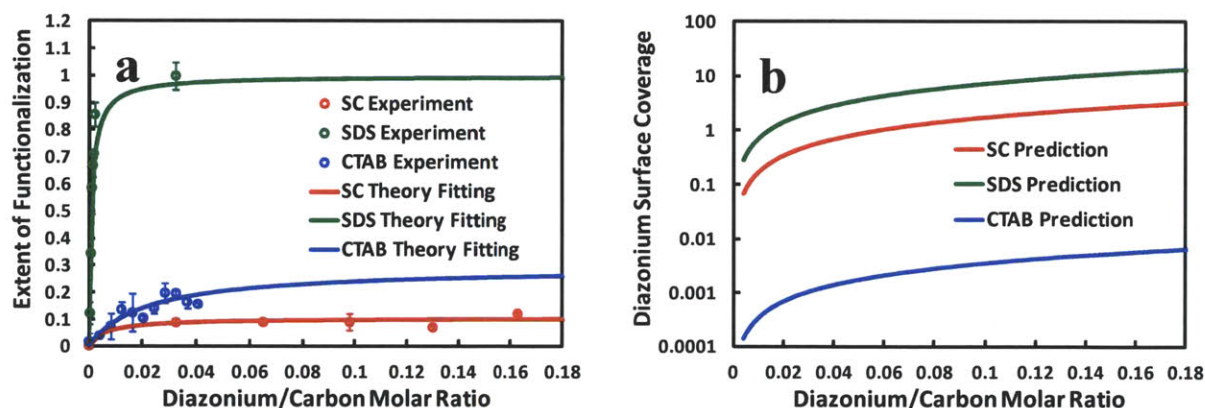


**Figure 4-6:** (a) Experimental data (circles) and theoretical fitting results (solid lines) for the extents of functionalization ( $f_{(7,5)}^{SC}$ ,  $f_{(7,5)}^{SDS}$ , and  $f_{(7,5)}^{CTAB}$ ) as a function of the diazonium/carbon molar ratio. The solid lines were predicted using Eq. (4-9), and the corresponding fitting parameters are listed in Table 4-1. (b) Predicted diazonium ion surface coverage (adsorption isotherm),  $\theta_A$  (in units of number of diazonium ions per nm of a SWCNT), as a function of the diazonium/carbon molar ratio, using Eq. (4-6) and the fitting parameters listed in Table 4-1.

#### 4.3.4 Modeling Results and Discussions

The deduced fitting parameters,  $A$ ,  $\theta_{TA}$ , and  $K_R$  are listed in Table 4-1, demonstrating the ability of Eq. (4-9) to model the concentration-dependent extent of functionalization shown in Figure 4-6-a. The nonlinear minimization algorithm for the least-squares fitting was carried out utilizing the interior-reflective Newton method subroutine in the MATLAB numerical library. The fitted  $A$  values (i.e.,  $\max(f_{(7,5)}^i)$ ) are ranked as follows: SDS > CTAB > SC, consistent with the experimental extents of functionalization shown in Figure 4-6-a. The higher  $A$  value for CTAB than for SC indicates that although the anionic surfactant SC yields a larger diazonium binding affinity than the cationic surfactant CTAB, diazonium ions adsorbed, and subsequently, reacted

on the SWCNT-CTAB complex can quench the PL intensity more effectively. This effectiveness may be due to the fact that the diazonium reaction can occur randomly along the nanotube for the linear surfactant CTAB, while it occurs very close to a pre-occupied reaction site for the rigid surfactant SC. As shown in Figure 4-5, CTAB (or any other linear surfactant) molecules are more likely to restructure for the diazonium ion to adsorb randomly on the nanotube surface. On the other hand, this is less likely for SC molecules, which leads to multiple diazonium reactions occurring within the same PL-quenched region along the nanotube (i.e., less effectiveness per reacted diazonium ion). This leads to the discrepancy in the rankings of the simulated  $K_A$  values and the experimental extents of functionalization for the different surfactant cases considered, as stressed in Section 4.3.1.

**Table 4-1:** Summary of parameter values for  $A = P\theta_{TR}$ ,  $\theta_{TA}$ , and  $K_R$  in Eq. (4-9) by fitting to the experimental values of  $C_0$  and  $f_{(m,n)}^i$  (see Figure 4-6-a) with constants  $l$  and  $K_A$  using the simulated  $\Delta G_A$  values in Eq. (4-4)

Surfactant Type	$l$ (nm)	$\Delta G_A$ ( $k_B T$ )	$K_A$	$A = P\theta_{TR}$	$\theta_{TA}$	$K_R$
SC	$2.26 \times 10^{16}$	$-4.8 \pm 2.0$	$1.22 \times 10^2$	0.105	$7.49 \times 10^{-20}$	$9.35 \times 10^{23}$
SDS	$1.505 \times 10^{16}$	$-7.4 \pm 2.0$	$1.64 \times 10^3$	1.000	$1.05 \times 10^{-19}$	$9.22 \times 10^{23}$
CTAB	$1.505 \times 10^{16}$	$1.5 \pm 1.0$	$2.23 \times 10^{-1}$	0.292	$7.65 \times 10^{-21}$	$1.24 \times 10^{27}$

The fitted  $\theta_{TA}$  values are ranked as follows: SDS > SC > CTAB, consistent with the ranked  $K_A$  values in Section 4.3.1. The fitted  $K_R$  values for the two anionic surfactants (SC and SDS) are very similar ( $\sim 10^{24}$ ), while the  $K_R$  value for CTAB is much larger ( $\sim 10^{27}$ ). This  $K_R$  difference suggests that cationic surfactants may modify the electronic structure of the SWCNT upon adsorption, which in turn, would enhance the reactivity of the SWCNT with the diazonium ions. The fitted  $K_R$  value corresponds to the free energy of diazonium-SWCNT reaction (determined using Arrhenius' law similar to Eq. (4-4)),  $\Delta G_R = -55 k_B T$  ( $-1.40$  eV) for SC and SDS, and  $\Delta G_R = -62 k_B T$  ( $-1.59$  eV) for CTAB, which are consistent with the QM simulated binding energy for

the desorption process of phenyl from bare (5,5) SWCNT (-1.42 eV).[189] In addition, note that  $K_R$  is much larger than  $K_A$ , which indicates that the reaction of the diazonium ion with the SWCNT sidewall is highly favorable, a finding which is consistent with the previously proposed irreversible reaction step.[90]

Although estimates of  $A = P\theta_{TR}$  are not available experimentally, there is experimental evidence that each individual reacted diazonium ion on the nanotube sidewall (referred to as a quenching site) can quench the PL intensity (excitons generated upon photon excitation) of every 100 ~ 300 nm of nanotube.[69, 70, 190] This length along the nanotube,  $\Lambda$ , is referred to as the effective mean quenching range of a single reacted diazonium ion.[70] Fundamentally,  $\Lambda$  can also be referred to as the exciton diffusion range for the functionalized SWCNT, a range for which an exciton can travel during its life time.[69] Experimental evidence based on time-dependent PL intensities (exciton kinetics) have shown that the value of  $\Lambda$  depends on both the SWCNT chirality[190] and the surfactant (e.g., SC, SDBS, SDC (sodium deoxycholate), and STC (sodium taurocholate)) utilized to disperse the SWCNT.[70] From the experimentally estimated value of  $\Lambda = 178 \pm 20$  nm per reacted diazonium ion for (7,5) SWCNTs dispersed in an aqueous SC solution,[70] I can estimate the corresponding proportionality constant  $P$  in Eq. (4-8). Specifically,

$$P = \Lambda N_{water} \quad (4-10)$$

where  $N_{water}$  is the number of water molecules in the SWCNT solution, which is about  $10^{23}$  for the 3 mL aqueous SC solution (see Section 4.2.2). In addition, based on the relation that  $A = P\theta_{TR}$ , I can estimate the corresponding value of  $\theta_{TR}$ . Specifically,

$$\theta_{TR} = \frac{A}{P} = \frac{A}{\Lambda N_{water}} \quad (4-11)$$

Using the values of  $\Lambda$  and  $N_{water}$  given above in Eqs. (4-10) and (4-11), I find that:  $P = 1.78 \times 10^{25}$  nm per diazonium/water molar ratio, and  $\theta_{TR} = 5.90 \times 10^{-27}$  diazonium/water molar ratio per nm (or ~ 6 reacted diazonium ions per  $10^4$  nm of the SWCNT). The predicted  $\theta_{TR}$  value is 7

orders of magnitude smaller than the  $\theta_{TA}$  value ( $7.49 \times 10^{-20}$  diazonium/water molar ratio per nm), which reflects the fact that very few physically adsorbed diazonium ions will eventually react with the nanotube sidewall to form covalent bonds. If experimental values of  $\Lambda$  were available for SDS and CTAB, I would also be able to accurately predict the corresponding  $P$  and  $\theta_{TR}$  values. As an order of magnitude estimation, the values of  $P$  and  $\theta_{TR}$  should be  $\sim 10^{25}$  nm per diazonium/water molar ratio, and 1 to 10 reacted diazonium ions per  $10^3$  nm of the SWCNT, respectively, regardless of the surfactant type and the SWCNT species.

Using the fitted values of  $A$ ,  $\theta_{TA}$ , and  $K_R$  in Eq. (4-6), I can independently predict the surface coverage (adsorption isotherm) of the diazonium ions on the various SWCNT-surfactant complexes (see Figure 4-6-b). The predicted surface coverage profiles are consistent with the ranked  $K_A$  and  $\theta_{TA}$  values for SDS, SC, and CTAB. As can be seen, the predicted surface coverages span 5 orders of magnitude (from 0.0001 to 10 diazonium ions per nm of the SWCNT). This clearly shows the ability of the various surfactants considered to modify the adsorption of diazonium ions. In addition, it implies that the functionalization process is extremely sensitive to the use of surfactants. In general, the theoretical framework developed here can also be utilized to model other surfactant types,  $i$ , SWCNT chiralities,  $(m,n)$ , and experimental conditions (e.g., SWCNT and diazonium salt concentrations, ionic strengths, pHs, and temperatures). This would require establishing a large database that contains  $K_A$  values as a function of  $i$  and  $(m,n)$  from simulations, as well as  $A$ ,  $\theta_{TA}$ , and  $K_R$  values as a function of  $i$  and  $(m,n)$  obtained by fitting the model to the available experimental data.

#### 4.4 Conclusions

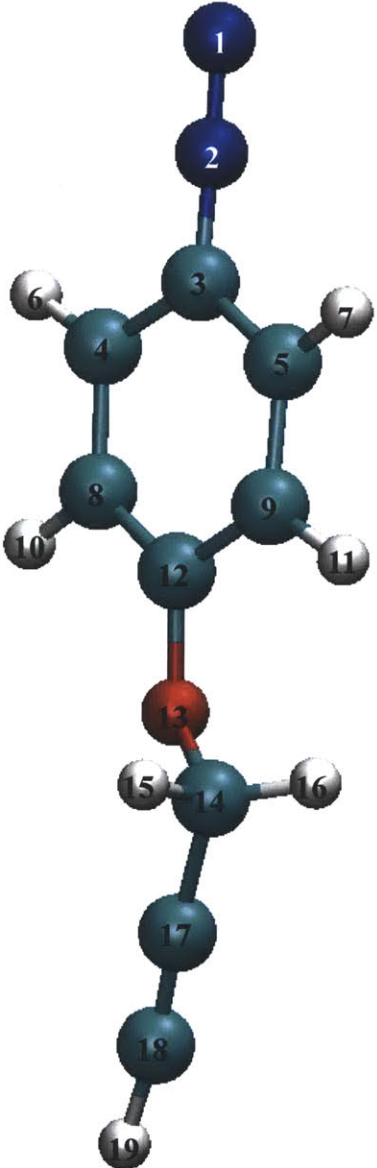
I combined molecular dynamics (MD) simulations, experiments, and equilibrium reaction modeling to both understand and model the extent of diazonium functionalization of SWCNTs coated with various surfactants. The free energy associated with diazonium adsorption determined from the PMF calculations using simulations can be used to rank surfactants in terms

of the extent of functionalization upon their decoration on the nanotube surface. The distinct binding affinities between linear and rigid surfactants were further investigated in detail, and attributed to the synergetic binding of the diazonium ion to the local “hot spots” formed by the accumulated, charged surfactant heads. Finally, a general theoretical framework was developed, which explicitly takes into account the reversibility of the diazonium reaction and the extensive diazonium adsorption on SWCNTs. This combined simulation-modeling framework can provide molecular-level information on quantities involved in the adsorption and reaction of diazonium ions with SWCNTs, which are very difficult to obtain or quantify through experiments. In addition, it can help understand the complex functionalization process, and guide the various sensitive experimental procedures to achieve the desired extent of SWCNT functionalization.

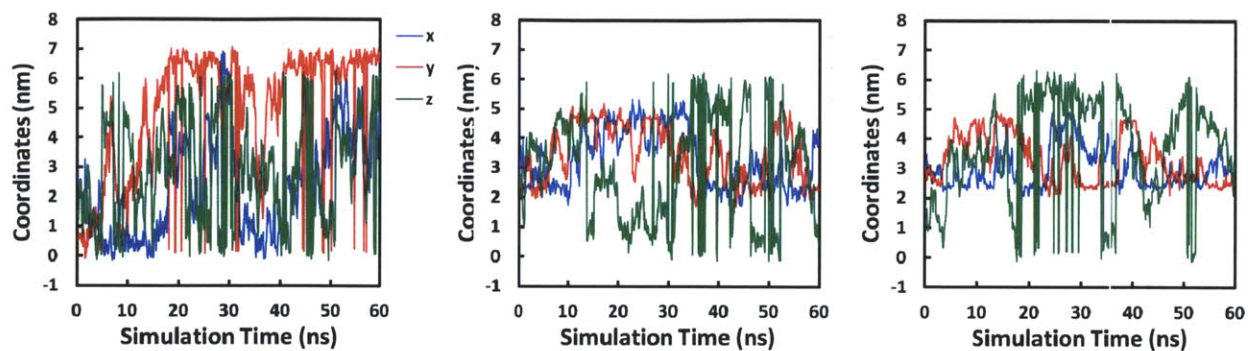
It is important to note that the theoretical framework presented here is not restricted to diazonium functionalization of SWCNTs, but can be extended, in general, to model solid surfaces (e.g., graphene,[73, 191] graphene oxide,[192, 193] silicon,[194] silica,[172, 195] metal,[194-196] metal oxide,[197] etc.) functionalized by any agent with complex molecular structures. The heterogeneous nature of many solid surfaces (e.g., those with surfactant/polymer coatings,[173, 198] having amorphous structures,[172, 193] or having random defects[199, 200]) can be modeled very well by molecular simulations. The proposed modeling framework that combines simulations with theoretical models can be utilized in a creative way to understand, at the molecular level, phenomena which involve physical adsorption, chemical adsorption, or both.[201, 202]

## 4.5 Appendix A: Supporting Tables and Figures

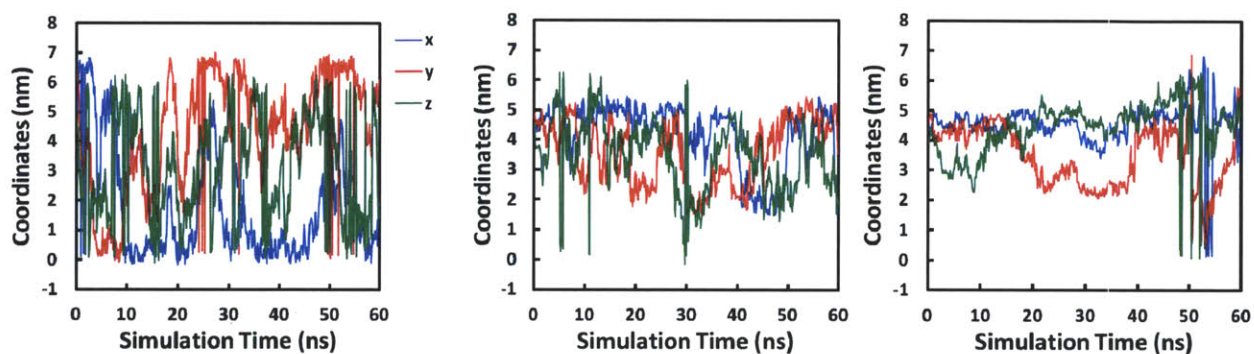
**Table 4-A1:** Partial atomic charges of the diazonium ion used in the molecular dynamics (MD) simulations. The color code for the diazonium ion chemical structure is the same as in Figure 4-2 in the main text. Note that charge symmetry was enforced to determine partial charges based on results from quantum mechanics (QM) calculations

Atom Number	Partial Charges (e)	Chemical Structure
1	0.032	
2	0.450	
3	-0.100	
4 and 5	-0.0085	
6 and 7	0.176	
8 and 9	-0.3045	
10 and 11	0.182	
12	0.579	
13	-0.442	
14	0.646	
15 and 16	-0.041	
17	-0.202	
18	-0.259	
19	0.288	

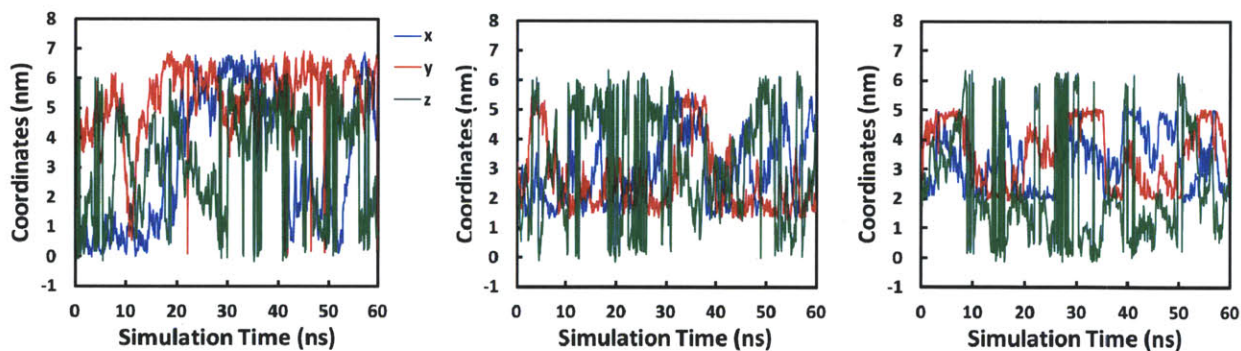




**a**



**b**



**c**

**Figure 4-A1:** Representative coordinates ( $x$ ,  $y$ , and  $z$ ) of the charged diazo group ( $-N^+\equiv N$ ) in the diazonium ion as a function of the simulation time for a: (a) SWCNT-SDS complex, (b) SWCNT-SC complex, and (c) SWCNT-CTAB complex. Left:  $r = 3.3$  nm, middle:  $r = 1.7$  nm, right:  $r = 1.1$  nm, corresponding to the density maps in Figure 4-4 in the main text. Note that  $z_{\max} \approx 6$  nm,  $x_{\max} = y_{\max} \approx 7$  nm, and the nanotube axis along the  $z$ -axis is located at  $x = y = 3.5$  nm.

## 4.6 Appendix B: Deconvolution of SWCNT Fluorescence Spectra

A custom-designed MATLAB program was used to determine the fluorescence emission peak center and intensity of each nanotube in an automated fashion (see Figure 4-A2 for representative SWCNT fluorescence spectra and spectra deconvolution). The fluorescence spectra were fitted using a sum of  $N = 9$  Lorentzian lineshapes (8 nanotube peaks and 1 G-prime peak). The fluorescence intensity at any energy,  $E$ , is a sum over the contributions of all the species present in solution:

$$I(E) = \sum_{i=1}^N \frac{C_i}{2\pi} \frac{\Gamma_i}{(E - E_{0,i})^2 + \Gamma_i^2/4}$$

The parameters to be estimated for the Lorentzian profile of the  $i^{\text{th}}$  entity are outlined below:

$C_i$  – area under the peak.

$\Gamma_i$  – full width at half maximum (FWHM, meV).

$E_{0,i}$  – peak center in terms of energy (meV).

Initial guesses for the peak areas were calculated from the control, or initial spectra. The area under the  $i^{\text{th}}$  peak was expressed as a fraction of the total area under the spectrum. This fraction was determined from the intensity of the peak in question. The FWHM and peak center for the G-prime peak were kept constant (11 meV and 1258.72 meV, respectively), and only its peak area was floated. In all, 31 parameters were used to fit a single fluorescence spectrum. Each  $\Gamma_i$  ( $E_{0,i}$ ) was constrained within a 10 meV (50 meV) window to maintain the physical validity of the fit. For responses for which the degree of quenching is over 50%, the shifting response is set to zero due to the difficulty in distinguishing between the actual shifting and relative intensity change of different species.

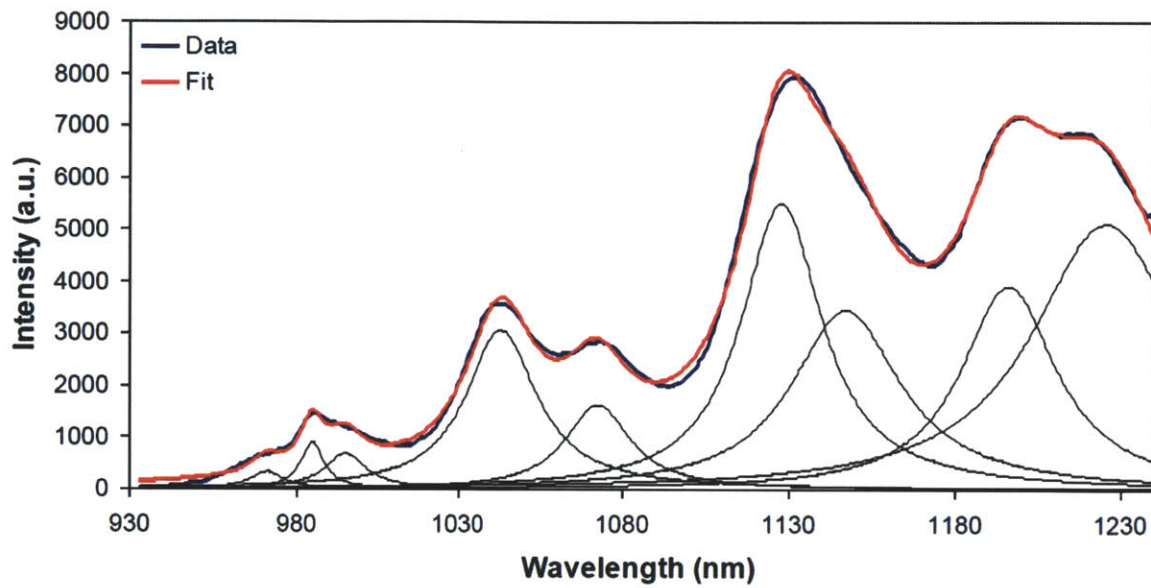


**Figure 4-A2:** Representative SWCNT fluorescence spectra and spectra deconvolution. The blue curve represents the original spectra data, the 9 black curves represent the deconvoluted spectra corresponding to  $N = 9$  Lorentzian lineshapes (8 nanotube peaks and 1 G-prime peak), and the red curve represents the fitted result (i.e., the summation of the 9 black curves) to the blue curve.

## Chapter 5

### Thesis Summary, Major Conclusions, and Future Work

#### 5.1 Thesis Summary and Major Conclusions

This thesis focuses primarily on combining molecular-level simulations, theoretical modeling, and experiments to help understand and design functional CNTs and graphene in aqueous surfactant solutions. In Chapters 2 and 3, the role of the anionic surfactant SC in dispersing SWCNTs and graphene sheets in aqueous solutions was investigated, respectively. In Chapter 4, the roles of various surfactants (SC (anionic), SDS (anionic), and CTAB (cationic)) in controlling the extent of functionalization of SWCNTs were investigated.

In Chapter 2, the surface structure of adsorbed SC molecules on the SWCNT surface was studied using MD simulations, and the interactions between two SWCNT-SC complexes were determined using PMF calculations. I found that the cholate ions wrap around the SWCNT like a ring and have a small tendency to orient perpendicular to the cylindrical axis of the SWCNT, a unique feature that has not been observed for conventional linear surfactants such as SDS. By comparing my simulated PMF profile of SC with the PMF profile of SDS reported in the literature, I found that, at the saturated surface coverages, SC is a better stabilizer than SDS, a finding that is consistent with the widespread use of SC to disperse SWNTs in aqueous media. Indeed, the superior dispersion-induced stability of SC over SDS results from a higher repulsive energy barrier and a shallower attractive energy well induced by SC in the PMF profile. In particular, I found that the shallower attractive energy well induced by SC is due to the rigid, bean-like structure of SC, which allows this bile salt surfactant to more effectively accommodate the intertube gap.

In Chapter 3, I first probed the surface structure and electrostatic potential of monolayer graphene dispersed in a SC aqueous solution, which exhibits 2D sheets partially covered with a

monolayer of negatively-charged cholate ions. Subsequently, I quantified the interactions between two graphene-SC assemblies by calculating the PMF between two SC-covered graphene sheets, which confirmed the existence of a metastable bilayer graphene structure due to the steric hindrance of the confined SC molecules. The traditional DLVO theory was found to be adequate to explain the long-range electrostatic repulsions between the anionic SC-covered graphene sheets, but was unable to account for the dominant, short-range steric hindrance imparted by the confined SC molecules. Interestingly, one faces a dilemma when using surfactants to disperse and stabilize graphene in aqueous solution: on the one hand, surfactants can stabilize graphene aqueous dispersions, but on the other hand, they prevent the formation of new AB-stacked bilayer and trilayer graphene resulting from the reaggregation process. Finally, the lifetime and time-dependent distribution of various graphene layer types were predicted using a kinetic model of colloid aggregation, and each graphene layer type was further decomposed into subtypes, including the AB-stacked species and various turbostratic species.

In Chapter 4, I showed that the free energy of diazonium adsorption onto the SWCNT-surfactant complex, determined using PMF calculations, can be used to rank surfactants in terms of the extent of functionalization attained following their adsorption on the nanotube surface. The difference in binding affinities between linear and rigid surfactants was attributed to the synergistic binding of the diazonium ion to the local “hot/cold spots” formed by the charged surfactant heads. Specifically, positively-charged CTAB heads repel positively-charged diazonium ions (forming “cold spots”), which results in a smaller extent of functionalization. On the other hand, negatively-charged SC and SDS heads attract positively-charged diazonium ions (forming “hot spots”), which results in larger extents of functionalization. Furthermore, the flexible SDS molecules can rearrange themselves to form “hotter spots” more efficiently than the rigid SC molecules, which results in an even larger extent of functionalization. A combined simulation–modeling framework was developed to provide guidance for controlling the various sensitive experimental conditions needed to achieve the desired extent of SWCNT functionalization.

Three major conclusions can be drawn from this thesis, which may help advance the practical implementation of CNTs and graphene:

1. Many applications of CNTs and graphene involve carrying out complex chemical processes in an aqueous solution phase. As a result, the efficient stabilization of these hydrophobic nanomaterials in aqueous solutions is essential for their successful implementation in practical applications. Surfactants, being one of the most versatile aqueous dispersants (along with amphiphilic polymers), play a key role in accomplishing this goal. Molecular-level simulations of the type discussed in this thesis, which can be used to complement traditional continuum-based theories, provide an invaluable tool to investigate these nano-structured aqueous dispersions.
2. Surfactants non-covalently adsorb onto CNT and graphene surfaces to form small “islands” of aggregates, instead of distributing uniformly on these surfaces. Ionic surfactants can induce surface charges on the originally uncharged CNT and graphene surfaces, which can significantly alter the physical (e.g., aggregate and layering structures, electrophoretic mobility, and electron conductivity) and chemical properties (e.g., reactivity and functionality) of CNTs and graphene in aqueous solutions.[158, 173, 203, 204] The ability to *a priori* predict and control these properties using modeling of the type presented in this thesis is extremely valuable.
3. The dispersion stability of CNTs and graphene in aqueous surfactant solutions is determined by the surfactant molecular structure, the surfactant surface coverage on the CNT and graphene surfaces (controlled by the surfactant type and its bulk concentration), and the solution environment (e.g., pH, ionic strength, and temperature). As a result, optimizing dispersion stability represents a challenging undertaking which typically requires tedious and time-consuming tuning of these experimental variables.[38, 205] With this need in mind, simulation and modeling methodologies of the type presented in this thesis can be very useful in predicting and optimizing these experimental variables in order to minimize trial-and-error experimentation.

## 5.2 Future Work

Although this thesis has focused primarily on the ability of the bile salt surfactant, sodium cholate, to disperse and stabilize CNTs and graphene in aqueous solutions, additional surfactant types (including anionic, cationic, nonionic, zwitterionic, or polymeric surfactants) could be studied. As a natural continuation of the studies presented in Chapters 2 and 3, such studies could lead to the identification of interesting dispersion mechanisms which have not yet been identified. For example, other research groups have already begun to investigate new types of surfactants possessing aromatic ring structures ( $\pi$ -orbital) in terms of their ability to stabilize SWCNTs.[206] Their simulation results suggest that strong  $\pi$ - $\pi$  stacking between the surfactant molecules and the SWCNT surface can enhance the stability of aqueous SWCNT dispersions.

The surface coverages of the various surfactants considered in the MD simulations presented in Chapters 2, 3, and 4 were obtained from experimentally-estimated saturated surfactant surface coverages reported in the literature. A more robust theoretical estimation of the saturated surface coverage of each surfactant type is required to molecularly predict, and compare, the dispersion stability induced by different surfactants. This estimation is theoretically challenging due to restrictions on simulation time and size, and can be presently handled solely using coarse-grained (CG) force fields. It is noteworthy, that the CG method was recently utilized to predict adsorption isotherms of model, “toy” surfactants on CNTs.[207] Together with my colleague Chih-Jen Shi (a member of the Blankschtein and Strano groups), we are utilizing the MARTINI CG force field[208] to simulate the adsorption isotherm of SC molecules on SWCNT and graphene surfaces.

In addition to MD simulations, other microscopic modeling and simulation techniques can be utilized to model the adsorption of surfactants or polymers on cylindrical (CNT) or flat (graphene) surfaces, including modeling the resulting dispersion stability. These techniques include, but are not limited to, self-consistent-field (SCF) theory,[209, 210] statistical-mechanics based density functional theory (DFT),[122, 211] single-chain mean-field theory,[121, 212] and Monte Carlo (MC) simulations.[213] The implementation of these techniques requires the

estimation of microscopic material properties as input parameters, which could lead to inaccuracies in the predictions made, including losing atomistic resolution of the model system. Nevertheless, the advantage of these techniques is that they can be implemented numerically within a much shorter time frame, although the size of the system considered is quite unlimited. As such, these techniques should be viewed as complementary, along with macroscopic continuum-based theories, to MD simulations for the purpose of formulating a multi-scale computational framework to study other nanoscale systems of interest.

The study in Chapter 4 on modeling functionalization of SWCNT-surfactant complexes with diazonium salts can be readily extended to model functionalization of graphene-surfactant complexes. Relevant experimental studies on graphene functionalization are already being carried out by my colleague Chih-Jen Shih. In addition, the impact of other surfactant types (nonionic or polymeric), as well as of reagents other than the diazonium salt considered in this thesis, on the functionalization of various interesting solid surfaces (including graphene,[73, 191] graphene oxide,[192, 193] silicon,[194] silica,[172, 195] metal,[194-196] metal oxide,[197] etc.) could also be investigated theoretically using the type of modeling approaches presented in this thesis.

As a natural continuation of the study reported in Chapter 4, reactive MD simulations (e.g., using the well-known reactive force field, ReaxFF[214]) can be utilized to study chemical reactions (or covalent adsorptions) of reagents onto CNT and graphene surfaces. This can be combined with classical MD simulations of the type implemented in this thesis to model physical adsorption, chemical adsorption, or both. The advantage of reactive MD simulations over quantum mechanics (QM) simulations for the purpose of modeling chemical reactions is that the former can handle larger systems in aqueous environments with a reasonable accuracy and within a shorter time frame, while the latter has system-size restrictions and can be very time consuming.

Finally, surfactant/polymer-decorated or covalently-functionalized CNTs and graphene can serve as novel functional building blocks for a wide range of nanotechnology applications, which include but are not limited to, highly-selective and highly-sensitive molecular sensors,[81, 215,



216] field-effect transistors for electronic devices,[16, 67, 139] electrodes for solar cells, fuel cells, or batteries,[217-219] and fillers for nanocomposites with promising mechanical, thermal, and electronic properties.[220-222] There is ample opportunity and need for theoretical studies (modeling and simulations) in these emerging areas to understand and design these nanoscale materials for various energy, environmental, and biomedical applications. As reflected in this thesis, active dialogue and close collaboration between modelers and experimentalists can facilitate construction of the intellectual bridge which connects theory with practical applications.

## Bibliography

1. M. Endo, S. Iijima, and M.S. Dresselhaus, *Carbon nanotubes*. 1st ed 1996, Oxford ; Tarrytown, N.Y.: Pergamon. x, 183 p.
2. Z. Xu, *Graphene : properties, synthesis, and applications* 2011, Hauppauge, N.Y.: Nova Science Publishers.
3. S. Iijima, *Helical Microtubules of Graphitic Carbon*. Nature, 1991. **354**(6348): p. 56-58.
4. B.H. Hong, J.Y. Lee, T. Beetz, Y.M. Zhu, P. Kim, and K.S. Kim, *Quasi-continuous growth of ultralong carbon nanotube arrays*. Journal of the American Chemical Society, 2005. **127**(44): p. 15336-15337.
5. M.F. Yu, B.S. Files, S. Arepalli, and R.S. Ruoff, *Tensile loading of ropes of single wall carbon nanotubes and their mechanical properties*. Physical Review Letters, 2000. **84**(24): p. 5552-5555.
6. A. Peigney, *Composite materials: Tougher ceramics with nanotubes*. Nature Materials, 2003. **2**(1): p. 15-16.
7. J.W.G. Wildoer, L.C. Venema, A.G. Rinzler, R.E. Smalley, and C. Dekker, *Electronic structure of atomically resolved carbon nanotubes*. Nature, 1998. **391**(6662): p. 59-62.
8. H. Kataura, Y. Kumazawa, Y. Maniwa, I. Umez, S. Suzuki, Y. Ohtsuka, and Y. Achiba, *Optical properties of single-wall carbon nanotubes*. Synthetic Metals, 1999. **103**(1-3): p. 2555-2558.
9. Y. Chen, R.C. Haddon, S. Fang, A.M. Rao, W.H. Lee, E.C. Dickey, E.A. Grulke, J.C. Pendergrass, A. Chavan, B.E. Haley, and R.E. Smalley, *Chemical attachment of organic functional groups to single-walled carbon nanotube material*. Journal of Materials Research, 1998. **13**(9): p. 2423-2431.
10. R.H. Baughman, A.A. Zakhidov, and W.A. de Heer, *Carbon nanotubes - the route toward applications*. Science, 2002. **297**(5582): p. 787-792.
11. R.R. Johnson, *Probing the Structure and Function of Biopolymer-Carbon Nanotube Hybrids with Molecular Dynamics*. Publicly Accessible Penn Dissertations, 2009.
12. M.C. Hersam, *Progress towards monodisperse single-walled carbon nanotubes*. Nature Nanotechnology, 2008. **3**(7): p. 387-394.
13. K.S. Novoselov, A.K. Geim, S.V. Morozov, D. Jiang, Y. Zhang, S.V. Dubonos, I.V. Grigorieva, and A.A. Firsov, *Electric field effect in atomically thin carbon films*. Science, 2004. **306**(5296): p. 666-669.

14. K.S. Novoselov, D. Jiang, F. Schedin, T.J. Booth, V.V. Khotkevich, S.V. Morozov, and A.K. Geim, *Two-dimensional atomic crystals*. Proceedings of the National Academy of Sciences of the United States of America, 2005. **102**(30): p. 10451-10453.
15. A.K. Geim and K.S. Novoselov, *The rise of graphene*. Nature Materials, 2007. **6**(3): p. 183-191.
16. F. Schwierz, *Graphene transistors*. Nature Nanotechnology, 2010. **5**(7): p. 487-496.
17. T. Ohta, A. Bostwick, T. Seyller, K. Horn, and E. Rotenberg, *Controlling the electronic structure of bilayer graphene*. Science, 2006. **313**(5789): p. 951-954.
18. S.Y. Zhou, G.H. Gweon, A.V. Fedorov, P.N. First, W.A. De Heer, D.H. Lee, F. Guinea, A.H.C. Neto, and A. Lanzara, *Substrate-induced bandgap opening in epitaxial graphene*. Nature Materials, 2007. **6**(11): p. 916-916.
19. Y.B. Zhang, T.T. Tang, C. Girit, Z. Hao, M.C. Martin, A. Zettl, M.F. Crommie, Y.R. Shen, and F. Wang, *Direct observation of a widely tunable bandgap in bilayer graphene*. Nature, 2009. **459**(7248): p. 820-823.
20. M.F. Craciun, S. Russo, M. Yamamoto, J.B. Oostinga, A.F. Morpurgo, and S. Thruha, *Trilayer graphene is a semimetal with a gate-tunable band overlap*. Nature Nanotechnology, 2009. **4**(6): p. 383-388.
21. Wikipedia, <http://en.wikipedia.org/wiki/Graphene>.
22. <http://nanopatentsandinnovations.blogspot.com/2010/02/aa-stacked-graphene-manufactured-by.html>.
23. A.A. Green and M.C. Hersam, *Emerging Methods for Producing Monodisperse Graphene Dispersions*. Journal of Physical Chemistry Letters, 2010. **1**(2): p. 544-549.
24. K.V. Emtsev, A. Bostwick, K. Horn, J. Jobst, G.L. Kellogg, L. Ley, J.L. McChesney, T. Ohta, S.A. Reshanov, J. Rohrl, E. Rotenberg, A.K. Schmid, D. Waldmann, H.B. Weber, and T. Seyller, *Towards wafer-size graphene layers by atmospheric pressure graphitization of silicon carbide*. Nature Materials, 2009. **8**(3): p. 203-207.
25. A. Reina, X.T. Jia, J. Ho, D. Nezich, H.B. Son, V. Bulovic, M.S. Dresselhaus, and J. Kong, *Large Area, Few-Layer Graphene Films on Arbitrary Substrates by Chemical Vapor Deposition*. Nano Letters, 2009. **9**(1): p. 30-35.
26. X.S. Li, W.W. Cai, J.H. An, S. Kim, J. Nah, D.X. Yang, R. Piner, A. Velamakanni, I. Jung, E. Tutuc, S.K. Banerjee, L. Colombo, and R.S. Ruoff, *Large-Area Synthesis of High-Quality and Uniform Graphene Films on Copper Foils*. Science, 2009. **324**(5932): p. 1312-1314.
27. K.S. Kim, Y. Zhao, H. Jang, S.Y. Lee, J.M. Kim, K.S. Kim, J.H. Ahn, P. Kim, J.Y. Choi, and B.H.

- Hong, *Large-scale pattern growth of graphene films for stretchable transparent electrodes*. Nature, 2009. 457(7230): p. 706-710.
28. S. Bae, H. Kim, Y. Lee, X.F. Xu, J.S. Park, Y. Zheng, J. Balakrishnan, T. Lei, H.R. Kim, Y.I. Song, Y.J. Kim, K.S. Kim, B. Ozyilmaz, J.H. Ahn, B.H. Hong, and S. Iijima, *Roll-to-roll production of 30-inch graphene films for transparent electrodes*. Nature Nanotechnology, 2010. 5(8): p. 574-578.
  29. A.H. Castro Neto, F. Guinea, N.M.R. Peres, K.S. Novoselov, and A.K. Geim, *The electronic properties of graphene*. Reviews of Modern Physics, 2009. 81(1): p. 109.
  30. C. Tanford, *The hydrophobic effect: formation of micelles and biological membranes*. 2nd ed1991, Malabar: Krieger.
  31. P.C. Hiemenz and R. Rajagopalan, *Principles of colloid and surface chemistry*. 3rd ed1997, New York: Marcel Dekker.
  32. J.N. Israelachvili, *Intermolecular and surface forces*. 3rd ed2011, Burlington, MA: Academic Press.
  33. P.H. Elworthy, A.T. Florence, and C.B. Macfarlane, *Solubilization by surface-active agents and its applications in chemistry and the biological sciences*1968, London,: Chapman & Hall. 335 p.
  34. S.D. Christian and J.F. Scamehorn, *Solubilization in surfactant aggregates*. Surfactant science series1995, New York: M. Dekker. xiii, 545 p.
  35. S.A. Hagan, A.G.A. Coombes, M.C. Garnett, S.E. Dunn, M.C. Davis, L. Illum, S.S. Davis, S.E. Harding, S. Purkiss, and P.R. Gellert, *Poly(lactide-poly(ethylene glycol) copolymers as drug delivery systems .1. Characterization of water dispersible micelle-forming systems*. Langmuir, 1996. 12(9): p. 2153-2161.
  36. Z.K. Zhao, C.G. Bi, Z.S. Li, W.H. Qiao, and L.B. Cheng, *Interfacial tension between crude oil and decylmethylnaphthalene sulfonate surfactant alkali-free flooding systems*. Colloids and Surfaces a-Physicochemical and Engineering Aspects, 2006. 276(1-3): p. 186-191.
  37. Z.K. Zhao, F. Liu, W.H. Qiao, Z.S. Li, and L.B. Cheng, *Novel alkyl methylnaphthalene sulfonate surfactants: A good candidate for enhanced oil recovery*. Fuel, 2006. 85(12-13): p. 1815-1820.
  38. V.C. Moore, M.S. Strano, E.H. Haroz, R.H. Hauge, R.E. Smalley, J. Schmidt, and Y. Talmon, *Individually suspended single-walled carbon nanotubes in various surfactants*. Nano Letters, 2003. 3(10): p. 1379-1382.
  39. M.S. Arnold, A.A. Green, J.F. Hulvat, S.I. Stupp, and M.C. Hersam, *Sorting carbon nanotubes by electronic structure using density differentiation*. Nature Nanotechnology, 2006. 1(1): p. 60-65.
  40. A.A. Green and M.C. Hersam, *Solution Phase Production of Graphene with Controlled Thickness*

via *Density Differentiation*. *Nano Letters*, 2009. **9**(12): p. 4031-4036.

41. L. Yurlova, A. Kryvoruchko, and B. Kornilovich, *Removal of Ni(II) ions from wastewater by micellar-enhanced ultrafiltration*. *Desalination*, 2002. **144**(1-3): p. 255-260.
42. T. Polubesova, S. Nir, D. Zadaka, O. Rabinovitz, C. Serban, L. Groisman, and B. Rubin, *Water purification from organic pollutants by optimized micelle-clay systems*. *Environmental Science & Technology*, 2005. **39**(7): p. 2343-2348.
43. J.N. Coleman, *Liquid-Phase Exfoliation of Nanotubes and Graphene*. *Advanced Functional Materials*, 2009. **19**(23): p. 3680-3695.
44. C. Richard, F. Balavoine, P. Schultz, T.W. Ebbesen, and C. Mioskowski, *Supramolecular self-assembly of lipid derivatives on carbon nanotubes*. *Science*, 2003. **300**(5620): p. 775-778.
45. M. Lotya, Y. Hernandez, P.J. King, R.J. Smith, V. Nicolosi, L.S. Karlsson, F.M. Blighe, S. De, Z.M. Wang, I.T. McGovern, G.S. Duesberg, and J.N. Coleman, *Liquid Phase Production of Graphene by Exfoliation of Graphite in Surfactant/Water Solutions*. *Journal of the American Chemical Society*, 2009. **131**(10): p. 3611-3620.
46. J.A. Zheng, C.A. Di, Y.Q. Liu, H.T. Liu, Y.L. Guo, C.Y. Du, T. Wu, G. Yu, and D.B. Zhu, *High quality graphene with large flakes exfoliated by oleyl amine*. *Chemical Communications*, 2010. **46**(31): p. 5728-5730.
47. M. Zheng, A. Jagota, M.S. Strano, A.P. Santos, P. Barone, S.G. Chou, B.A. Diner, M.S. Dresselhaus, R.S. McLean, G.B. Onoa, G.G. Samsonidze, E.D. Semke, M. Usrey, and D.J. Walls, *Structure-based carbon nanotube sorting by sequence-dependent DNA assembly*. *Science*, 2003. **302**(5650): p. 1545-1548.
48. X. Tu, S. Manohar, A. Jagota, and M. Zheng, *DNA sequence motifs for structure-specific recognition and separation of carbon nanotubes*. *Nature*, 2009. **460**(7252): p. 250-253.
49. W.-J. Kim, M.L. Usrey, and M.S. Strano, *Selective Functionalization and Free Solution Electrophoresis of Single-Walled Carbon Nanotubes: Separate Enrichment of Metallic and Semiconducting SWNT*. *Chemistry of Materials*, 2007. **19**(7): p. 1571-1576.
50. S. Park and R.S. Ruoff, *Chemical methods for the production of graphenes*. *Nature Nanotechnology*, 2009. **4**(4): p. 217-224.
51. S. Niyogi, E. Bekyarova, M.E. Itkis, J.L. McWilliams, M.A. Hamon, and R.C. Haddon, *Solution properties of graphite and graphene*. *Journal of the American Chemical Society*, 2006. **128**(24): p. 7720-7721.
52. S. Stankovich, D.A. Dikin, R.D. Piner, K.A. Kohlhaas, A. Kleinhammes, Y. Jia, Y. Wu, S.T. Nguyen,

- and R.S. Ruoff, *Synthesis of graphene-based nanosheets via chemical reduction of exfoliated graphite oxide*. Carbon, 2007. **45**(7): p. 1558-1565.
53. D. Li, M.B. Muller, S. Gilje, R.B. Kaner, and G.G. Wallace, *Processable aqueous dispersions of graphene nanosheets*. Nature Nanotechnology, 2008. **3**(2): p. 101-105.
  54. V.C. Tung, M.J. Allen, Y. Yang, and R.B. Kaner, *High-throughput solution processing of large-scale graphene*. Nature Nanotechnology, 2009. **4**(1): p. 25-29.
  55. C. Gomez-Navarro, J.C. Meyer, R.S. Sundaram, A. Chuvilin, S. Kurasch, M. Burghard, K. Kern, and U. Kaiser, *Atomic Structure of Reduced Graphene Oxide*. Nano Letters, 2010. **10**(4): p. 1144-1148.
  56. A. Bagri, C. Mattevi, M. Acik, Y.J. Chabal, M. Chhowalla, and V.B. Shenoy, *Structural evolution during the reduction of chemically derived graphene oxide*. Nature Chemistry, 2010. **2**(7): p. 581-587.
  57. H.A. Becerril, J. Mao, Z. Liu, R.M. Stoltenberg, Z. Bao, and Y. Chen, *Evaluation of solution-processed reduced graphene oxide films as transparent conductors*. Acs Nano, 2008. **2**(3): p. 463-470.
  58. P. Blake, P.D. Brimicombe, R.R. Nair, T.J. Booth, D. Jiang, F. Schedin, L.A. Ponomarenko, S.V. Morozov, H.F. Gleeson, E.W. Hill, A.K. Geim, and K.S. Novoselov, *Graphene-based liquid crystal device*. Nano Letters, 2008. **8**(6): p. 1704-1708.
  59. Y. Hernandez, V. Nicolosi, M. Lotya, F.M. Blighe, Z.Y. Sun, S. De, I.T. McGovern, B. Holland, M. Byrne, Y.K. Gun'ko, J.J. Boland, P. Niraj, G. Duesberg, S. Krishnamurthy, R. Goodhue, J. Hutchison, V. Scardaci, A.C. Ferrari, and J.N. Coleman, *High-yield production of graphene by liquid-phase exfoliation of graphite*. Nature Nanotechnology, 2008. **3**(9): p. 563-568.
  60. A. Vijayaraghavan, C. Sciascia, S. Dehm, A. Lombardo, A. Bonetti, A.C. Ferrari, and R. Krupke, *Dielectrophoretic Assembly of High-Density Arrays of Individual Graphene Devices for Rapid Screening*. Acs Nano, 2009. **3**(7): p. 1729-1734.
  61. J.M. Schnorr and T.M. Swager, *Emerging Applications of Carbon Nanotubes*. Chemistry of Materials, 2011. **23**(3): p. 646-657.
  62. K. Kostarelos, A. Bianco, and M. Prato, *Promises, facts and challenges for carbon nanotubes in imaging and therapeutics*. Nature Nanotechnology, 2009. **4**(10): p. 627-633.
  63. Y. Lin, F. Lu, Y. Tu, and Z. Ren, *Glucose Biosensors Based on Carbon Nanotube Nanoelectrode Ensembles*. Nano Letters, 2003. **4**(2): p. 191-195.
  64. H. Cai, X. Cao, Y. Jiang, P. He, and Y. Fang, *Carbon nanotube-enhanced electrochemical DNA*

- biosensor for DNA hybridization detection*. Analytical and Bioanalytical Chemistry, 2003. 375(2): p. 287-293.
65. P. Zhao, C.F. Fang, Y.M. Wang, Y.X. Zhai, and D.S. Liu, *First-principles study of the switching characteristics of the phenoxynaphthacenequinone-based optical molecular switch with carbon nanotube electrodes*. Physica E: Low-dimensional Systems and Nanostructures, 2009. 41(3): p. 474-478.
  66. X.F. Li, L.L. Wang, K.Q. Chen, and Y. Luo, *Nanomechanically induced molecular conductance switch*. Applied Physics Letters, 2009. 95(23): p. 232118.
  67. S. Sorgenfrei, C.-y. Chiu, R.L. Gonzalez, Y.-J. Yu, P. Kim, C. Nuckolls, and K.L. Shepard, *Label-free single-molecule detection of DNA-hybridization kinetics with a carbon nanotube field-effect transistor*. Nature Nanotechnology, 2011. 6(2): p. 126-132.
  68. B.R. Goldsmith, J.G. Coroneus, V.R. Khalap, A.A. Kane, G.A. Weiss, and P.G. Collins, *Conductance-Controlled Point Functionalization of Single-Walled Carbon Nanotubes*. Science, 2007. 315(5808): p. 77-81.
  69. L. Cognet, D.A. Tsyboulski, J.D.R. Rocha, C.D. Doyle, J.M. Tour, and R.B. Weisman, *Stepwise quenching of exciton fluorescence in carbon nanotubes by single-molecule reactions*. Science, 2007. 316(5830): p. 1465-1468.
  70. A.J. Siitonen, D.A. Tsyboulski, S.M. Bachilo, and R.B. Weisman, *Surfactant-Dependent Exciton Mobility in Single-Walled Carbon Nanotubes Studied by Single-Molecule Reactions*. Nano Letters, 2010. 10(5): p. 1595-1599.
  71. E. Bekyarova, M.E. Itkis, P. Ramesh, C. Berger, M. Sprinkle, W.A. de Heer, and R.C. Haddon, *Chemical Modification of Epitaxial Graphene: Spontaneous Grafting of Aryl Groups*. Journal of the American Chemical Society, 2009. 131(4): p. 1336-1337.
  72. J.R. Lomeda, C.D. Doyle, D.V. Kosynkin, W.-F. Hwang, and J.M. Tour, *Diazonium Functionalization of Surfactant-Wrapped Chemically Converted Graphene Sheets*. Journal of the American Chemical Society, 2008. 130(48): p. 16201-16206.
  73. R. Sharma, J.H. Baik, C.J. Perera, and M.S. Strano, *Anomalously Large Reactivity of Single Graphene Layers and Edges toward Electron Transfer Chemistries*. Nano Letters, 2010. 10(2): p. 398-405.
  74. A.R. Leach, *Molecular modelling: principles and applications*. 2nd ed2001, Harlow, England ; New York: Prentice Hall.
  75. *GROMACS Online Manual*. <http://www.gromacs.org/Documentation/Manual>.

76. M.J. O'Connell, S.M. Bachilo, C.B. Huffman, V.C. Moore, M.S. Strano, E.H. Haroz, K.L. Rialon, P.J. Boul, W.H. Noon, C. Kittrell, J.P. Ma, R.H. Hauge, R.B. Weisman, and R.E. Smalley, *Band gap fluorescence from individual single-walled carbon nanotubes*. *Science*, 2002. **297**(5581): p. 593-596.
77. M.F. Islam, E. Rojas, D.M. Bergey, A.T. Johnson, and A.G. Yodh, *High weight fraction surfactant solubilization of single-wall carbon nanotubes in water*. *Nano Letters*, 2003. **3**(2): p. 269-273.
78. L. Vaisman, G. Marom, and H.D. Wagner, *Dispersions of surface-modified carbon nanotubes in water-soluble and water-insoluble polymers*. *Advanced Functional Materials*, 2006. **16**(3): p. 357-363.
79. M.S. Strano, V.C. Moore, M.K. Miller, M.J. Allen, E.H. Haroz, C. Kittrell, R.H. Hauge, and R.E. Smalley, *The role of surfactant adsorption during ultrasonication in the dispersion of single-walled carbon nanotubes*. *Journal of Nanoscience and Nanotechnology*, 2003. **3**(1-2): p. 81-86.
80. J. Kong, N.R. Franklin, C.W. Zhou, M.G. Chapline, S. Peng, K.J. Cho, and H.J. Dai, *Nanotube molecular wires as chemical sensors*. *Science*, 2000. **287**(5453): p. 622-625.
81. J.H. Kim, D.A. Heller, H. Jin, P.W. Barone, C. Song, J. Zhang, L.J. Trudel, G.N. Wogan, S.R. Tannenbaum, and M.S. Strano, *The rational design of nitric oxide selectivity in single-walled carbon nanotube near-infrared fluorescence sensors for biological detection*. *Nature Chemistry*, 2009. **1**(6): p. 473-481.
82. C.Y. Lee, R. Sharma, A.D. Radadia, R.I. Masel, and M.S. Strano, *On-chip micro gas chromatograph enabled by a noncovalently functionalized single-walled carbon nanotube sensor array*. *Angewandte Chemie-International Edition*, 2008. **47**(27): p. 5018-5021.
83. H. Wang, *Dispersing carbon nanotubes using surfactants*. *Current Opinion in Colloid & Interface Science*, 2009. **14**(5): p. 364-371.
84. O. Matarredona, H. Rhoads, Z.R. Li, J.H. Harwell, L. Balzano, and D.E. Resasco, *Dispersion of single-walled carbon nanotubes in aqueous solutions of the anionic surfactant NaDDBS*. *Journal of Physical Chemistry B*, 2003. **107**(48): p. 13357-13367.
85. W. Wenseleers, I.I. Vlasov, E. Goovaerts, E.D. Obratsova, A.S. Lobach, and A. Bouwen, *Efficient isolation and solubilization of pristine single-walled nanotubes in bile salt micelles*. *Advanced Functional Materials*, 2004. **14**(11): p. 1105-1112.
86. L.B. Partay, P. Jedlovsky, and M. Sega, *Molecular aggregates in aqueous solutions of bile acid salts. Molecular dynamics simulation study*. *Journal of Physical Chemistry B*, 2007. **111**(33): p. 9886-9896.



87. L.B. Partay, M. Sega, and P. Jedlovsky, *Counterion binding in the aqueous solutions of bile acid salts, as studied by computer simulation methods*. *Langmuir*, 2008. **24**(19): p. 10729-10736.
88. Q.H. Zhang, X.Q. Ma, A. Ward, W.X. Hong, V.P. Jaakola, R.C. Stevens, M.G. Finn, and G. Chang, *Designing facial amphiphiles for the stabilization of integral membrane proteins*. *Angewandte Chemie-International Edition*, 2007. **46**(37): p. 7023-7025.
89. M.S. Arnold, J. Suntivich, S.I. Stupp, and M.C. Hersam, *Hydrodynamic Characterization of Surfactant Encapsulated Carbon Nanotubes Using an Analytical Ultracentrifuge*. *ACS Nano*, 2008. **2**(11): p. 2291-2300.
90. M.L. Usrey, E.S. Lippmann, and M.S. Strano, *Evidence for a two-step mechanism in electronically selective single-walled carbon nanotube reactions*. *Journal of the American Chemical Society*, 2005. **127**(46): p. 16129-16135.
91. N.R. Tummala and A. Striolo, *SDS Surfactants on Carbon Nanotubes: Aggregate Morphology*. *ACS Nano*, 2009. **3**(3): p. 595-602.
92. N.R. Tummala and A. Striolo, *Curvature effects on the adsorption of aqueous sodium-dodecyl-sulfate surfactants on carbonaceous substrates: Structural features and counterion dynamics*. *Physical Review E*, 2009. **80**(2): p. 021408.
93. Z.J. Xu, X.N. Yang, and Z. Yang, *A Molecular Simulation Probing of Structure and Interaction for Supramolecular Sodium Dodecyl Sulfate/Single-Wall Carbon Nanotube Assemblies*. *Nano Letters*, 2010. **10**(3): p. 985-991.
94. R. Qiao and P.C. Ke, *Lipid-carbon nanotube self-assembly in aqueous solution*. *Journal of the American Chemical Society*, 2006. **128**(42): p. 13656-13657.
95. E.J. Wallace and M.S.P. Sansom, *Carbon nanotube/detergent interactions via coarse-grained molecular dynamics*. *Nano Letters*, 2007. **7**(7): p. 1923-1928.
96. E.J. Wallace and M.S.P. Sansom, *Carbon nanotube self-assembly with lipids and detergent: a molecular dynamics study*. *Nanotechnology*, 2009. **20**(4): p. 045101.
97. E.J.F. Carvalho and M.C. dos Santos, *Role of Surfactants in Carbon Nanotubes Density Gradient Separation*. *ACS Nano*, 2010. **4**(2): p. 765-770.
98. A. Quintilla, F. Hennrich, S. Lebedkin, M.M. Kappes, and W. Wenzel, *Influence of endohedral water on diameter sorting of single-walled carbon nanotubes by density gradient centrifugation*. *Physical Chemistry Chemical Physics*, 2010. **12**(4): p. 902-908.
99. J.N. Israelachvili, *Intermolecular and surface forces : with applications to colloidal and biological systems* 1985, London ; Orlando.: Academic Press.

100. J.M. Smith, H.C. Van Ness, and M.M. Abbott, *Introduction to chemical engineering thermodynamics*. 7th ed. McGraw-Hill chemical engineering series 2005, Boston: McGraw-Hill. xviii, 817 p.
101. N. Nair, W.J. Kim, R.D. Braatz, and M.S. Strano, *Dynamics of surfactant-suspended single-walled carbon nanotubes in a centrifugal field*. *Langmuir*, 2008. **24**(5): p. 1790-1795.
102. X.C. Zhang, J.K. Jackson, and H.M. Burt, *Determination of surfactant critical micelle concentration by a novel fluorescence depolarization technique*. *Journal of Biochemical and Biophysical Methods*, 1996. **31**(3-4): p. 145-150.
103. B. Hess, C. Kutzner, D. van der Spoel, and E. Lindahl, *GROMACS 4: Algorithms for highly efficient, load-balanced, and scalable molecular simulation*. *Journal of Chemical Theory and Computation*, 2008. **4**(3): p. 435-447.
104. N.R. Tummala and A. Striolo, *Role of counterion condensation in the self-assembly of SDS surfactants at the water-graphite interface*. *Journal of Physical Chemistry B*, 2008. **112**(7): p. 1987-2000.
105. H.J.C. Berendsen, J.R. Grigera, and T.P. Straatsma, *The Missing Term in Effective Pair Potentials*. *Journal of Physical Chemistry*, 1987. **91**(24): p. 6269-6271.
106. S. Miyamoto and P.A. Kollman, *Settle - an Analytical Version of the Shake and Rattle Algorithm for Rigid Water Models*. *Journal of Computational Chemistry*, 1992. **13**(8): p. 952-962.
107. W.L. Jorgensen, D.S. Maxwell, and J. Tirado-Rives, *Development and testing of the OPLS all-atom force field on conformational energetics and properties of organic liquids*. *Journal of the American Chemical Society*, 1996. **118**(45): p. 11225-11236.
108. B. Hess, H. Bekker, H.J.C. Berendsen, and J.G.E.M. Fraaije, *LINCS: A linear constraint solver for molecular simulations*. *Journal of Computational Chemistry*, 1997. **18**(12): p. 1463-1472.
109. B. Hess, *P-LINCS: A parallel linear constraint solver for molecular simulation*. *Journal of Chemical Theory and Computation*, 2008. **4**(1): p. 116-122.
110. T. Darden, D. York, and L. Pedersen, *Particle Mesh Ewald - an  $N \cdot \log(N)$  Method for Ewald Sums in Large Systems*. *Journal of Chemical Physics*, 1993. **98**(12): p. 10089-10092.
111. U. Essmann, L. Perera, M.L. Berkowitz, T. Darden, H. Lee, and L.G. Pedersen, *A Smooth Particle Mesh Ewald Method*. *Journal of Chemical Physics*, 1995. **103**(19): p. 8577-8593.
112. R.W. Hockney, S.P. Goel, and J.W. Eastwood, *Quiet High-Resolution Computer Models of a Plasma*. *Journal of Computational Physics*, 1974. **14**(2): p. 148-158.

113. L. Verlet, *Computer Experiments on Classical Fluids .I. Thermodynamical Properties of Lennard-Jones Molecules*. Physical Review, 1967. **159**(1): p. 98-103.
114. G. Bussi, D. Donadio, and M. Parrinello, *Canonical sampling through velocity rescaling*. Journal of Chemical Physics, 2007. **126**(1): p. 014101.
115. H.J.C. Berendsen, J.P.M. Postma, W.F. Vangunsteren, A. Dinola, and J.R. Haak, *Molecular-Dynamics with Coupling to an External Bath*. Journal of Chemical Physics, 1984. **81**(8): p. 3684-3690.
116. B.C. Stephenson, A. Goldsipe, K.J. Beers, and D. Blankschtein, *Quantifying the hydrophobic effect. 1. A computer simulation-molecular-thermodynamic model for the self-assembly of hydrophobic and amphiphilic solutes in aqueous solution*. Journal of Physical Chemistry B, 2007. **111**(5): p. 1025-1044.
117. F. Eisenhaber, P. Lijnzaad, P. Argos, C. Sander, and M. Scharf, *The Double Cubic Lattice Method - Efficient Approaches to Numerical-Integration of Surface-Area and Volume and to Dot Surface Contouring of Molecular Assemblies*. Journal of Computational Chemistry, 1995. **16**(3): p. 273-284.
118. B.C. Stephenson, A. Goldsipe, K.J. Beers, and D. Blankschtein, *Quantifying the hydrophobic effect. 2. A computer simulation-molecular-thermodynamic model for the micellization of nonionic surfactants in aqueous solution*. Journal of Physical Chemistry B, 2007. **111**(5): p. 1045-1062.
119. N.M. Uddin, F. Capaldi, and B. Farouk, *Molecular Dynamics Simulations of Carbon Nanotube Interactions in Water/Surfactant Systems*. Journal of Engineering Materials and Technology-Transactions of the ASME, 2010. **132**(2): p. 021012.
120. H. Flyvbjerg and H.G. Petersen, *Error-Estimates on Averages of Correlated Data*. Journal of Chemical Physics, 1989. **91**(1): p. 461-466.
121. R. Shvartzman-Cohen, E. Nativ-Roth, E. Baskaran, Y. Levi-Kalisman, I. Szleifer, and R. Yerushalmi-Rozen, *Selective dispersion of single-walled carbon nanotubes in the presence of polymers: the role of molecular and colloidal length scales*. Journal of the American Chemical Society, 2004. **126**(45): p. 14850-14857.
122. N. Patel and S.A. Egorov, *Dispersing nanotubes with surfactants: A microscopic statistical mechanical analysis*. Journal of the American Chemical Society, 2005. **127**(41): p. 14124-14125.
123. N. Fuchs, *Theory of coagulation*. Zeitschrift Fur Physikalische Chemie-Abteilung a-Chemische Thermodynamik Kinetik Elektrochemie Eigenschaftslehre, 1934. **171**(3/4): p. 199-208.
124. L.W. Li, D. Bedrov, and G.D. Smith, *Water-induced interactions between carbon nanoparticles*. Journal of Physical Chemistry B, 2006. **110**(21): p. 10509-10513.

125. F. Booth, *The Solution of Some Potential Problems in the Theory of Electrolytes*. Journal of Chemical Physics, 1951. **19**(7): p. 821-826.
126. D. Chapot, L. Bocquet, and E. Trizac, *Electrostatic potential around charged finite rodlike macromolecules: nonlinear Poisson-Boltzmann theory*. Journal of Colloid and Interface Science, 2005. **285**(2): p. 609-618.
127. As discussed in Ref. 29, the electrostatic repulsion between two charged parallel plates in the limit of small separations can be approximated as  $U_{elec} \propto \sigma \ln(d)$  based on the Poisson-Boltzmann equation, where  $\sigma$  is the effective surface charge density of the plates. In the case of surfactant-covered SWNTs, we have assumed that the linear dependence of  $U_{elec}$  on  $\sigma$  remains valid.
128. N. Grossiord, P. van der Schoot, J. Meuldijk, and C.E. Koning, *Determination of the surface coverage of exfoliated carbon nanotubes by surfactant molecules in aqueous solution*. Langmuir, 2007. **23**(7): p. 3646-3653.
129. A. Bandyopadhyay and S.P. Moulik, *Counterion Binding Behavior of Micelles of Sodium Dodecyl-Sulfate and Bile-Salts in the Pure State, in Mutually Mixed States and Mixed with a Nonionic Surfactant*. Colloid and Polymer Science, 1988. **266**(5): p. 455-461.
130. A.S. Khair and T.M. Squires, *Ion steric effects on electrophoresis of a colloidal particle*. Journal of Fluid Mechanics, 2009. **640**: p. 343-356.
131. Z. Hui, *On the Influence of Ion Excluded Volume (Steric) Effects on the Double-Layer Polarization of a Nonconducting Spherical Particle in an AC Field*. Journal of Physical Chemistry C, 2010. **114**(18): p. 8389-8397.
132. J.N. Israelachvili, *The Forces between Surfaces*. Philosophical Magazine a-Physics of Condensed Matter Structure Defects and Mechanical Properties, 1981. **43**(3): p. 753-770.
133. R.G. Horn and J.N. Israelachvili, *Direct Measurement of Structural Forces between 2 Surfaces in a Non-Polar Liquid*. Journal of Chemical Physics, 1981. **75**(3): p. 1400-1411.
134. J.N. Israelachvili, R.K. Tandon, and L.R. White, *Measurement of Forces between 2 Mica Surfaces in Aqueous Polyethylene Oxide Solution*. Journal of Colloid and Interface Science, 1980. **78**(2): p. 430-443.
135. R.M. Pashley and J.N. Israelachvili, *A Comparison of Surface Forces and Interfacial Properties of Mica in Purified Surfactant Solutions*. Colloids and Surfaces, 1981. **2**(2): p. 169-187.
136. C. Berger, Z.M. Song, X.B. Li, X.S. Wu, N. Brown, C. Naud, D. Mayou, T.B. Li, J. Hass, A.N. Marchenkov, E.H. Conrad, P.N. First, and W.A. de Heer, *Electronic confinement and coherence in*

- patterned epitaxial graphene*. *Science*, 2006. **312**(5777): p. 1191-1196.
137. Y. Hernandez, *High-yield production of graphene by liquid-phase exfoliation of graphite*. *Nature Nanotechnology*, 2008. **3**(9): p. 563-568.
  138. N. Mohanty and V. Berry, *Graphene-Based Single-Bacterium Resolution Biodevice and DNA Transistor: Interfacing Graphene Derivatives with Nanoscale and Microscale Biocomponents*. *Nano Letters*, 2008. **8**(12): p. 4469-4476.
  139. Y. Ohno, K. Maehashi, Y. Yamashiro, and K. Matsumoto, *Electrolyte-Gated Graphene Field-Effect Transistors for Detecting pH Protein Adsorption*. *Nano Letters*, 2009. **9**(9): p. 3318-3322.
  140. Z.G. Cheng, Q. Li, Z.J. Li, Q.Y. Zhou, and Y. Fang, *Suspended Graphene Sensors with Improved Signal and Reduced Noise*. *Nano Letters*, 2010. **10**(5): p. 1864-1868.
  141. M. Lotya, P.J. King, U. Khan, S. De, and J.N. Coleman, *High-Concentration, Surfactant-Stabilized Graphene Dispersions*. *ACS Nano*, 2010. **4**(6): p. 3155-3162.
  142. Y. Zhang, T.-T. Tang, C. Girit, Z. Hao, M.C. Martin, A. Zettl, M.F. Crommie, Y.R. Shen, and F. Wang, *Direct observation of a widely tunable bandgap in bilayer graphene*. *Nature*, 2009. **459**(7248): p. 820-823.
  143. C. Faugeras, A. Neri, M. Potemski, A. Mahmood, E. Dujardin, C. Berger, and W.A. de Heer, *Few-layer graphene on SiC, pyrolytic graphite, and graphene: A Raman scattering study*. *Applied Physics Letters*, 2008. **92**(1): p. 011914.
  144. J.M.B.L. dos Santos, N.M.R. Peres, and A.H. Castro, *Graphene bilayer with a twist: Electronic structure*. *Physical Review Letters*, 2007. **99**(25): p. 256802.
  145. M.S. Dresselhaus and G. Dresselhaus, *Intercalation Compounds of Graphite*. *Advances in Physics*, 1981. **30**(2): p. 139-326.
  146. X.L. Li, G.Y. Zhang, X.D. Bai, X.M. Sun, X.R. Wang, E. Wang, and H.J. Dai, *Highly conducting graphene sheets and Langmuir-Blodgett films*. *Nature Nanotechnology*, 2008. **3**(9): p. 538-542.
  147. P.K. Ang, S. Wang, Q.L. Bao, J.T.L. Thong, and K.P. Loh, *High-Throughput Synthesis of Graphene by Intercalation - Exfoliation of Graphite Oxide and Study of Ionic Screening in Graphene Transistor*. *ACS Nano*, 2009. **3**(11): p. 3587-3594.
  148. J.H. Lee, D.W. Shin, V.G. Makotchenko, A.S. Nazarov, V.E. Fedorov, Y.H. Kim, J.Y. Choi, J.M. Kim, and J.B. Yoo, *One-Step Exfoliation Synthesis of Easily Soluble Graphite and Transparent Conducting Graphene Sheets*. *Advanced Materials*, 2009. **21**(43): p. 1-5.
  149. X.L. Li, X.R. Wang, L. Zhang, S.W. Lee, and H.J. Dai, *Chemically derived, ultrasmooth graphene*

- nanoribbon semiconductors*. Science, 2008. 319(5867): p. 1229-1232.
150. N. Behabtu, J.R. Lomeda, M.J. Green, A.L. Higginbotham, A. Sinitskii, D.V. Kosynkin, D. Tsentelovich, A.N.G. Parra-Vasquez, J. Schmidt, E. Kesselman, Y. Cohen, Y. Talmon, J.M. Tour, and M. Pasquali, *Spontaneous high-concentration dispersions and liquid crystals of graphene*. Nature Nanotechnology, 2010. 5(6): p. 406-411.
  151. J.H. Lee, D.W. Shin, V.G. Makotchenko, A.S. Nazarov, V.E. Fedorov, J.H. Yoo, S.M. Yu, J.Y. Choi, J.M. Kim, and J.B. Yoo, *The Superior Dispersion of Easily Soluble Graphite*. Small, 2010. 6(1): p. 58-62.
  152. C.-J. Shih, A. Vijayaraghavan, R. Krishnan, R. Sharma, J.-H. Han, M.-H. Ham, Z. Jin, S. Lin, G.L.C. Paulus, N.F. Reuel, Q.H. Wang, D. Blankshtein, and M.S. Strano, *Bi- and trilayer graphene solutions*. Nature Nanotechnology, 2011. 6(7): p. 439-445.
  153. J.R. Lomeda, C.D. Doyle, D.V. Kosynkin, W.F. Hwang, and J.M. Tour, *Diazonium Functionalization of Surfactant-Wrapped Chemically Converted Graphene Sheets*. Journal of the American Chemical Society, 2008. 130(48): p. 16201-16206.
  154. N. Nair, W.J. Kim, M.L. Usrey, and M.S. Strano, *A structure-reactivity relationship for single walled carbon nanotubes reacting with 4-hydroxybenzene diazonium salt*. Journal of the American Chemical Society, 2007. 129(13): p. 3946-3954.
  155. M. Sammalkorpi, A.Z. Panagiotopoulos, and M. Haataja, *Structure and dynamics of surfactant and hydrocarbon aggregates on graphite: A molecular dynamics simulation study*. Journal of Physical Chemistry B, 2008. 112(10): p. 2915-2921.
  156. C.-J. Shih, S. Lin, M.S. Strano, and D. Blankshtein, *Understanding the Stabilization of Liquid-Phase-Exfoliated Graphene in Polar Solvents: Molecular Dynamics Simulations and Kinetic Theory of Colloid Aggregation*. Journal of the American Chemical Society, 2010. 132(41): p. 14638-14648.
  157. A. Cheng and W.A. Steele, *Computer-Simulation of Ammonia on Graphite .1. Low-Temperature Structure of Monolayer and Bilayer Films*. Journal of Chemical Physics, 1990. 92(6): p. 3858-3866.
  158. S. Lin and D. Blankshtein, *Role of the Bile Salt Surfactant Sodium Cholate in Enhancing the Aqueous Dispersion Stability of Single-Walled Carbon Nanotubes: A Molecular Dynamics Simulation Study*. The Journal of Physical Chemistry B, 2010. 114(47): p. 15616-15625.
  159. Y. Sasaki, H.D. Nagata, Y.K. Fujii, S. Lee, S. Nagadome, and G. Sugihara, *A thermodynamic study on the adsorption behavior of four bile salt species on graphite in water*. Colloids and Surfaces B-Biointerfaces, 1997. 9(3-4): p. 169-176.

160. J.N. Israelachvili, *Intermolecular and surface forces* 1991, London: Academic Press. 213-246.
161. A.A. Gurtovenko and I. Vattulainen, *Calculation of the electrostatic potential of lipid bilayers from molecular dynamics simulations: Methodological issues*. *Journal of Chemical Physics*, 2009. **130**(21): p. 215107.
162. J.D. Ingle and S.R. Crouch, *Spectrochemical analysis* 1988, Englewood Cliffs, N.J.: Prentice Hall.
163. N. Choudhury and B.M. Pettitt, *On the mechanism of hydrophobic association of nanoscopic solutes*. *Journal of the American Chemical Society*, 2005. **127**(10): p. 3556-3567.
164. V. Knecht, H.J. Risselada, A.E. Mark, and S.J. Marrink, *Electrophoretic mobility does not always reflect the charge on an oil droplet*. *Journal of Colloid and Interface Science*, 2008. **318**(2): p. 477-486.
165. R.J. Smith, M. Lotya, and J.N. Coleman, *The importance of repulsive potential barriers for the dispersion of graphene using surfactants*. *New Journal of Physics*, 2010. **12**: p. 125008.
166. J.W.T. Seo, A.A. Green, A.L. Antaris, and M.C. Hersam, *High-Concentration Aqueous Dispersions of Graphene Using Nonionic, Biocompatible Block Copolymers*. *Journal of Physical Chemistry Letters*, 2011. **2**(9): p. 1004-1008.
167. R.D. Deegan, O. Bakajin, T.F. Dupont, G. Huber, S.R. Nagel, and T.A. Witten, *Capillary flow as the cause of ring stains from dried liquid drops*. *Nature*, 1997. **389**(6653): p. 827-829.
168. A.C. Ferrari, J.C. Meyer, V. Scardaci, C. Casiraghi, M. Lazzeri, F. Mauri, S. Piscanec, D. Jiang, K.S. Novoselov, S. Roth, and A.K. Geim, *Raman spectrum of graphene and graphene layers*. *Physical Review Letters*, 2006. **97**(18): p. 187401.
169. F.E. Regnier and K.M. Gooding, *High-Performance Liquid-Chromatography of Proteins*. *Analytical Biochemistry*, 1980. **103**(1): p. 1-25.
170. L. Movileanu, D.J. Niedzwiecki, and J. Grazul, *Single-Molecule Observation of Protein Adsorption onto an Inorganic Surface*. *Journal of the American Chemical Society*, 2010. **132**(31): p. 10816-10822.
171. J.O. Tegenfeldt, C. Prinz, H. Cao, R.L. Huang, R.H. Austin, S.Y. Chou, E.C. Cox, and J.C. Sturm, *Micro- and nanofluidics for DNA analysis*. *Analytical and Bioanalytical Chemistry*, 2004. **378**(7): p. 1678-1692.
172. R. Carr, J. Comer, M.D. Ginsberg, and A. Aksimentiev, *Microscopic Perspective on the Adsorption Isotherm of a Heterogeneous Surface*. *Journal of Physical Chemistry Letters*, 2011. **2**(14): p. 1804-1807.

173. S. Lin, C.-J. Shih, M.S. Strano, and D. Blankschtein, *Molecular Insights into the Surface Morphology, Layering Structure, and Aggregation Kinetics of Surfactant-Stabilized Graphene Dispersions*. *Journal of the American Chemical Society*, 2011. **133**(32): p. 12810-12823.
174. M.S. Strano, C.A. Dyke, M.L. Usrey, P.W. Barone, M.J. Allen, H.W. Shan, C. Kittrell, R.H. Hauge, J.M. Tour, and R.E. Smalley, *Electronic structure control of single-walled carbon nanotube functionalization*. *Science*, 2003. **301**(5639): p. 1519-1522.
175. A.J. Blanch, C.E. Lenehan, and J.S. Quinton, *Dispersant Effects in the Selective Reaction of Aryl Diazonium Salts with Single-Walled Carbon Nanotubes in Aqueous Solution*. *The Journal of Physical Chemistry C*, 2012. **116**(2): p. 1709-1723.
176. A.J. Hilmer, T.P. McNicholas, S. Lin, J. Zhang, Q.H. Wang, J.D. Mendenhall, C. Song, D.A. Heller, P.W. Barone, D. Blankschtein, and M.S. Strano, *Role of Adsorbed Surfactant in the Reaction of Aryl Diazonium Salts with Single-Walled Carbon Nanotubes*. *Langmuir*, 2012. **28**(2): p. 1309-1321.
177. W.L. Jorgensen, M.L.P. Price, and D. Ostrovsky, *Gas-phase and liquid-state properties of esters, nitriles, and nitro compounds with the OPLS-AA force field*. *Journal of Computational Chemistry*, 2001. **22**(13): p. 1340-1352.
178. J.N.C. Lopes, A.A.H. Padua, and K. Shimizu, *Molecular force field for ionic liquids IV: Trialkylimidazolium and alkoxycarbonyl-imidazolium cations; alkylsulfonate and alkylsulfate anions*. *Journal of Physical Chemistry B*, 2008. **112**(16): p. 5039-5046.
179. J.N.C. Lopes and A.A.H. Padua, *Molecular force field for ionic liquids composed of triflate or bistriflylimide anions*. *Journal of Physical Chemistry B*, 2004. **108**(43): p. 16893-16898.
180. M.J. Frisch, G.W. Trucks, H.B. Schlegel, G.E. Scuseria, M.A. Robb, J.R. Cheeseman, J.A. Montgomery, T. Vreven, K.N. Kudin, J.C. Burant, J.M. Millam, S.S. Iyengar, J. Tomasi, V. Barone, B. Mennucci, M. Cossi, G. Scalmani, N. Rega, G.A. Petersson, H. Nakatsuji, M. Hada, M. Ehara, K. Toyota, R. Fukuda, J. Hasegawa, M. Ishida, T. Nakajima, Y. Honda, O. Kitao, H. Nakai, M. Klene, X. Li, J.E. Knox, H.P. Hratchian, J.B. Cross, V. Bakken, C. Adamo, J. Jaramillo, R. Gomperts, R.E. Stratmann, O. Yazyev, A.J. Austin, R. Cammi, C. Pomelli, J.W. Ochterski, P.Y. Ayala, K. Morokuma, G.A. Voth, P. Salvador, J.J. Dannenberg, V.G. Zakrzewski, S. Dapprich, A.D. Daniels, M.C. Strain, O. Farkas, D.K. Malick, A.D. Rabuck, K. Raghavachari, J.B. Foresman, J.V. Ortiz, Q. Cui, A.G. Baboul, S. Clifford, J. Cioslowski, B.B. Stefanov, G. Liu, A. Liashenko, P. Piskorz, I. Komaromi, R.L. Martin, D.J. Fox, T. Keith, A. Laham, C.Y. Peng, A. Nanayakkara, M. Challacombe, P.M.W. Gill, B. Johnson, W. Chen, M.W. Wong, C. Gonzalez, and J.A. Pople, *Gaussian 03, Revision C.02*, 2003: Gaussian 03, Revision C.02.
181. C.M. Breneman and K.B. Wiberg, *Determining Atom-Centered Monopoles from Molecular*



- Electrostatic Potentials - the Need for High Sampling Density in Formamide Conformational-Analysis.* Journal of Computational Chemistry, 1990. **11**(3): p. 361-373.
182. J.N.C. Lopes, J. Deschamps, and A.A.H. Padua, *Modeling ionic liquids using a systematic all-atom force field.* Journal of Physical Chemistry B, 2004. **108**(6): p. 2038-2047.
183. T.H. Dunning, *Gaussian-Basis Sets for Use in Correlated Molecular Calculations .1. The Atoms Boron through Neon and Hydrogen.* Journal of Chemical Physics, 1989. **90**(2): p. 1007-1023.
184. K.L. Schuchardt, B.T. Didier, T. Elsethagen, L.S. Sun, V. Gurumoorthi, J. Chase, J. Li, and T.L. Windus, *Basis set exchange: A community database for computational sciences.* Journal of Chemical Information and Modeling, 2007. **47**(3): p. 1045-1052.
185. D. Feller, *The role of databases in support of computational chemistry calculations.* Journal of Computational Chemistry, 1996. **17**(13): p. 1571-1586.
186. P.W. Barone, H. Yoon, R. Ortiz-Garcia, J.Q. Zhang, J.H. Ahn, J.H. Kim, and M.S. Strano, *Modulation of Single-Walled Carbon Nanotube Photoluminescence by Hydrogel Swelling.* ACS Nano, 2009. **3**(12): p. 3869-3877.
187. M. Suttipong, N.R. Tummala, B. Kitiyanan, and A. Striolo, *Role of Surfactant Molecular Structure on Self-Assembly: Aqueous SDBS on Carbon Nanotubes.* Journal of Physical Chemistry C, 2011. **115**(35): p. 17286-17296.
188. W. Humphrey, A. Dalke, and K. Schulten, *VMD: Visual molecular dynamics.* Journal of Molecular Graphics & Modelling, 1996. **14**(1): p. 33-38.
189. E.R. Margine, M.L. Bocquet, and X. Blase, *Thermal Stability of Graphene and Nanotube Covalent Functionalization.* Nano Letters, 2008. **8**(10): p. 3315-3319.
190. A.J. Siitonen, D.A. Tsyboulski, S.M. Bachilo, and R.B. Weisman, *Dependence of Exciton Mobility on Structure in Single-Walled Carbon Nanotubes.* Journal of Physical Chemistry Letters, 2010. **1**(14): p. 2189-2192.
191. J.M. Englert, C. Dotzer, G.A. Yang, M. Schmid, C. Papp, J.M. Gottfried, H.P. Steinruck, E. Spiecker, F. Hauke, and A. Hirsch, *Covalent bulk functionalization of graphene.* Nature Chemistry, 2011. **3**(4): p. 279-286.
192. D.R. Dreyer, S. Park, C.W. Bielawski, and R.S. Ruoff, *The chemistry of graphene oxide.* Chemical Society Reviews, 2010. **39**(1): p. 228-240.
193. C.-J. Shih, S. Lin, R. Sharma, M.S. Strano, and D. Blankschtein, *Understanding the pH-Dependent Behavior of Graphene Oxide Aqueous Solutions: A Comparative Experimental and Molecular Dynamics Simulation Study.* Langmuir, 2012. **28**(1): p. 235-241.

194. J. Schneider and L. Colombi Ciacchi, *Specific Material Recognition by Small Peptides Mediated by the Interfacial Solvent Structure*. Journal of the American Chemical Society, 2012. **134**(4): p. 2407-2413.
195. A.D. Radadia, C.J. Stavis, R. Carr, H.J. Zeng, W.P. King, J.A. Carlisle, A. Aksimentiev, R.J. Hamers, and R. Bashir, *Control of Nanoscale Environment to Improve Stability of Immobilized Proteins on Diamond Surfaces*. Advanced Functional Materials, 2011. **21**(6): p. 1040-1050.
196. S. Liao, Y. Shnidman, and A. Ulman, *Adsorption Kinetics of Rigid 4-Mercaptobiphenyls on Gold*. Journal of the American Chemical Society, 2000. **122**(15): p. 3688-3694.
197. J. Schneider and L.C. Ciacchi, *A Classical Potential to Model the Adsorption of Biological Molecules on Oxidized Titanium Surfaces*. Journal of Chemical Theory and Computation, 2010. **7**(2): p. 473-484.
198. M. Steenackers, A.M. Gigler, N. Zhang, F. Deubel, M. Seifert, L.H. Hess, C.H.YX. Lim, K.P. Loh, J.A. Garrido, R. Jordan, M. Stutzmann, and I.D. Sharp, *Polymer Brushes on Graphene*. Journal of the American Chemical Society, 2011. **133**(27): p. 10490-10498.
199. M. Riccò, D. Pontiroli, M. Mazzani, M. Choucair, J.A. Stride, and O.V. Yazyev, *Muons Probe Strong Hydrogen Interactions with Defective Graphene*. Nano Letters, 2011. **11**(11): p. 4919-4922.
200. Y.-C. Lin, C.-C. Lu, C.-H. Yeh, C. Jin, K. Suenaga, and P.-W. Chiu, *Graphene Annealing: How Clean Can It Be?* Nano Letters, 2011. **12**(1): p. 414-419.
201. N. Karousis, N. Tagmatarchis, and D. Tasis, *Current Progress on the Chemical Modification of Carbon Nanotubes*. Chemical Reviews, 2010. **110**(9): p. 5366-5397.
202. P. Singh, S. Campidelli, S. Giordani, D. Bonifazi, A. Bianco, and M. Prato, *Organic functionalisation and characterisation of single-walled carbon nanotubes*. Chemical Society Reviews, 2009. **38**(8): p. 2214-2230.
203. A.J. Hilmer, T.P. McNicholas, S.C. Lin, J.Q. Zhang, Q.H. Wang, J.D. Mendenhall, C.S. Song, D.A. Heller, P.W. Barone, D. Blankschtein, and M.S. Strano, *Role of Adsorbed Surfactant in the Reaction of Aryl Diazonium Salts with Single-Walled Carbon Nanotubes*. Langmuir, 2012. **28**(2): p. 1309-1321.
204. S. Lin, A.J. Hilmer, J.D. Mendenhall, M.S. Strano, and D. Blankschtein, *Molecular Perspective on Diazonium Adsorption for Controllable Functionalization of Single-Walled Carbon Nanotubes in Aqueous Surfactant Solutions*. Journal of the American Chemical Society, 2012. **134**(19): p. 8194-8204.
205. A.J. Blanch, C.E. Lenehan, and J.S. Quinton, *Optimizing Surfactant Concentrations for Dispersion*

- of Single-Walled Carbon Nanotubes in Aqueous Solution*. The Journal of Physical Chemistry B, 2010. **114**(30): p. 9805-9811.
206. N.R. Tummala, B.H. Morrow, D.E. Resasco, and A. Striolo, *Stabilization of Aqueous Carbon Nanotube Dispersions Using Surfactants: Insights from Molecular Dynamics Simulations*. ACS Nano, 2010. **4**(12): p. 7193-7204.
207. P. Angelikopoulos and H. Bock, *The Nanoscale Cinderella Problem: Design of Surfactant Coatings for Carbon Nanotubes*. The Journal of Physical Chemistry Letters, 2011. **2**(3): p. 139-144.
208. S.J. Marrink, H.J. Risselada, S. Yefimov, D.P. Tieleman, and A.H. de Vries, *The MARTINI force field: Coarse grained model for biomolecular simulations*. Journal of Physical Chemistry B, 2007. **111**(27): p. 7812-7824.
209. S.A. Egorov, *Microphase separation of mixed polymer brushes physisorbed on cylindrical surfaces*. Soft Matter, 2012. **8**(14): p. 3971-3979.
210. K. Chen and Y.-q. Ma, *Interactions between Colloidal Particles Induced by Polymer Brushes Grafted onto the Substrate*. The Journal of Physical Chemistry B, 2005. **109**(37): p. 17617-17622.
211. N. Patel and S.A. Egorov, *Interactions between nanocolloidal particles in polymer solutions: Effect of attractive interactions*. Journal of Chemical Physics, 2005. **123**(14): p. 144916.
212. R. Shvartzman-Cohen, M. Florent, D. Goldfarb, I. Szleifer, and R. Yerushalmi-Rozen, *Aggregation and Self-Assembly of Amphiphilic Block Copolymers in Aqueous Dispersions of Carbon Nanotubes*. Langmuir, 2008. **24**(9): p. 4625-4632.
213. S.V. Savenko and M. Dijkstra, *Phase behavior of a suspension of colloidal hard rods and nonadsorbing polymer*. Journal of Chemical Physics, 2006. **124**(23).
214. A.C.T. van Duin, S. Dasgupta, F. Lorant, and W.A. Goddard, *ReaxFF: A reactive force field for hydrocarbons*. Journal of Physical Chemistry A, 2001. **105**(41): p. 9396-9409.
215. P.W. Barone, S. Baik, D.A. Heller, and M.S. Strano, *Near-infrared optical sensors based on single-walled carbon nanotubes*. Nature Materials, 2005. **4**(1): p. 86-92.
216. F. Schedin, A.K. Geim, S.V. Morozov, E.W. Hill, P. Blake, M.I. Katsnelson, and K.S. Novoselov, *Detection of individual gas molecules adsorbed on graphene*. Nature Materials, 2007. **6**(9): p. 652-655.
217. X. Wang, L. Zhi, and K. Mullen, *Transparent, Conductive Graphene Electrodes for Dye-Sensitized Solar Cells*. Nano Letters, 2007. **8**(1): p. 323-327.
218. S.W. Lee, N. Yabuuchi, B.M. Gallant, S. Chen, B.-S. Kim, P.T. Hammond, and Y. Shao-Horn,

*High-power lithium batteries from functionalized carbon-nanotube electrodes.* Nature Nanotechnology, 2010. 5(7): p. 531-537.

219. L. Ji, Z. Tan, T. Kuykendall, E.J. An, Y. Fu, V. Battaglia, and Y. Zhang, *Multilayer nanoassembly of Sn-nanopillar arrays sandwiched between graphene layers for high-capacity lithium storage.* Energy & Environmental Science, 2011. 4(9): p. 3611-3616.
220. S. Stankovich, D.A. Dikin, G.H.B. Dommett, K.M. Kohlhaas, E.J. Zimney, E.A. Stach, R.D. Piner, S.T. Nguyen, and R.S. Ruoff, *Graphene-based composite materials.* Nature, 2006. 442(7100): p. 282-286.
221. M.K. Shin, B. Lee, S.H. Kim, J.A. Lee, G.M. Spinks, S. Gambhir, G.G. Wallace, M.E. Kozlov, R.H. Baughman, and S.J. Kim, *Synergistic toughening of composite fibres by self-alignment of reduced graphene oxide and carbon nanotubes.* Nature Communications, 2012. 3: p. 650.
222. RamanathanT, A.A. Abdala, StankovichS, D.A. Dikin, M. Herrera Alonso, R.D. Piner, D.H. Adamson, H.C. Schniepp, ChenX, R.S. Ruoff, S.T. Nguyen, I.A. Aksay, R.K. Prud'Homme, and L.C. Brinson, *Functionalized graphene sheets for polymer nanocomposites.* Nature Nanotechnology, 2008. 3(6): p. 327-331.